

Surface plasmon-enhanced molecular switching for optoelectronic applications

Bohdan Lenyk

Information

Band / Volume 77

ISBN 978-3-95806-595-6

Forschungszentrum Jülich GmbH
Institute of Biological Information Processing
Bioelectronics (IBI-3)

Surface plasmon-enhanced molecular switching for optoelectronic applications

Bohdan Lenyk

Schriften des Forschungszentrums Jülich
Reihe Information / Information

Band / Volume 77

ISSN 1866-1777

ISBN 978-3-95806-595-6

Bibliografische Information der Deutschen Nationalbibliothek.
Die Deutsche Nationalbibliothek verzeichnet diese Publikation in der
Deutschen Nationalbibliografie; detaillierte Bibliografische Daten
sind im Internet über <http://dnb.d-nb.de> abrufbar.

Herausgeber
und Vertrieb: Forschungszentrum Jülich GmbH
 Zentralbibliothek, Verlag
 52425 Jülich
 Tel.: +49 2461 61-5368
 Fax: +49 2461 61-6103
 zb-publikation@fz-juelich.de
 www.fz-juelich.de/zb

Umschlaggestaltung: Grafische Medien, Forschungszentrum Jülich GmbH

Druck: Grafische Medien, Forschungszentrum Jülich GmbH

Copyright: Forschungszentrum Jülich 2021

Schriften des Forschungszentrums Jülich
Reihe Information / Information, Band / Volume 77

D 352 (Diss. Konstanz, Univ. 2021)

ISSN 1866-1777
ISBN 978-3-95806-595-6

Vollständig frei verfügbar über das Publikationsportal des Forschungszentrums Jülich (JuSER)
unter www.fz-juelich.de/zb/openaccess.



This is an Open Access publication distributed under the terms of the [Creative Commons Attribution License 4.0](https://creativecommons.org/licenses/by/4.0/),
which permits unrestricted use, distribution, and reproduction in any medium, provided the original work is properly cited.

ABSTRACT

Molecular electronics aims at gaining control over the operation of macroscopic devices by employing molecules as building blocks. To fulfill the spectrum of functions, various types of molecules are designed including photochromic molecules. Diarylethenes are an example of the latter one and are discussed as potential optoelectronic switches, which can reversibly transition between two forms with different electrical conductance and optical absorbance. By exposure to UV light, the overall electronic structure alters from non-conjugation (open) to end-to-end conjugation (closed) forms, while visible light reverses the process.

These features enable to intensively employ diarylethenes in a single-molecule junction upscaling their usage to large-area ensemble contacts. However, in general, the transition between closed and open states (opening) exhibits a lower quantum yield compared to the reverse UV-activated process of closing. These unequal switching rates can be problematic for optoelectronic molecular contacts relying on reversible switching. Thereby, in this work, the novel strategy is proposed to use surface plasmon-enhanced electromagnetic fields to accelerate the visible-light-mediated cycloreversion reaction. To implement this concept into large-area molecular contacts with vertical geometry, a plasmonic field enhancement of gold films perforated with nanoholes was employed.

The surface plasmon resonance properties of nanohole arrays fabricated by nanosphere lithography are systematically studied as a function of the geometrical features such as lattice constant, thickness, and hole diameter. Moreover, nanohole arrays are tested in different media, e.g. aqueous solution, revealing a novel phenomenon of enhanced transmission in the visible range, which can be applied not only for enhancing visible-light-triggered chemical reactions but for other applications like biosensing, live-cell imaging, etc.

Optical response, mechanical features, and switching kinetics of solid films of diarylethenes are studied in two switching configurations such as back-side and front-side switching, and on different substrates like transparent quartz and nanohole arrays. The latter reveal enhanced optical transmission ($\sim 60\%$) and pronounced enhancement of elec-

tromagnetic field intensities, resulting in around 50% faster opening kinetics of the diarylethenes compared with quartz substrates. All experimental UV-vis measurements are corroborated with finite-difference time-domain simulation verifying the obtained results.

The electrical response of diarylethenes is investigated in vertical geometry junctions realized in crossbar configurations. Two independent scenarios of fabrication are proposed enabling the implementation of nanohole arrays to support the potential of surface plasmon-enhanced visible-light-triggered electrical switching.

ZUSAMMENFASSUNG

Die molekulare Elektronik zielt darauf ab, Steuerbare makroskopische Schaltkreise zu entwickeln, in denen Moleküle als Bausteine verwendet werden. Um vielfältige Funktionen zu realisieren, werden verschiedene Arten von Molekülen entwickelt, einschließlich photochromer Moleküle. Diarylethene sind ein Beispiel für letztere und werden als potentielle optoelektronische Schalter betrachtet, die reversibel inzwischen zwei Formen mit unterschiedlicher elektrischem Leitwert und optischer Absorption hin- und hergeschaltet werden können. Durch die Einwirkung von UV-Licht ändert sich die gesamte elektronische Struktur von einer nichtkonjugierten (offenen) zu einer durchgehend konjugierten Form (geschlossen), während sichtbares Licht den Prozess umkehrt.

Diese Merkmale ermöglichen sowohl den Einsatz von Diarylethenen in Einzelmolekülkontakten als auch ihre Verwendung in großflächigen Ensemblekontakten. Im Allgemeinen zeigt der Übergang zwischen geschlossenen und offenen Zuständen (Öffnen) jedoch eine geringere Quantenausbeute im Vergleich zum umgekehrten UV-aktivierten Schließprozess. Diese ungleichen Schaltraten können problematisch für optoelektronische molekulare Kontakte sein, die auf reversiblen Schalten beruhen. In dieser Arbeit wird daher eine neuartige Strategie zur Nutzung von durch Oberflächenplasmonen verstärkten elektromagnetischen Feldern vorgeschlagen, um die durch sichtbares Licht vermittelte Cycloreversionsreaktion zu beschleunigen. Um dieses Konzept in großflächige molekulare Kontakte mit vertikaler Geometrie umzusetzen, wurde eine plasmonische Feldverstärkung von mit Nanolöchern perforierten Goldfilmen eingesetzt.

Die Oberflächenplasmonenresonanzen in durch Kolloidlithographie hergestellten Nanoloch-Arrays werden systematisch in Abhängigkeit der geometrischen Merkmale wie Gitterkonstante, Dicke und Lochdurchmesser untersucht. Darüber hinaus werden Nanoloch-Arrays in verschiedenen Medien getestet, z. B. in wässriger Lösung, was das neue Phänomen der erhöhten Transmission im sichtbaren Bereich aufzeigt, das nicht nur zur Beschleunigung der durch sichtbares Licht ausgelösten chemischen Reaktionen führt, sondern auch für andere Anwendungen wie Biosensorik, Bildgebung lebender Zellen usw. angewendet werden kann.

Optische Reaktionen, mechanische Merkmale und Schaltkinetik kompakter Diarylethenfilme werden in zwei Schaltkonfigurationen, nämlich Beleuchtung von der Rück- und von der Vorderseite sowie auf transparenten Quarz- und Nanoloch-Arrays auf verschiedenen Substraten untersucht. Letztere zeigen eine verbesserte optische Transmission ($\sim 60\%$) und eine ausgeprägte Verstärkung der elektromagnetischen Feldintensitäten, was zu einer um etwa 50% schnelleren Öffnungskinetik der Diarylethene im Vergleich zu Quarzsubstraten führt. Alle experimentellen UV-Vis-Messungen werden durch Finite-Difference-Time-Domain-Simulationen bestätigt, die die erhaltenen experimentellen Ergebnisse verifiziert.

Die elektrischen Reaktionen von Diarylethenen werden in Kontakten mit vertikaler Geometrie untersucht, die in Crossbar-Konfiguration realisiert werden. Es werden zwei unabhängige Herstellungsszenarien vorgeschlagen, die die Implementierung von Nanoloch-Arrays ermöglichen, um das Potenzial von durch Oberflächenplasmonen verstärkte, durch sichtbares Licht ausgelöstes elektrisches Schalten zu nutzen.

CONTENTS

Abstract	i
Zusammenfassung	iii
1 Introduction	1
2 Fundamentals	3
2.1 Molecular junctions	3
2.1.1 Transport mechanisms in molecules	3
2.1.2 Large-area ensemble molecular contacts	6
2.1.3 Diarylethene-based molecular junctions	8
2.2 Surface plasmon polaritons	10
2.2.1 Optical properties of noble metals	10
2.2.2 Surface plasmons at metal-dielectric interfaces	12
2.2.3 Excitation of surface plasmon polaritons	15
2.2.4 Nanohole arrays	16
2.3 State of the art	19
2.3.1 Molecular optoelectronic switches	19
2.3.2 Photochromic molecule-based plasmonic structures	20
3 Materials & Methods	21
3.1 Fabrication and characterization methods	21
3.1.1 Lithography	21
3.1.2 Chemical etching & deposition	24
3.1.3 Surface analysis	27
3.1.4 Preparation of the C ₅ FHSAc films	29
3.2 Optical measurements	30
3.3 Electrical measurements	32

3.4	Simulations	33
3.4.1	FDTD simulations	33
3.4.2	Finite element method (FEM)	36
4	Sample fabrication & characterization	39
4.1	Fabrication of nanohole arrays	39
4.1.1	Nanosphere lithography (NSL)	39
4.1.2	Reduction of particles	42
4.1.3	Characterization of particle monolayers	45
4.2	Bottom electrode fabrication	48
4.2.1	Bottom electrode fabrication by NSL	48
4.2.2	Electrical conductivity of nanohole arrays bottom electrode	52
4.2.3	Bottom electrode fabrication by e-beam lithography	53
4.3	Top electrode fabrication	55
4.3.1	Top electrode fabrication by transfer onto a POP stamp	55
4.3.2	Top electrode by direct fabrication onto POP	57
4.4	Crossbars assembly	60
5	Results & Discussion	63
5.1	Characteristic of diarylethenes in the solid and liquid state	63
5.1.1	Chemical & optical properties	63
5.1.2	Refractive index estimation	67
5.1.3	Switching kinetics	69
5.2	Optical properties of nanohole arrays	72
5.2.1	Tuning the Surface Plasmon resonances	72
5.2.2	Enhanced transmission by waveguide modes	77
5.3	Surface plasmon-enhanced switching kinetics	80
5.3.1	Morphology of the C ₅ FHSAc film on nanohole arrays	80
5.3.2	Optical response of the C ₅ FHSAc film on nanohole arrays	82
5.3.3	Switching kinetics of the C ₅ FHSAc film on nanohole arrays	84
5.4	Electrical measurements of diarylethenes	97
5.4.1	Switching ability of C ₅ FHSAc molecules	97
5.4.2	Live switching of C ₅ FHSAc molecules	98
6	Summary & outlook	101
	Acknowledgements	103
	A Appendix	105

A.1 Protocols 105
A.2 Photo- and e-beam fabrication masks 113
A.3 Optical properties of nanohole arrays 117
A.4 FDTD and experimental spectrum 118

List of Abbreviations

AFM	atomic force microscopy
ALD	atomic layer deposition
Au	gold film
BSEs	backscattered electrons
C ₅ FHSAc	C ₅₁ H ₃₀ F ₆ O ₄ S ₂
DI	deionized
EOT	extraordinary transmission
FAIA	funnel assisted interfacial assembly
FDTD	finite-difference time-domain
FEM	finite element method
FWHM	full width at half maximum
hAu	gold nanohole arrays nicknamed as "holey" gold
ICP	inductively coupled plasma
IR	infrared
LOFO	lift-off float-on
MEA	microelectrode arrays
NSL	nanosphere lithography
PALO	polymer-assisted lift-off
POP	polyolefin plastomer
PS	polystyrene
PTFE	polytetrafluorethylen
rGO	reduced graphene oxide
RF	radio frequency
RI	refractive index
RIE	reactive ion etching
SAMs	self-assembled monolayers

SEM	scanning electron microscopy
SEs	secondary electrons
SiO _x	silicon oxide
SPP	surface plasmon polariton
SPPs	surface plasmon polaritons
SWNTs	single-walled carbon nanotubes
TE	transverse electric
TM	transverse magnetic
TX-100	triton-x 100

CHAPTER 1

INTRODUCTION

The particular interest of molecular electronics is to design macroscopic devices with molecules playing the role of functional units [1]. One subtype of molecular devices utilizes photochromic molecules to fulfill the requirements of applications where the precise control of operations is performed by external light exposure [2, 3]. The associated alternations of the electronic structure of the molecules facilitate the design and fabrication of optical and optoelectronic devices [4].

Diarylethenes are discussed as an example of photochromic molecules, which can reversibly transition between two forms with different absorbance and approximately one order magnitude difference in conductance [5]. The reversible transfer between these forms can be achieved by applying either UV or visible light. UV light transforms the non-conjugated (open) form into the completely conjugated (closed), while visible light reverses the process which proceeds without major alteration in molecular geometry [6]. Furthermore, attributed stability and thermal irreversibility make diarylethenes a suitable candidate for implementation into functional optoelectronic switches [7, 8].

However, the two independent subreactions activated by UV and visible light possess unequal quantum yields which may differ by several orders of magnitude [6, 9, 10]. Generally, the visible-light-triggered reaction features much slower switching rates compared to the reverse UV-activated process. This brings issues to transport experiments resulting in hindered visible-light-assisted reactions [11, 12]. To overcome these restrictions, multiple strategies are proposed suggesting mostly technological changes e.g. junction geometry, high power external sources, etc. Alternatively, in this work, the enhancement of electromagnetic fields associated with surface plasmon excitation is proposed to accelerate the visible-light-mediated process.

1. Introduction

The surface plasmons are employed in a broad spectrum of applications enabling the utilization of enhanced optical fields in the close vicinity of the surface, for instance, to increase the intensity of Raman modes in Surface Enhanced Raman Spectroscopy [13, 14]. Furthermore, the strong confinement of the electromagnetic fields to interfaces facilitates the probing of the surface process with high sensitivity, which is widely realized in fields like biosensing [15, 16], photovoltaics [17–19], and others.

Molecular junctions are designed to capture molecules between two conductive electrodes proposing various schemes and geometries from single-molecule devices to large-area junctions. However, the latter ones remain still challenging lacking the standards to insert millions of molecules between two solid electrodes. Among others, the vertical geometries like metal-molecule-top electrodes show promising results, in particular, for achieving bidirectional switching of photochromic molecules [20]. Different materials of top electrodes like reduced Graphene Oxide (rGO) [21], liquid metals (e.g. InGa) [22], and metal transfer techniques such as lift-off float-on (LOFO) [23] have been employed to complete the top contact between molecules and electrodes. In this work, the modification of the latter technique was chosen. However, the incorporation of surface plasmons into molecular junctions brings additional physical and mechanical issues requiring not only conductive and transparent electrodes for UV and visible light but also suitable platforms to support surface plasmon-light coupling. Conventional materials like indium tin oxide or graphene serve as electrode material fulfilling the demands of transparency, however, none of them matches the requirements of surface plasmon excitations. Thereby, in this work, to achieve the aforementioned standards, periodic gratings within gold metal films (nanohole arrays) [24] were chosen to provide coupling of the switching light to the surface plasmons. Nanohole arrays are proposed to serve as a bottom electrode in the metal-molecule-metal vertical geometry contacts.

Unlike other techniques such as e.g. the Kretschmann configuration [25], nanohole arrays can provide coupling between the wavevector of the incident light and surface plasmons without additional assisted components like e.g. prisms. The resulting enhanced fields at the metal-molecule interface can potentially accelerate the switching kinetics of the molecules.

CHAPTER 2

FUNDAMENTALS

2.1 MOLECULAR JUNCTIONS

The field of molecular electronics is commonly introduced as a branch of nanotechnology with molecules employed as building blocks to gain control over the function of macroscopic devices on the nanoscale level [1, 26]. Conceptually, the topic of molecular electronics starts with a single-molecule based device [27–30] considered as a zero-dimensional object (0D) with dimensions smaller than the electron wavelength, upscaling to large-area junctions introduced as a monolayer with two dimensions (2D) [31]. The latter one attracts a large interest due to the high potential incorporation of molecular components into electronic circuit units. However, it still remains challenging, in particular, due to the physical and mechanical issues to sandwich molecules between two solid electrodes [32, 33].

2.1.1 TRANSPORT MECHANISMS IN MOLECULES

A molecule junction, generally, can be divided into three intercorrelated components: the electrode, the contact interface, and the molecular backbone or functional center. There are several conduction mechanisms for molecules known as resonant and non-resonant coherent tunneling, thermally induced hopping, Fowler–Nordheim tunneling, Poole–Frenkel transport, field emission, etc. [34–37]. It has been shown that among other factors that impact the charge transport across molecules, the molecular length highly dominates and defines the main conduction mechanism [38–40]. With the increase of the length of the junction, for instance, by adding multilayers, the dominant electron transport properties alter from tunneling attributed to single-molecule junctions (<6 nm) to hopping which is

2. Fundamentals

the main mode of transport in organic films with a thickness (>50 nm), (Figure 2.1) [36].

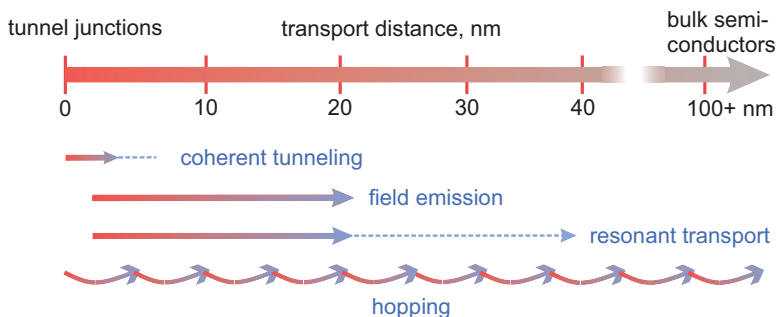


FIGURE 2.1: Schematic drawing representing characteristic length ranges for transport mechanisms that can occur in molecular junctions (from a few nm tunnel junctions to bulk films with a thickness of >50 nm). Dashed lines stand for the range within which the phenomenon occurs under certain conditions and materials involved [36].

Tunneling

The current flow through a molecular junction consisting of two electrodes separated by molecules with a length shorter than ~ 5 -6 nm is realized dominantly through the tunneling process [41] characterized by the Landauer approach [42]. If the configuration metal-molecule-metal is considered, the two metal electrodes are modeled as solid state body with a continuous band structure filled up to the Fermi energy level E_F whereas a molecule is described with the Highest Occupied Molecular Orbital (HOMO) and the Lowest Unoccupied Molecular Orbital (LUMO), (Figure 2.2). Applying the voltage to the

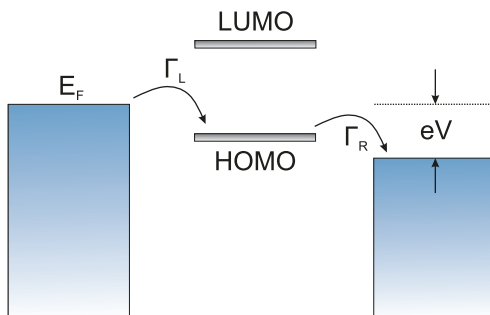


FIGURE 2.2: Schematic drawing of the resonant tunneling showing HOMO and LUMO molecular energy levels located between two metal electrodes characterized by Fermi level E_F . The coupling (Γ) of the electrodes to the molecular orbitals leads to electric transport through the molecular levels.

junction leads to the reduction of the energy level of one electrode by eV . This difference in the potentials of the left and right tends to create energetically favorable conditions to resonant tunneling behavior through the molecular orbital if the HOMO/LUMO levels lie in between the Fermi levels of the electrodes. In this case, electrons are transferred across the molecular junction to maintain equilibrium involving an occupation or clearing of respective orbitals.

There are two types of transport that possibly can occur across molecular junctions typically referred to dispersive or ballistic. Unlike the dispersive mechanism, where energy is transferred with the drift of electrons due to the collisions with each other, ballistic transport is the unimpeded flow of electrons characterized by collision-free motion. In the absence of inelastic interactions, the current in single-molecule junctions is given by the expression [43]:

$$I = \frac{2e}{h} \int_{-\infty}^{\infty} T(E) [f_L(E) - f_R(E)] dE \quad (2.1)$$

where $T(E)$ being the electron transmission probability as a function of energy and $f(E)$ is the Fermi distribution function (the subscripts L and R denote the left and right electrode). The transmission function $T(E)$ depends on the coupling strength of both leads (Γ_L and Γ_R) to the molecular orbital and their respective energy level positions. When it is assumed that a single molecular orbital located at an energy E_0 from the Fermi energy E_F , the transmission function can be expressed with the resonance Lorentzian shape as follows:

$$T(E) = \frac{4\Gamma_L\Gamma_R}{(E - E_0)^2 + (\Gamma_L + \Gamma_R)^2} \quad (2.2)$$

Thereby, the conductance of single-molecule junctions increases with the interface coupling strength and decreases with the energy offset between the dominant conducting molecular orbitals and the electrode's Fermi level.

Hopping

Further increase of the length of a molecular junction tends to create conditions for multiple mechanisms such as field emission, resonant tunneling, hopping, and others. The field emission is referred to a special case of coherent tunneling when the effective applied bias exceeds the energy of the tunnel barrier. It is independent of temperature but decreases exponentially with the distance.

Unlike tunneling mechanisms, where current flow involves an electron transport through a barrier, the hopping includes electron motion over the barrier containing a series of transfers between neighboring relatively stable sites consisting of localized redox states. Noteworthy, as an alternative to a hopping process resonant tunneling has been proposed

2. Fundamentals

introducing charge carriers transporting through molecular orbitals rather than tunneling through barriers. The distinction between two aforementioned mechanisms is associated with the activation which is required to support only hopping transport. The activation barrier can result in slow charge transport causing low mobilities which is typical for organic semiconductors.

In Marcus theory, which explains the rates of electron transfer [44], the conductance G attributed to hopping charge transport exhibits a temperature dependence resulting in the following relation:

$$G \propto e^{\frac{-E_a}{k_B T}} \quad (2.3)$$

where E_a being the activation energy, while T and k_B denote the temperature and Boltzmann's constant, respectively. Moreover, it is characterized as a weak length-dependent process making it inversely proportional to the molecular length. Among others, the temperature dependence is a key factor, which enables to distinguish and separate hopping and tunneling charge transport mechanisms.

2.1.2 LARGE-AREA ENSEMBLE MOLECULAR CONTACTS

The large-area ensemble molecular contacts are discussed as a linking bridge for transferring benefits of single-molecule junctions to the scale of typical electronic micro- and nano-circuits. However, it brings the biggest challenge of inserting the functional layer of millions of molecules between two solid electrodes. In order to obtain a reliable large-area junction, possible damage of sensitive and fragile molecules should be prevented. Additionally, an assembling technology is supposed to be designed to optimize the molecule-electrode contacts with the purpose of high yield mass production characterized by robustness and reproducibility. Thereby, it results in numerous demands on all components of the molecular contact to overcome.

The choice of suitable electrode materials depends on several factors such as chemical inertness to air, good processability, work function, and good compatibility with molecules of interest. Furthermore, an assembled contact requires to consider aspects [33] such as coupling of the molecules to the electrode surface, control of the geometry of molecules to avoid different orientations and aggregation effects in molecular assemblies, and deposition of the top contact electrode [45] if a vertical geometry is applied. Thereby, taking into account the aforementioned criteria, there are different fabrication strategies to accomplish reliable molecular contacts.

Firstly, in order to deposit molecular species onto bottom electrodes, the following most commonly used techniques are applied, such as the Langmuir–Blodgett [46], the electrografting [47] methods, and self-assembly [48]. Among others, the latter one has been

widely used due to the resulting high-quality monolayers, its simplicity and versatility. The self-assembly technique relies on the chemisorption of molecules onto electrode surfaces with subsequent attachment via specific binding group followed by self-organization due to the intermolecular forces between neighboring molecules.

Once the molecular layer is assembled, the question emerges how to complete the junction by placing the top electrode without damaging the molecules and changing their electrical properties. To solve this issue, numerous techniques have been employed including physical or chemical vapor deposition, the lift-off float-on (LOFO) process, liquid metal droplets, use of a conducting buffer layer (e.g. organic semiconductor PEDOT:PSS [20, 49], reduced Graphene Oxide (rGO) [21]) and others (Figure 2.3). The most straight-

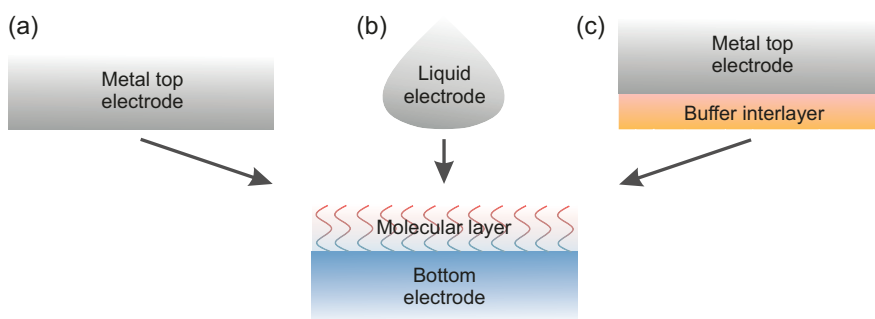


FIGURE 2.3: Sketch represents the main schemes employed to realize large-area molecular junctions in vertical geometry. (a) The sandwich structure consisting of the bottom electrode, assembled molecular layer and a top electrode placed onto molecules by metal evaporation, lift-off float-on (LOFO) process, etc., (b) Liquid metal (Hg, InGa, etc.) employed as top electrode, (c) Sandwich geometry with a buffer conducting layer (e.g. PEDOT:PSS, reduced Graphene Oxide (rGO), etc) placed between the molecular layer and top electrode to prevent damage of molecules.

forward scheme includes the "sandwich" structure with a metal top electrode (Figure 2.3 a) directly deposited by e.g. evaporation onto the molecular layer employing physical or chemical vapor deposition [50–52]. The biggest advantage of this method is its simplicity, however, the direct evaporation approach was extensively criticized. Firstly, the molecular layer is likely to be damaged due to high energetic metal atoms impinging on the surface. Additionally, the diffusion of metal atoms through the layer is likely to lead to a filament formation. This may further be mistakenly attributed to molecular response during electrical measurements due to the resistive contact.

In contrast, different "soft" non-destructive methods have been developed such as lift-off float-on (LOFO) [23] and polymer-assisted lift-off (PALO) [53] approaches. In these methods, a thin metallic film is deposited on a sacrificial substrate via capillary interactions and subsequently transferred onto the assembled molecular layer enabling "soft"

2. Fundamentals

contact and preventing physical damage of the molecules. The transfer is usually performed employing a liquid-mediated process (float-on) on a high-surface tension liquid (e.g. water). Among others, one of the biggest advantages of the LOFO and PALO methods is the potential usage of the smoother peeled side of the metallic film as its active surface, which is beneficial to accomplish reliable molecular contacts.

As an alternative to the aforementioned methods, a conductive metallic liquid can be utilized to complete the contact such as Hg and InGa (Figure 2.3 b) [22]. The damage-free contact is provided here by fluidity and high surface tension of the electrode. However, the possible amalgamation of the liquid metal may happen leading to an asymmetry in current-voltage characteristics. Furthermore, the fluidity brings another drawback that the contact area cannot be precisely defined and varies with the temperature.

Another approach to overcome the aforementioned issues related to physical damage of molecules and reliability of junctions include the usage of buffer interlayers prior to metal evaporation such as conductive polymers like e.g. PEDOT:PSS [49, 54] and carbon-based contacts like e.g. reduced Graphene Oxide (rGO), graphene [55], or single-walled carbon nanotubes (SWNTs) [21, 56, 57]. Such interlayers prevent metal atoms damaging the molecular species by creating a "soft" protective contact. However, in case of PEDOT:PSS, the junction may exhibit an asymmetrical semiconducting electrical characteristics, which hides pure molecular response. Thereby, to prevent it, graphene-based interlayer films have been proposed enabling high yield molecular junctions with good operational stability and reliability. Noteworthy, conductive polymer and graphene buffer layers are often used for solar-cell applications and optical spectroscopy due to their transparency to visible light.

2.1.3 DIARYLETHENE-BASED MOLECULAR JUNCTIONS

Photochromic molecules such as spiropyran [58], azobenzenes [59], fulgides [60, 61], or diarylethenes [62] have been extensively employed in molecular electronics to serve as inks and dyes as well as multifunctional devices [63] and optoelectronic components [64]. The ability to manipulate and alter the function of active devices to match the desired tasks via external light exposure has attracted wide scientific interest [65].

Diarylethene-based molecular electronics devices have been studied intensively over the last two decades [2], in particular in the scale of the single-molecule junctions. However, the first report introduced the exceptional case of irreversible light-induced conductance switching from the conjugated form (closed state) to the non-conjugated (open state) [12]. Later this observation was argued intensively focusing on the closing reaction, which might have been suppressed by the quenching of the excited state of the open form that the molecule has to adopt to be able to transit to the closed form. Since then various new

approaches have been developed [66, 67] leading to the conclusion that molecular engineering (e.g. choice of switching core, side arms anchoring groups [21, 68–70] and junction engineering (geometry, electrode material, and others [71]) are crucial to enable photoinduced switching. This resulted in successful reversible switching of diarylethenes, which opened the field for further investigations and approaches to realize robust molecular switches [72].

However, despite the aforementioned factors, there have been still reports, where irreversible switching is observed. In this case, preferentially the closing reaction takes place, while the opening is disabled [11, 69, 73].

To enhance the reversible switching, extend the functions, and facilitate implementation of photochromic molecules into large-area junctions and organic transistors, conductive polymer matrices were developed [74]. Even though the structural and electronic interactions between molecules and semiconducting polymers are far from being fully understood, there have been various reports on the realization of robust organic optical switches. In particular, the incorporation of diarylethenes in matrices such as poly(3-hexylthiophene) (P3HT), poly(9,9-dioctylfluorene-alt-benzothiadiazole) (F8BT), diketopyrrolopyrrole thieno [3,2-b]thiophene copolymer (DPPT-TT), and poly(4-decyltetradecylisoindigo-alt-dithiophene) (IIDDTC3) resulted in optically switchable transistors with high carrier mobility and "on/off" aspect ratio of $> 10^3$ [75].

2.2 SURFACE PLASMON POLARITONS

When light reaches a metal-dielectric interface, surface waves can be generated due to the specific interaction between incident photons and surface mobile electrons. The free electrons, which exist inside the metal respond to such external stimulation by performing a resonant oscillation, which consequently generates a type of surface waves at the metal-dielectric interface. Noteworthy, these kinds of charge density oscillations in the metal are named surface plasmons whereas the combined modes between the electromagnetic field and the surface plasmons are denoted as surface plasmon polaritons (SPP) [76].

2.2.1 OPTICAL PROPERTIES OF NOBLE METALS

Over a wide frequency range, the optical properties of metals can be quantitatively described by a plasma model, where metal is considered as a gas of free conduction electrons, which moves against a fixed background of positive heavy immobile ions. The mass of ions is about three orders larger than that of electrons, therefore, their movement can be neglected. Furthermore, in the plasma model, the information on lattice potential and electron-electron interactions is not considered. Instead, some aspects of the band structure are incorporated into the effective optical mass m_e of each electron. The electrons oscillate in the response to the applied electromagnetic field, and their motion is damped via collisions occurring with a characteristic collision frequency.

If the harmonic external field $\vec{E}(t) = \vec{E}_0 e^{i\omega t}$ with the amplitude E_0 and frequency ω is applied to a metal that is considered as aforementioned electron gas, the equation of motion of the electron is described by the following equation:

$$m_e \frac{\partial^2 \vec{r}}{\partial t^2} + m_e \gamma \frac{\partial \vec{r}}{\partial t} = e \vec{E}_0 e^{i\omega t} \quad (2.4)$$

where e and m_e denote the charge and the effective mass of the electron, respectively, and \vec{r} is the displacement. The damping parameter γ is oppositely proportional to the relaxation time (τ) and is expressed as $\gamma = v_F/l$ where v_F is the Fermi velocity and l corresponds to the electrons mean free path between scattering events. Typically, relaxation time of the free electron gas is in the order of 10^{-14} s at room temperature, which corresponds to $\gamma = 100$ THz.

The electric field leads to a displacement of electrons with respect to the ions which generates the polarisation $\vec{P} = -Ne\vec{r}$ where N is the number of electrons per volume unit. The optical properties of metals can be described by a complex dielectric constant

ϵ_r that depends on the frequency of the light. It can be expressed as a relation between the dielectric displacement \vec{D} and the electric field \vec{E} as follows:

$$\vec{D} = \epsilon_0 \vec{E} + \vec{P} = \epsilon_0 \epsilon_r \vec{E} \quad (2.5)$$

where ϵ_0 denotes the permittivity of the vacuum ($\epsilon_0 = 8.85 \times 10^{-12} \text{F/m}$) and ϵ_r stands for the relative permittivity of the metal.

Considering the harmonic electron displacement $\vec{r} = \vec{r}_0 e^{i\omega t}$, equation 2.4 yields in the solution for \vec{r} :

$$\vec{r} = \frac{e\vec{E}}{m_e(\omega^2 + i\gamma\omega)} \quad (2.6)$$

Thus, taking into account the aforementioned definition of polarisation \vec{P} and the solution of equation 2.6, the displacement field \vec{D} can be expressed as:

$$\vec{D} = \epsilon_0 \left(1 - \frac{\omega_p^2}{\omega^2 + i\gamma\omega} \right) \vec{E} \quad (2.7)$$

where ω_p is named as plasmon frequency of the free electron gas and is determined as $\omega_p^2 = Ne^2/\epsilon_0 m_e$. Thereby, comparing the equations 2.5 and 2.7, the dielectric constant ϵ_r is derived as:

$$\epsilon_r(\omega) = 1 - \frac{\omega_p^2}{\omega^2 + i\gamma\omega} = 1 - \frac{\omega_p^2 \tau^2}{\omega^2 \tau^2 + i\omega\tau} \quad (2.8)$$

As can be seen, the dielectric constant ϵ_r possesses a complex nature containing a real and an imaginary part, where the latter ϵ_r represents the ohmic losses. By inserting the values of $\omega_p = 13.8 \times 10^{15} \text{ s}^{-1}$ and $\gamma = 1.075 \times 10^{14} \text{ s}^{-1}$ for gold [77], the real part of the dielectric function becomes negative towards the visible range. Furthermore, the dielectric constant enables to quantitatively estimate how the metal behaves at different frequency regimes limited to the condition $\omega < \omega_p$ where metal maintains its metallic nature. In the regime of large frequencies close to ω_p , the approximation $\omega\tau \gg 1$ is applied. In this case the damping can be neglected and the dielectric constant becomes predominantly real as follows:

$$\epsilon_r = 1 - \frac{\omega_p^2}{\omega^2} \quad (2.9)$$

Furthermore, the regime of very low frequencies where $\omega\tau \ll 1$ tends to reveal the domination of the imaginary over the real part of the refractive index. Thus, in this frequency regime, metals mainly absorb.

Noteworthy, if thus-far omitted transparency regime ($\omega > \omega_p$) of the free-electron gas model is considered, by inserting the dielectric constant from equation 2.9 in the

2. Fundamentals

general dispersion relation $k = \epsilon(\vec{k}, \omega) \frac{\omega^2}{c^2}$, the dispersion relation of traveling waves can be obtained (equation 2.10) and plotted correspondingly (Figure 2.5, green solid line).

$$\omega(k) = \sqrt{\omega_p^2 + \frac{k^2 c^2}{\epsilon}} \quad (2.10)$$

As can be seen, for $\omega > \omega_p$ the plasma supports transverse waves propagating with a group velocity $v_g = \frac{d\omega}{dk}$.

2.2.2 SURFACE PLASMONS AT METAL-DIELECTRIC INTERFACES

Surface plasmon polaritons (SPP) are the electromagnetic excitations that propagate along the interface between a metal and a dielectric medium (Figure 2.4) with the evanescent electric field decaying exponentially perpendicular to the interface (along the z axis).

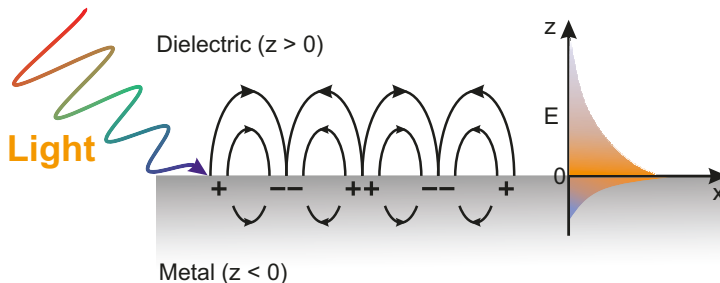


FIGURE 2.4: Schematic drawing of a surface plasmon wave propagation along a metal-dielectric interface with associated electromagnetic field distribution. The field strength decreases exponentially with the vertical distance z from the surface.

To obtain the excitation conditions for SPP, the Maxwell's equations [78] can be solved independently for the metal and dielectric parts with a plane interface between the two media.

A propagating electromagnetic wave through this interface can be described by a wave equation 2.11 (where ∇^2 denotes the Laplacian, c is the speed of light in vacuum) in absence of external charge and current densities.

$$\nabla^2 \vec{E} - \frac{\epsilon}{c^2} \frac{\partial \vec{E}}{\partial t} = 0 \quad (2.11)$$

By assuming in all generality the harmonic time dependence $\vec{E}(\vec{r}, t) = \vec{E}(\vec{r})e^{-i\omega t}$, the wave equation 2.11 converts to the Helmholtz equation:

$$\nabla^2 \vec{E} - k_0^2 \epsilon \vec{E} = 0 \quad (2.12)$$

where k_0 is the wavevector of the propagating wave in vacuum.

Firstly, it is assumed that a metal surface extends infinitely in the x - y plane at $z = 0$, (Figure 2.4). Additionally, the wave propagates in x direction along the $z = 0$ plane and exponentially drops along the z directions into both media.

The solution of the wave equation can be obtained for a set of coupled equations linked to the transverse magnetic (TM or p) modes where only the field components E_x , E_z and H_y are nonzero, and the transverse electric (TE or s) modes that exhibit only nonzero components of H_x , H_z , and E_y .

Furthermore, a dielectric medium is assumed as non-absorbing half-space ($z > 0$) with the positive real dielectric constant ϵ_2 and a conducting half-space ($z < 0$) represented as metal with a dielectric function $\epsilon_1(\omega)$. The metallic nature of the latter implies that the real part of ϵ_1 is negative, which according to equation 2.9 is satisfied at frequencies below the plasmon frequency ω_p . It can be shown [79] that using the conditions for the continuity of the normal and transversal field components on this interface together with the aforementioned restrictions, the surface plasmon polaritons only exist for TM polarization. Thereby, the set of solutions for both half-spaces for TM modes, which propagate along x direction is delivered as follows:

$$\begin{cases} \vec{E}_i = (E_{i,x}, 0, E_{i,y})e^{i(\vec{k}_i \cdot \vec{r} - i\omega t)} & (2.13a) \\ \vec{H}_i = (0, H_{i,y}, 0)e^{i(\vec{k}_i \cdot \vec{r} - i\omega t)} & (2.13b) \\ \vec{D}_i = \epsilon_0 \epsilon_i \vec{E}_i, \quad \vec{B}_i = \mu_0 \vec{H}_i & (2.13c) \end{cases}$$

where $i = 1, 2$ indicates a dielectric and a metallic medium, respectively. The wave vector in equations 2.13 is introduced as $\vec{k}_i = (\beta, 0, k_{i,z})$, where $\beta = k_x$ stands for the propagation constant along the x axis.

Continuity of H_y and $\epsilon_i E_z$ at the interface results in the following relation between components of $k_{i,z}$

$$\frac{k_{2,z}}{k_{1,z}} = -\frac{\epsilon_2}{\epsilon_1} \quad (2.14)$$

The fields decay exponentially into the respective half-spaces with certain confinement to the surface. This demands two materials with opposite signs of the real part of their dielectric permittivities such as conductor and insulator. Thereby, the surface plasmon waves can propagate along the interface between the two media with dielectric permittivities of $\epsilon_2 < 0$ e.g. metal and $\epsilon_1 > 0$ e.g. a dielectric.

As a result, a specific coupled superposition of an electromagnetic wave in the dielectric medium ("polariton") and an oscillating electron plasma in the metal ("surface plasmon") is obtained (Figure 2.4) and due to this composed nature referred to surface plasmon

2. Fundamentals

polariton. These two modes exhibit an evanescent or near field in the close vicinity to the interface and is a consequence of the bound, non-radiative nature of surface plasmons [80].

The penetration depth of the field into the dielectric medium is typically $\sim \lambda/2n$, where n is the refractive index, while in the metal it is shorter and mainly defined by the skin depth (~ 20 nm for most metals in the visible range). The electric field drops along the z axis following the exponential decay $\vec{E} \propto e^{-k_z z}$ which is defined by the constant decay length of $1/k_z$.

Furthermore, one can obtain the dispersion relation for SPP waves utilizing the equations 2.13a and 2.14, which leads to the following relation:

$$\beta = \frac{\omega}{c} \sqrt{\frac{\epsilon_1 \epsilon_2}{\epsilon_1 + \epsilon_2}} \quad (2.15)$$

By inserting values of the simplified dielectric function of metal ϵ_2 (2.9) and a constant value of the dielectric ϵ_2 into the equation 2.15, the dispersion relation function $\omega(\beta)$ can be plotted accordingly (Figure 2.5, violet solid line). As can be seen from Figure 2.5, the

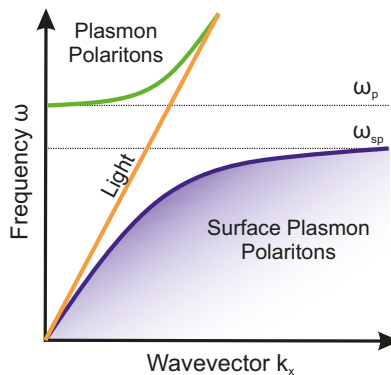


FIGURE 2.5: Dispersion relation of SPPs (violet solid line) in comparison with light in vacuum (orange solid line) and plasmon polaritons (green solid line). At short wavelengths the SPP approaches asymptotically the surface plasmon frequency ω_{sp} .

dispersion line of light in vacuum $\omega_{Light}(k) = ck_x$ (Figure 2.5, yellow solid line) does not intersect with the SPP dispersion curve lying above it and clearly showing a mismatch of momentum. This leads to the fact that to obtain the excitation of SPPs via light irradiation, this momentum difference must be bridged by coupling techniques (prisms, couplers, waveguides). The SPP curve gradually increases with the increase of frequency asymptotically approaching the saturation named as surface plasmon frequency ω_{sp} , which depends on the permittivity of the dielectric medium and is defined as $\omega_{sp} = \frac{\omega_p}{\sqrt{1+\epsilon_2}}$.

2.2.3 EXCITATION OF SURFACE PLASMON POLARITONS

As mentioned above, the SPPs on a planar metal/dielectric interface cannot be excited directly by free-space light irradiation, since at the same frequency there is a momentum mismatch ($\beta > k_{Light}$), which does not allow the coupling of light to surface plasmons (Figure 2.6 a).

As can be seen from the dispersion curve of SPPs (Figure 2.6 a), even for small energies (small wave vector) the free-space light line only asymptotically approaches the SPP curve without intersecting it. Therefore, the excitation of the SPP can be carried out only if the

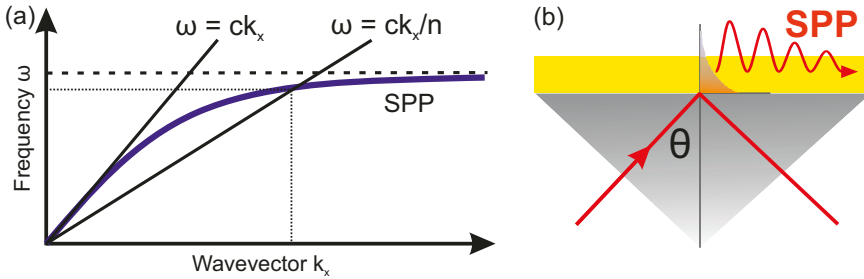


FIGURE 2.6: Excitation of SPPs. (a) The dispersion relation of SPP with the free-space light line and the tilted light line in a dielectric with refractive index n . (b) The drawing represents the prism-assisted Kretschmann configuration setup to excite SPPs in the planar interface.

wavevector of light is increased over its free-space value. Among various approaches to overcome this issue, conceptually the most straightforward approach is utilizing a medium with a certain refractive index $n = \sqrt{\epsilon}$. In this case, the light line is tilted by a factor of n leading to a dispersion relation $\omega = ck_x/\sqrt{\epsilon}$, which results in the intersection with the SPP curve at a certain resonance frequency.

The aforementioned concept is realized in the prism-assisted Kretschmann configuration [25] (Figure 2.6 b). This coupling scheme employs an evanescent electromagnetic field formed at a surface due to the total internal reflection, while the tunneling of the fields of the excitation beam to the metal/air interface provides a phase-matching. Unlike in the Otto configuration [79], the metal film is directly deposited onto the prism with a refractive index n . The excitation beam reaches the film through the prism at an incident angle θ , which is greater than the critical angle of total reflection. The light further reflects from the metal-prism interface while an electromagnetic field resonantly tunnels through the metal film and excites SPPs with an in-plane momentum of $\beta = k\sqrt{\epsilon} \sin(\theta)$.

Alternatively, there are other ways to tilt a free-space light line providing a surface plasmon excitation condition such as e.g. metal nanomaterials [81], dielectric waveguides [82, 83], and periodic gratings. In the latter case, the desired increase of light momentum

is obtained by adding a reciprocal lattice vector \vec{G} of the grating to the free-space wave vector k_x resulting in the new parallel wave vector of $k_x' = k_x + G_x$.

2.2.4 NANO HOLE ARRAYS

Among multiple periodic grating excitation approaches, a metal film perforated with arrays of subwavelength size holes (nanohole arrays [24, 84]) has attracted attention due to its technical feasibility, versatile way of fabrication, and high applicability. In particular, since the first report more than two decades ago [85], nanohole arrays have been intensively used in point-of-care biosensing, photonics, photovoltaics, optical imaging etc.

In the frame of classical theory introduced by Bethe [86], the transmission (T) through subwavelength hole drops dramatically as the fourth power of the ratio between the aperture size (r) and the wavelength (λ): $T \propto (r/\lambda)^4$. However, in the case of arrays of subwavelength holes, the electromagnetic-field confinement in the vicinity of the metallic surface due to the SPP excitation resonantly enhances the light transmitted through the metal film perforated with periodically arranged holes. Consequently, the transmission reveals to be several orders of magnitude larger than predicted by Bethe's aperture theory which is denoted as extraordinary transmission phenomenon (EOT) [24, 87]. The origins of EOT and the role of SPPs in this phenomenon is a debatable topic suggesting several additional mechanisms behind the process, including contributions of localized surface plasmons [88], effect of Wood's anomaly, waveguide modes, etc. [89–92]

As an example, let's consider a structure consisting of a metal film with nanoholes assembled in a hexagonal two-dimensional pattern (Figure 2.7), as will be further employed in chapter 5.2. Another assumption includes only pure SPP excitation without considering multiple resonances originating from Fabry-Perot cavities [93], SPP molecule effects, and others [91].

As mentioned above, the lattice contributes an additional component \vec{G} to the wave vector of incident light \vec{k}_{\parallel} enabling coupling between SPPs and light (Figure 2.7), which can be expressed in the following equation 2.16).

$$\vec{k}_{spp} = \vec{k}_{\parallel} + m \cdot \vec{G}_x + n \cdot \vec{G}_y \quad (2.16)$$

where \vec{k}_{spp} being the wave vector of SPP that is described by a propagation constant β in the dispersion relation 2.15, \vec{k}_{\parallel} stands for the light wave vector component projected on the x - y plane, m and n are integers defining the corresponding mode. Furthermore, the relation 2.16 can be expressed using the dispersion relation 2.15 as follows:

$$\frac{2\pi}{\lambda} \sqrt{\frac{\epsilon_d \epsilon_m}{\epsilon_d + \epsilon_m}} = |n_0 k_0 \sin(\theta) + m G_x + n G_y| \quad (2.17)$$

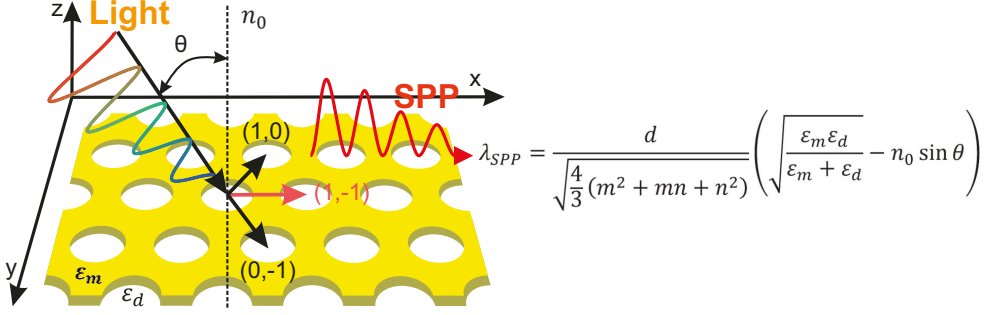


FIGURE 2.7: Schematic drawing of the SPP excitation via hexagonal nanohole arrays showing coupling between incident light and surface plasmons in the gold. The wavelength of the SPP resonances (λ_{spp}) is defined by formula 2.18

where λ is the wavelength of the incident light in vacuum, ϵ_d and ϵ_m are relative dielectric permittivities of the dielectric and the metal, respectively, n_0 denotes the refractive index of the medium, where the light propagates. It can be shown [94, 95] that taking into account a hexagonal assembly of nanoholes with the reciprocal vector $|\vec{G}| = \frac{4\pi}{\sqrt{3}d}$ the position of SPP, λ_{spp} , can be expressed as follows:

$$\lambda_{spp} = \frac{d}{\sqrt{\frac{4}{3}(m^2 + mn + n^2)}} \left(\sqrt{\frac{\epsilon_d \epsilon(\omega)_m}{\epsilon_d + \epsilon(\omega)_m}} - n_0 \sin \theta \right) \quad (2.18)$$

with d being the pitch between two neighboring holes (lattice constant).

Equation 2.18 can be simplified considering a zero-order configuration ($\theta = 0$), which results in:

$$\lambda_{spp} = \frac{d}{\sqrt{\frac{4}{3}(m^2 + mn + n^2)}} \sqrt{\frac{\epsilon_d \epsilon(\omega)_m}{\epsilon_d + \epsilon(\omega)_m}} \quad (2.19)$$

In contrast, if a square assembly of nanoholes is considered [96], which is a common pattern for standard lithography fabrication techniques, the reciprocal lattice vector of the grating turns to $|\vec{G}| = \frac{2\pi}{d}$ which leads to the following relation:

$$\lambda_{spp} = \frac{d}{\sqrt{(m^2 + n^2)}} \sqrt{\frac{\epsilon_d \epsilon(\omega)_m}{\epsilon_d + \epsilon(\omega)_m}} \quad (2.20)$$

Furthermore, despite the rough approximations used for deriving formulas 2.18 and 2.20, it is still worth noticing that the surface plasmon properties of nanohole arrays can be tuned by altering the lattice constant maintaining the same metal-dielectric interface.

2. Fundamentals

Additionally, it is possible to observe multiple resonances depending on the combination of integers m and n .

Moreover, due to the direct dependence of the position of SPP, λ_{spp} , with the dielectric permittivity of the medium, the nanohole arrays have gained widespread usage in sensing techniques.

Additionally, the optical properties of SPPs excited via nanohole arrays are correlated with their geometrical features, which are neglected during deriving formulas 2.18 and 2.20. In particular, the lifetime of SPPs depends on the resonant wavelength and the hole geometry [97]. While the hole radius increases the lifetime of SPP shortens leading to changes in optical spectrum and electrical field decay length.

Noteworthy, the optical properties of the nanohole arrays may originate from the coupling between localized surface plasmons created by the holes and surface plasmon polaritons. A strong concentration of optical modes was observed around the holes with the help of the active near-field nanoprobe [88].

2.3 STATE OF THE ART

The areas of molecular electronics and plasmonics have been studied intensively over the last decades enabling the realization of functional devices like sensors, transistors, switches, and others. In particular, to fulfill the spectrum of applications of optics and optoelectronics, molecule-based devices lead to the development of e.g. optical switches [98, 99], memory elements [100–102], and transistors [74], while surface plasmon based platforms allow e.g. the detection and imaging down to single-molecule level [103]. Furthermore, the connection of these two areas [104] lead to the novel concepts of coupling between molecular orbitals and plasmonic energy levels [105], and surface plasmon-enhanced molecular switching as introduced in [106].

2.3.1 MOLECULAR OPTOELECTRONIC SWITCHES

In recent years, a broad spectrum of studies has been conducted to address the molecular switching external light stimuli [1]. Among various photochromic molecules, azobenzenes and diarylethenes introduced themselves as good candidates for photoswitching contacts, and, therefore, have been intensively employed as a functional unit in molecular junctions.

Since the transition between isomer states during photoswitching is controlled by input light energy, it is essential to use a transparent electrode for the molecular junctions such that light can be efficiently absorbed by the molecular layer [55, 107]. To fulfill these requirements, graphene electrodes have been proposed providing suitable chemical stability, transparency, and compatibility. Additionally, graphene provides mechanical flexibility, which may extend the applications of optical molecular switches to wearable electronics [108]. For instance, the fabricated molecular junctions based on soft contacts between graphene electrodes and azobenzene molecules showed reversible photoinduced tunneling transport between *cis*- and *trans*-isomers [55]. Moreover, the reversible conformational changes in the azobenzene SAMs were repeatedly observed with the change in current density without significant degradation (over more than 50 photoswitchable cycles). This makes graphene a suitable candidate to serve as transparent and conductive electrodes for molecular photoswitch devices.

Another promising and widely discussed approach to achieve bidirectional photoswitching of molecular species is using conductive PEDOT:PSS interlayers. For instance, diarylethenes were incorporated in such geometry revealing around one order magnitude difference in current density with the external UV-vis stimuli [20]. In this case, the large-area molecular junction was fabricated with a 90 nm-thick PEDOT:PSS electrode, and an auxiliary semitransparent 20 nm-top gold contact. Noteworthy, PEDOT:PSS allowed thermal evaporation of the gold onto the junctions without damaging the molec-

2. Fundamentals

ular species. Even though the 20 nm thickness of the gold was conductive enough to support electron transport, the optical transmission was approximately 20-50%, which pronouncedly reduces the switching efficiency.

2.3.2 PHOTOCROMIC MOLECULE-BASED PLASMONIC STRUCTURES

The surface plasmon-induced electric field confinement has been employed in various fields including such techniques as Surface-Enhanced Raman [13] and Plasmon-Enhanced fluorescence spectroscopy [103]. For instance, the latter one due to the coupling of the fluorophores in their excited states with localized surface plasmons enables the imaging and detection down to a single molecule.

Furthermore, quantum emitters such as excitons in J-aggregates, quantum dots, and dye molecules can support strong coupling to surface plasmon polaritons resulting in new hybridized light-matter states [105, 109]. J-aggregate molecules or organic dyes (e.g. Rhodamine 6G) possess a decent sharp absorption peak exhibiting a resonance nature. The coupling of such resonators to surface plasmons led to the formation of two separated resonances with so-called Rabi splitting [110].

Moreover, it was reported that the strong coupling between dye molecules and the plasmon modes induced the enhancement of the Raman signal from the dye [111]. In this report, the resonant coupling was observed between localized surface plasmon resonances in nanostructured silver films and an adsorbed monolayer of Rhodamine 6G dye. The maximum Raman response was observed when a polariton mode matched the Stokes shifted emission band of the dye.

While being an active component of molecular electronic devices, a coupling between photochromic molecules and surface plasmons has been also realized introducing novel optical features [112, 113]. Even though the photochromic molecules exhibit broader extinction peak in comparison with dyes, the reversible strong coupling was observed exhibiting prominent Rabi splitting [114, 115].

Furthermore, plasmonic nanoantennas were designed incorporating silver nanocubes separated from a silver film by a composite spiropyran and polymethyl methacrylate (PMMA) [116]. This hybrid structure based on photochromic molecules enabled dynamic tuning of plasmon resonances up to 71 nm through multiple cycles.

Active and reversible control of the plasmonic phase and group propagation was realized using photochromic molecules mixed with a dielectric matrix. This demonstrated the potential for the construction of remotely controlled plasmon-optical devices e.g. switchable plasmonic lens [117].

CHAPTER 3

MATERIALS & METHODS

3.1 FABRICATION AND CHARACTERIZATION METHODS

The field of micro and nanostructuring has been developing for decades consequently consisting of various methods and tools to achieve nanosize features [118]. By combining lithography with other fabrication processes such as deposition and etching, a high-resolution topography can be achieved, while this cycle may be repeated several times to form complex micro and nanoscale structures.

In order to fabricate nanohole arrays, bottom and top electrodes of the crossbar configuration, a combination of photo, e-beam, and nanosphere lithography (NSL) was employed. Furthermore, the structuring was carried out by wet etching, RIE, and ALD, while characterization was performed by SEM and AFM.

3.1.1 LITHOGRAPHY

Generally, lithography techniques are divided into two groups such as maskless and masked lithography. On the one hand, photolithography is an example of the latter one and has become a facile and conventional technique, which enables to fabricate structures beyond the optical diffraction limit within the microns range. On the other hand, to successively downsize the fabrication a maskless electron-beam, nanoimprint or NSL can be employed to overcome the photolithography constraints.

Photolithography

Briefly, the photolithography technique utilizes the exposure of a light-sensitive polymer (photo-resist) to ultraviolet light through a photomask to define the desired pattern.

3. Materials & Methods

A fabrication workflow usually starts with the deposition of a resist onto a substrate. Spin-coating is the common approach of resist deposition, which results in a superior homogeneous layer spread throughout the whole surface, followed by soft baking to minimize the remaining solvent concentration. In this case, the combination of resist viscosity and rotation speed determines the resulting thickness. Generally, photoresists themselves are composed of a polymer matrix and a photosensitive chemically active component. Under the light exposure, the photoactive components are strengthened and degraded in the case of negative and positive tone resist, respectively. Here, positive AZ5214E (Microchem Corp., USA) and negative nLOF2020 (Microchem Corp., USA) resists were utilized.

The exposure is performed commonly at defined wavelengths of 436 nm ("g-line"), 405 nm ("h-line"), and 365 nm ("i-line"). The latter wavelength is employed by a Mask Aligner (Süss Microtech AG, Germany) which was used in this work. The whole wafer surface is exposed, while an opaque metal photomask blocks light and shadows areas of the resist, leading to a selective photochemical change in defined parts of the resist. If the contact mode is applied, where the photomask is in contact with or in close proximity to the photo-resist, the resolution of the projection is directly limited by the wavelength and the ability of the optical system to capture enough diffraction orders from the illuminated mask. Therefore, an approximate minimum feature size (Δm) is given by the following equation:

$$\Delta m = k \frac{\lambda}{NA} \quad (3.1)$$

where NA is the numerical aperture of the lens and the coefficient k is defined by process-related factors and from classical theory determined as 0.61 by the Rayleigh criterion [78].

Depending on the resist type, two different kinds of photomasks are used such as light and dark field masks. Both can be applied to positive and negative tone resists, depending on the structure design. However, the combination of positive resist and dark field mask is preferably used to achieve higher resolution by capturing more diffraction orders.

The exposure can be followed for some resists by so-called post exposure bake. It smoothes out the concentration distribution of photoproducts leading to a homogeneously developed pattern. The subsequent step of developing (here, by MIF326 developer (Microchem Corp., USA)) removes soluble areas.

The following steps can be combined with deposition or etching of material through the resist pattern to obtain complex structures.

Electron-beam lithography

To overcome the aforementioned optical diffraction limitations of photolithography, electron-beam lithography can be used employing a focused electron beam to expose the resist [119]. Photoresists can be treated by electron beams leading to the same results as with light. For instance, a nLOF2020 negative resist is employed efficiently for both techniques. However, the best results can be achieved with the resist specifically designed for electron-beam lithography demands. Here, positive tone resists polymethyl methacrylate (PMMA) ARP639.04 50K, and AR-P649.04 200K (Allresist GmbH, Germany) were employed for electron-beam writing.

The focused electron beam enables to achieve a resolution, which is theoretically defined by the De Broglie wavelength of the electrons and can be approximately calculated based on the following equation:

$$\lambda[\text{nm}] \approx \frac{1.23}{\sqrt{V[\text{V}]}} \quad (3.2)$$

where V is the applied acceleration voltage. However, there are several factors, which dramatically affect the resolution. Firstly, to prevent a significant feature displacement, a resist charging should be avoided. A silicon oxide (SiO_x) (4" Si wafers with 400 nm of oxide grown on top) supports enough grounding for electrons, unlike other materials (e.g. transparent quartz substrate).

The ultimate resolution is also limited by beam-to-matter interactions, which appear in forward and backscattering of electrons. This phenomenon is called the proximity effect and seriously reduces the practical resolution. Additionally, the technique is not suitable for big pattern manufacturing due to the longer writing time in comparison with photolithography. Despite the aforementioned restraints, e-beam lithography enables a resolution of sub 10 nm, which allows to fabricate various nanostructures with versatile designs. Here, a Vistec EBPG 5000+ HS electron-beam machine was employed operating with the acceleration voltage of 100 kV and a dose of 375 $\mu\text{C}/\text{cm}^2$.

Nanosphere lithography (NSL)

NSL [120–122], also known as colloidal lithography [123, 124], has been introduced as an alternative to aforementioned techniques like photo and e-beam lithography, especially for producing structures with defined long-range periodicity. The NSL has attracted great interest due to its compatibility with wafer-scale processes as well as its potential to manufacture a wide variety of homogeneous one-, two-, or three-dimensional nanostructures.

Generally, the workflow of NSL is divided into two steps. The first step is the assembly of nanoparticles onto the substrate via e.g. interfacial assembly (see section 4.1). The composition and size of the particles can differ depending on the fabrication steps.

3. Materials & Methods

The substrate itself can be patterned, for instance, with either photoresist [125] or other templates to support selective particle deposition. Additional layers of particles can be deposited to create complex 3D structures. The second step involves the modification of geometrical features such as e.g. particles' size, localization, and shape followed by structuring processes [126] like e.g. dry etching and metal deposition. The latter one can be modified by tuning the glancing angle deposition to produce various novel designs of 3D nanostructures [127]. The particles are easily synthesized utilizing typical polymer materials which makes them also commercially available. In this work, polystyrene (PS) particles were purchased from Bang Laboratories Inc., USA. The particles' dispersions are composed of PS beads dissolved in the aqueous medium in the concentration of solids around 10%. The PS beads possess functional carboxylic groups (-COOH), which cover particles with low surface density ($<35 \text{ \AA}^2$ per group).

3.1.2 CHEMICAL ETCHING & DEPOSITION

Etching of the material is one of the most crucial and commonly employed ways of nanostructuring, enabling a selective transfer of a designed pattern. There are two types of etching processes named dry and wet chemical etching, which exhibit essential differences [128]. During wet chemical etching, the material is etched by the diffusion of active components via liquid phase, whereas dry etching utilizes electromagnetic fields to direct reactants to the material. Therefore, when a material is etched by a liquid, the exposed parts are generally removed isotropically, while on the other hand directed electromagnetic fields can support anisotropic etching. In this case, for instance, a developed photoresist can play a role of a shadow mask for selective etching or other hard masks can be used (e.g. chromium, aluminium).

Wet chemical etching

A high degree of anisotropy is desired in etching processes to assure an accurate transfer of the mask pattern. The isotropic nature of wet etching leads to a widening of the mask pattern. Therefore, sub-microns resolution features are hard to fabricate. However, despite the resolution limitations of wet etching, it has found widespread use because of its low cost, high reliability and throughput, and excellent selectivity with respect to both mask and substrate materials.

Generally, the wet etch process can be described by three basic steps. The first one is diffusion of the liquid etchant to the structure that is aimed to be removed. The second step involves usually a reduction-oxidation (redox) reaction between the etchant and the

material which entails the oxidation of the latter one. The final step is the dissolution of the oxidized material followed by diffusion of the byproducts from the reacted surface.

Here a wet chemical etching was employed to selectively etch metals such as gold and titanium. Gold belongs to noble metals, therefore, the removal of this material requires a strong oxidizer for the separation of the unpaired valence electrodes. For this reason, iodine can be employed to support the following chemical reaction:



The gold etchant TechniEtch ACI2 (Microchemicals GmbH, Germany) was employed containing a mixture of KI and I₂. KI is added to improve the solubility of AuI.

Since a slow etching process is easier to operate and tune, a stock solution of TechniEtch ACI2 was dissolved in water by a 1:1 ratio to reduce the concentration of the reactants. This led to a dramatic drop in the etching rate from approx. 1000 to 50 nm/min.

Titanium was used as an adhesion promoter between gold and the substrate. Titanium forms a very stable oxide layer in the air. It can be etched by hydrofluoric (HF) acid, which is, therefore, often a component of titanium etchants. Here, in order to etch titanium, the etchant TechniEtch TC (Microchemicals GmbH, Germany) was employed, which contains the following components in a ratio HF:H₂O₂:H₂O = 1:1:20. In this mixture H₂O₂ oxidizes layer by layer the titanium which is further etched by HF.

Reactive Ion Etching (RIE)

RIE is an example of a powerful dry etch method [129], which facilitates nanostructuring enabling an accurate anisotropic etching of down to nanosize features. The main concept relies on the usage of plasma generated under low pressure, which contains high-energy ions.

Generally, the system consists of the vacuum chamber where the wafer is placed on the lower electrode connected to the power source (Figure 3.1). The gas composition depends on the material to be etched and in order to obtain high etch rate supports not only chemical but also physical reactions to remove parts of material from a substrate. The plasma itself is ignited by a radio frequency (RF) electromagnetic field at 13.56 MHz and can be combined with inductively coupled plasma (ICP) sources to provide a high ion density and, therefore, increase the rate of etching. Thus, anisotropic nature of etching is supported by the directionality of the ions accelerated towards the negatively biased substrate by electromagnetic field sources.

An Oxford Plasmalab 100 (Oxford Instruments plc, Great Britain) was employed containing both RF and ICP sources (Figure 3.1). The maximum power provided by the RF

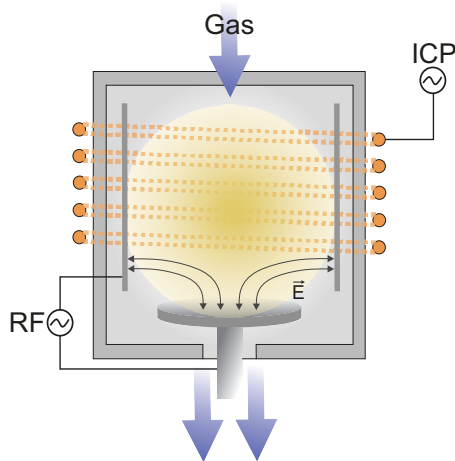


FIGURE 3.1: Sketch representing a general working principle of the RIE machine Oxford Plasmalab 100 based on a RF- and ICP coupled service.

source is 200 W, while the ICP can support up to 2000 W. The electrode where the wafer is placed is connected to the liquid nitrogen cooling system, while a helium air cushion provides a sufficient heat transfer. Therefore, the system prevents overheating, which is beneficial for temperature sensitive materials, such as e. g. PS beads.

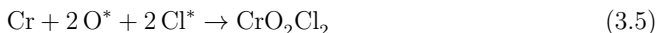
In order to etch SiO_x and quartz, a combination of the gases Ar and fluoroform (CHF₃) was chosen in a ratio of 30:5 sccm (the detailed protocol is described in A.1). The latter gas contains fluorine (F), which chemically reacts with SiO₂ leading to the formation of unstable products following the reaction:



The chemical etching was supported by a physical ion bombardment via Ar ions facilitating the uniform etching process.

To etch the PS particles, a combination of oxygen (O₂) and fluoroform CHF₃ was employed in a ratio of 40:10 sccm. Oxygen is the main component, which chemically oxidizes the PS, whereas CHF₃ was added as a reactive component to make the etching process more homogeneous by removing the carboxyl functionalization of the particles and possible carboxylate ions on the PS surface during the oxidation. The temperature was kept at 0°C to prevent possible melting.

The chromium (Cr) metal layer was etched utilizing a mixture of the two gases Cl₂ and O₂ in a ratio of 30:20 sccm following the reaction:



where O^* and Cl^* are reactive species generated in the ionized plasma, while CrO_2Cl_2 is volatile in the plasma environment and is pumped out with the exhaust gases.

Atomic Layer Deposition

Atomic layer deposition (ALD) is a vapor phase technique capable of producing thin films of a variety of materials via chemical surface reactions [130]. Generally, the process flow consists of sequential alternating pulses of gaseous chemical precursors that react with the substrate. Once the whole surface is covered by a monolayer of the components of the first gas, it is pumped away and a second gas is introduced that also condenses and is chemisorbed on top of the first layer. The sequence repeats to deposit layer by layer that can be controlled by number of cycles to achieve an aimed thickness. The ALD technique allows to deposit ultra thin defect-free films with complex 3D conformity.

The materials that can be deposited by ALD include e.g. transparent conductive oxides, dielectrics, diffusion barriers, and photocatalytically active coatings. Here, a FlexAL II ALD machine (Oxford Instruments, Great Britain) was employed to deposit Ta_2O_5 film.

3.1.3 SURFACE ANALYSIS

The fabrication of nanofeatures requires a proper analysis demanding high-resolution imaging and surface characterization, which can be provided by e.g. Scanning Electron Microscopy (SEM) and Atomic Force Microscopy (AFM), respectively. While SEM is employed to visualize nano and micro size features, AFM offers not only atomic scale imaging, but also nanomanipulation and insights into molecule-surface interaction, etc.

Atomic Force Microscopy

Atomic Force Microscopy (AFM) is a powerful and multifunctional imaging tool that enables characterization and visualization of surface topographies with sub-nm resolution [131]. Due to the mechanical nature of the operating principle, it allows imaging various nanosize objects without constraints on material properties including even biological samples from single molecules to living cells [132].

An AFM technique utilizes a cantilever with a sharp tip to scan over a sample surface. It offers a multitude of different measurement modes e.g. Contact Mode and Tapping Mode. The latter one enables a high topographical resolution preventing the damage of the surface by avoiding the direct continuous tip-surface contact, which is beneficial, in particular, for biological samples or soft molecule films.

In tapping mode, the tip is driven to oscillate with the frequency close to its resonance value. As the tip approaches the surface, the close-range atomic force between the surface

3. Materials & Methods

and the tip causes the cantilever to alter the oscillation amplitude. These changes are monitored by laser beam reflection enabling precise tracking by a photodetector. The oscillation amplitude is then measured and used as the input to the electronic feedback loop. The loop adjusts the relative height position by maintaining the amplitude constant translating the collected information into a topographic image.

Furthermore, the tapping mode can give more details about surface properties, in particular, the stiffness, since the change in oscillation frequency can be translated into a phase image.

To characterize the topography of C₅FHSAc films and the nanohole arrays surfaces, a Bruker Nanoscope V Multimode AFM setup was employed equipped with RTESPA-150 cantilevers (Bruker Nano Inc, Camarillo, USA).

Scanning Electron Microscopy

A Scanning Electron Microscopy is a great alternative to AFM for high-resolution nanoimaging in a versatile and relatively quick way. Similar to the electron-beam lithography (see section 3.1.1) the main principle of this method relies on the scanning of the surface by focused electron beam, which practically allows imaging of the objects with the resolution down to approx. 1 nm (at Zeiss Gemini 1550).

A primary electron beam is generated in vacuum conditions and accelerated by a voltage to the sample surface. As the beam reaches the substrate it penetrates the material and specific collisions lead to the production of Auger, secondary, and backscattered electrons together with characteristic, continuum, and fluorescent X-rays. Each of these collisions can be captured by a detector and translated into an image.

A Zeiss Gemini 1550 scanning electron microscope was utilized to image the nanohole array surface and PS particles, employing the secondary electron and in-lens detectors, which detect secondary electrons (SEs) and both secondary and backscattered electrons (BSEs), respectively. The SEs originate from the near-surface regions and exhibit lower energy than BSEs enabling better surface topography imaging. On the other hand, BSEs originate from deeper material regions, which, therefore, brings additional information on the atomic composition. This results in better contrast for output imaging.

The surface imaging here was carried out mostly by the in-lens detector, except for images taken at an angle, since in this case the focus distance could not be small enough to support proper in-lens detection. The applied acceleration voltage was 15 and 20 kV. To avoid the bleaching effect caused by surface charging, a conductive layer is required. Therefore, for such substrates e.g. PS particles and quartz, a thin layer of iridium (Ir) was sputtered with a thickness of around 2 nm.

3.1.4 PREPARATION OF THE C₅FHSAC FILMS

Here, in order to carry out the electrical and optical measurements of C₅FHSAc molecules, the film was deposited onto substrates (bottom electrodes, Au and quartz surfaces, nanohole arrays) by means of spin-coating. The solid C₅FHSAc molecules were dissolved in chloroform (CHCl₃) resulting in a 2 mM concentration. To test the thickness dependence of the solid film, additional concentrations of 1 mM, and 5 mM were obtained. Before the deposition, the substrates were cleaned in an oxygen plasma with a pressure of 0.7 mbar and a power of 200 W for 5 min. Subsequently, the Au substrates were immersed in ethanol for 5 min to allow oxide reduction. 60 μ l of 2 mM molecules solutions were spin-coated onto the surface at 300 rpm for 90 sec.

For live switching tests (see section 5.4.2), before the spin-coating the electrodes were immersed in C₅FHSAc solution overnight to support self-assembling of the monolayer.

3.2 OPTICAL MEASUREMENTS

Here in order to convert molecules between two states, a light source (Newport, USA) containing a 150 W Xe-lamp was employed. Since the Xe-lamp generates both UV and visible light, a 400 nm long-pass filter (Thorlabs, USA) was utilized to open the molecules and a 380 nm band-pass filter with full width at half maximum (FWHM) (10 ± 2) nm (Thorlabs, USA) to initiate the closing reaction (Figure 3.2). To record the irradiation

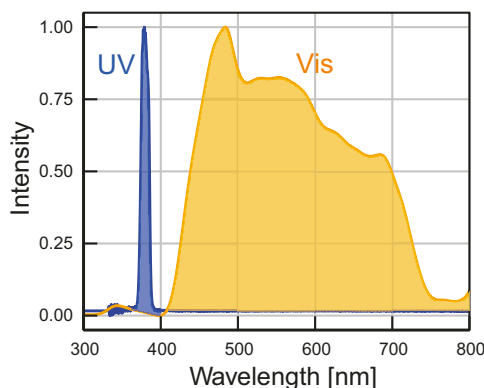


FIGURE 3.2: Normalized irradiation spectra of the light source that was used in order to open (Vis light, orange) and close (UV light, blue) the film. The spectra were filtered with low-pass filter to remove sharp irradiation spikes in the visible range.

spectrum of the light source, a mobile spectrometer CCS200/M (Thorlabs, USA) was used in combination with an optical fiber connected to a CCSA2 cosine corrector (Thorlabs, USA). The light source was equipped with an optical fiber that enabled to guide light directly to the corrector. Depending on the intensity of the output light, different integration times were used to obtain the best signal-to-noise ratio. As a result, the light source irradiates a broad white spectrum in the range $\sim[450 : 750 \text{ nm}]$ for the opening process exhibiting a narrow UV peak at 379 nm for the reverse closing reaction with full width at FWHM of around 11 nm.

The intensities of both UV and white light were measured employing a compact power and energy meter PM100D (Thorlabs, USA). The intensity of the UV light was revealed to be around 0.74 W/m^2 , while visible light appeared to be approx. 72 W/m^2 . The energy meter was equipped with a UV extended silicon photodiode detector S120VC (Thorlabs, USA) and mounted in the holder near the reflective mirror, where the testing samples for kinetic measurements were supposed to be placed.

In order to fully control the time and, thereby, the illumination dose, the light source was equipped with an electronic shutter (Newport, USA) that was controlled via a PC. The shutter blade exhibits a rise/fall time of 0.1 sec and the minimum exposure time was

set to be 1 s for kinetic measurements. The spectra were recorded in 1 nm steps for all ranges employing a high precision Perkin Elmer Lambda 900 spectrometer (Perkin Elmer, USA).

3.3 ELECTRICAL MEASUREMENTS

In order to measure the sheet resistance of the fabricated nanohole arrays and compact Au, a 4200A-SCS parameter analyzer (Keithley Instruments, USA) was employed. The analyzer was connected to a 4-point probe station. The 4 probes were applied to the surface and the Van der Pauw method [133] was utilized in order to obtain the sheet resistance.

To characterize the current density distribution for open and closed molecular species captured between the bottom and top crossbar electrodes, 2 probes were employed to record current-voltage (I-V) curves for each junction (Figure 3.3 a). The voltage was operated in sweeping mode starting from 0 V.

To test a live electrical switching of molecular species, a sample was placed onto a metal holder containing a UV extended mirror. The light from the source was guided via the optical fiber to the holder, where it is directly transmitted to the sample via the mirror (Figure 3.3 b).

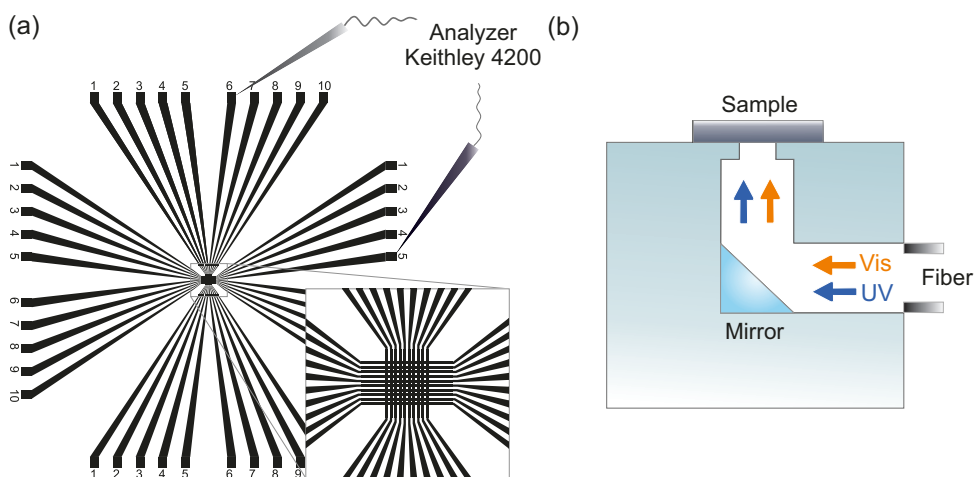


FIGURE 3.3: (a) The schematic drawing representing electrical measurements of C_5FHSAc film sandwiched between top and bottom electrodes in a crossbar configuration. Each of the 100 junctions can be addressed by applying a voltage between a pair of bottom and top leads. (b) Sketch showing a holder that supports live-switching electrical measurements. The light is guided via an optical fiber to the holder, reflected by a mirror that directs the light to the sample.

3.4 SIMULATIONS

Simulations provide a unique environment and a powerful tool to anticipate and estimate behavior of a decent system. The working flow of each simulation is straightforward and is described by the following steps: define the geometry, select materials and suitable interface, set mesh and boundary conditions, select a solver and visualize the results.

3.4.1 FDTD SIMULATIONS

The finite-difference time-domain (FDTD) method [134, 135] conceptually and in terms of implementation is one of the most versatile full-wave techniques used to solve problems in electromagnetics firstly introduced by Yee in 1966 [136]. It is convenient and powerful tool for modeling nano and micro-scale optical devices ranging from waveguides and antennas to nanoparticles and oscillators. The method is typically used when the feature dimensions are in similar size order as the working wavelength and is able to model various of optics related processes such as light propagation, scattering, diffraction, absorption, reflection and polarization effects etc.

The main concept of FDTD relies on solving Maxwell's equations (3.6) directly without any physical approximation in complex geometries making the calculation accurate and versatile.

$$\begin{cases} \frac{\partial \vec{D}}{\partial t} = \nabla \times \vec{H} & (3.6a) \\ \vec{D}(\omega) = \epsilon_0 \epsilon_r(\omega) \vec{E}(\omega) & (3.6b) \\ \frac{\partial \vec{H}}{\partial t} = -\frac{1}{\mu_0} \nabla \times \vec{E} & (3.6c) \end{cases}$$

where \vec{H} , \vec{E} , and \vec{D} correspond to the magnetic, electric, and displacement fields, respectively, while ϵ_r is the complex relative dielectric constant.

It is a volume-based method, therefore, it demands dividing the space of the working interface into a uniform mesh of Yee cells (Figure 3.4), where \vec{E} and \vec{D} field components are determined at grid points by solving the equations 3.6.

Unlike other simulation methods used for electromagnetics such as e.g. finite element method (FEM) where the time dependence is eliminated, FDTD employs both spatial and temporal discretization. Time is quantized into small steps, where each step represents the time required for the field to travel from one cell to the next. The electrical field is solved at a given instant in time, then the magnetic field is solved at the next instant in time, and the process is repeated over and over again.

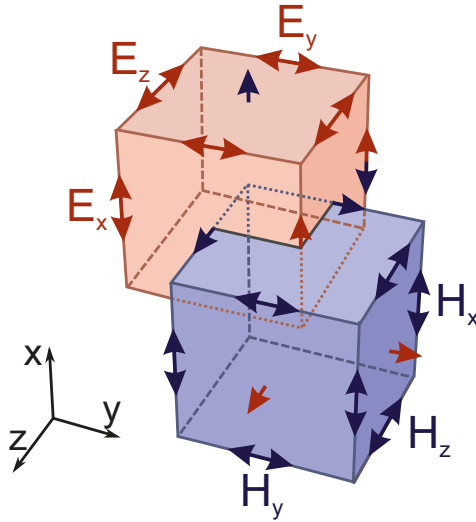


FIGURE 3.4: Sketch representing a Yee cell used for FDTD simulation. The field \vec{E} and \vec{H} components are interlaced at space and time intervals for the purpose of implementing a leapfrog algorithm.

For obtaining meaningful results keeping the stability of the method, the electromagnetic field should not change significantly over an increment, which, therefore, brings basic constraints on the step size for both space and time (equation 3.7).

$$\begin{cases} \min(\Delta x, \Delta y, \Delta z) = \frac{\lambda_{min}}{10 \cdot n_{max}} & (3.7a) \\ \Delta t \leq \frac{1}{\nu_{max} \sqrt{\frac{1}{(\Delta x)^2} + \frac{1}{(\Delta y)^2} + \frac{1}{(\Delta z)^2}}} & (3.7b) \end{cases}$$

where Δx , Δy , Δz correspond to the mesh size, λ_{min} is the minimum wavelength used in the simulation, n_{max} denotes the maximum refractive index, while ν_{max} is the maximum light velocity in the computational domain. Practically this means that the shortest wavelength should contain at least 10 cells. Once the mesh size (Δx , Δy , Δz) is chosen following the condition 3.7a, a time increment follows the Courant-Friedrichs-Levy condition 3.7b.

In order to simulate the optical response and electrical field distribution within the cross-section of nanohole arrays and ordered layers of PS beads, a FDTD package from Ansys Lumerical Inc. (Vancouver, Canada) was utilized. The software includes a large variety of available materials in the default database. Since the majority of materials (e.g. metals) exhibit a complex behavior of electrical permittivity within a wide frequency

range, a suitable model is required to describe it. Most of the alternative simulators exploit models such as Drude, Debye, and Lorentz, etc., which were originally derived from simplified models of the permittivity of idealized materials. Thereby, fundamentally they cannot fully simulate real object properties. In contrast, Lumerical offers a multi-coefficient model to enable an accurate broadband material simulation. The model enables a small tolerance in the fitting of dielectric permittivity leading to a more accurate material model.

Moreover, any dispersive material with tabulated real and imaginary parts of refractive index or permittivity can be fitted within a broad range of wavelengths enabling a proper simulation. Here, to obtain the continuous spectrum of the refractive index of the C_5FHSAc molecular film, a multi-coefficient model was applied, which showed a good agreement with a small error of fitting. The typical materials such as titanium, gold, and quartz were taken from the default Lumerical database, where the same multi-coefficient model is employed to generate the data of electrical permittivity.

The experimental optical spectra were recorded here in the transmission configuration, meaning that only the intensity of light which passed through a material is measured by a photodetector disregarding reflected light. The same interface configuration was built in the simulation space of Lumerical (Figure 3.5). The source of light was positioned

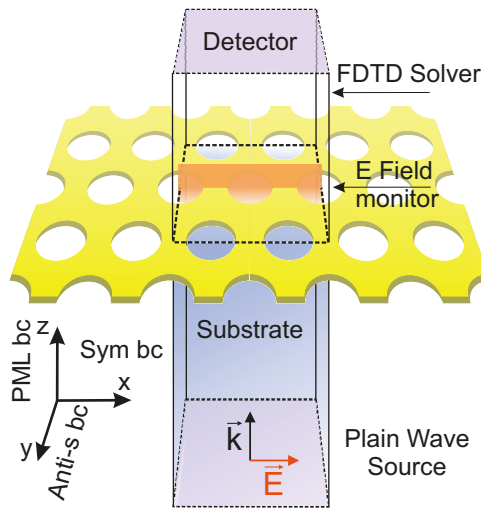


FIGURE 3.5: Schematic drawing representing the FDTD simulation working space containing gold nanohole arrays on quartz substrate.

behind the material and directed perpendicularly to the sample surface along the z axis. The source of light was chosen as a plane wave source with amplitude 1 V and linearly polarized electrical field along the x axis. The substrate (quartz) was positioned between

the light source and the sample (nanohole or PS beads arrays), while the detector was located above the aforementioned components.

The arrays exhibit hexagonal periodicity along the x and y axes. Therefore, in order to simulate the whole structure, only a single computational unit is sufficient together with periodical conditions along axes. The unit corresponds to the rectangle with two sides of $2 \cdot L$ and $\sqrt{3} \cdot L$, where L is the pitch between the centers of two neighboring nanoholes or beads. Since the electromagnetic fields through a structure have a plane of symmetry in the middle of a hexagonal period, the periodic boundary conditions were replaced with symmetric (Sym bc, Figure 3.5) and antisymmetric ones (Anti-s bc, Figure 3.5) for the x and y axis, respectively, allowing to reduce the simulation time by a factor of 8 maintaining the same conditions. The conditions for the z axis were chosen as perfectly matched layer (PML, Figure 3.5).

The mesh size varied for each simulation depending on the dimensions of the structure. To obtain the distribution of electrical fields in a cross-section of nanohole and PS beads arrays, the monitor was placed perpendicularly to the sample surface along the x - z plane. The resolution of the obtained field directly correlated with the mesh size, since the field's values were determined in the nodes of the grid.

3.4.2 FINITE ELEMENT METHOD (FEM)

The Finite Element Method (FEM) is a typical tool to simulate fluid-structure interaction, thermomechanical problems, mass transport, electromagnetic properties, etc [137]. The basic concept of FEM involves discretizing a computational space into discrete elements, where for each element the method determines the field solution with simple linear or quadratic equations that are solved simultaneously for the complete system. Many physical process laws, as well as Maxwell's equations (3.6), can be expressed as partial differential equations and, therefore, solved by FEM.

Here, in order to determine the electrical resistivity of nanohole arrays depending on the hole diameter, the COMSOL Multiphysics 5.4 numerical software was employed equipped with the AC/DC module that uses FEM.

From a classical perspective, Ohm's law gives the resistance of a macroscopic uniform conductor $R = \rho \frac{L}{S}$, where ρ denotes the resistivity, L is the conductor length, S stands for the cross-sectional area. On the other hand, the local form of Ohm's law (equation 3.8) is valid under the same conditions at any point of the conductor.

$$\vec{j} = \frac{1}{\rho} \vec{E} = \sigma \vec{E} \quad (3.8)$$

where \vec{j} is the current density, σ is the conductivity, \vec{E} denotes the electrical field. The package solves the differential form of Maxwell's equations together with initial and boundary conditions. Therefore, all variables equation 3.8 can be simulated to define the local current density. Then the overall resistance is determined by integrating all values along the working area.

CHAPTER 4

SAMPLE FABRICATION & CHARACTERIZATION

4.1 FABRICATION OF NANOHOLE ARRAYS

There are various techniques exploited to fabricate metal films perforated with periodic arrays of nanoholes (nanohole arrays). For instance, electron-beam lithography was used to produce nanohole arrays for high-precision sensing [138], while focused ion milling enabled unique designs of hole arrangement [139]. Even though these techniques facilitate the nanofabrication, they are expensive and time-consuming, which, therefore, hampers large-scale and low-cost wafer-scale fabrication.

To overcome these limitations, soft lithography was utilized including nanoimprint [140] and NSL (section 3.1.1). The latter one is capable of patterning large areas of nanoholes with sufficient quality due to the manipulation of colloids with sizes ranging from several nm to μm . This advantage made NSL a good candidate as a cheap method for the fabrication of plasmonic films [141].

4.1.1 NANOSPHERE LITHOGRAPHY (NSL)

The fabrication of nanohole arrays by nanosphere lithography relies on the deposition of a monolayer of PS beads onto a sample, reducing the size of the particles by means of RIE (see chapter 3) and subsequent metal evaporation on top. The beads themselves are exploited as a shadow mask for metallization forming nanohole arrays are, where the lattice constant is defined by the initial diameter of the beads, and the size of the holes fits the diameter of the particles after RIE. Depending on the size of the particles, the coverage

4. Sample fabrication & characterization

area and other factors including the envisaged resulting quality, the nanobeads can be deposited by means of several techniques like spin-coating [142] and water-air interface assembly [143] (e.g. Langmuir - Blodgett [144]). The latter one is not only capable of proving sufficient quality of close hexagonal layers of particles, but also facilitates upscaling the fabrication of nanohole arrays to wafer size.

Interfacial Assembly

In this work, a modified liquid-air interface assembly technique named Funnel Assisted Interfacial Assembly (FAIA) was utilized by introducing a polyethylene funnel, which facilitates the uniform and close-packed deposition of particle monolayers [145]. Briefly, the main concept of this approach relies on trapping nanobeads between two interfaces (water and air) followed by a compression of the particles to obtain a densely packed particle film. While the particle layer approaches the substrate, the plastic funnel due to the repulsion pulls beads closer together keeping the hexagonal packing. As a result, full coverage is obtained, which can be verified by a shimmering effect (Figure 4.1 a).

To fabricate nanohole arrays, different diameters of PS particle dispersions were utilized in the combination with interfacial assembly. PS beads with initial diameters of 198 nm, 382 nm, and 577 nm were utilized. The particle dispersion of 382 nm PS beads (5% in water) was mixed with ethanol containing 0.02% Triton-X 100 (TX-100) (Sigma Aldrich GmbH, Germany) resulting in an aqueous solution of 50% ethanol, 2.5% particles, and 0.01% TX-100. The same components with the aforementioned ratio were used for the preparation of 577 nm particle dispersion. Due to the smaller diameter, the colloidal solution of 197 nm PS beads was mixed in a higher concentration (10% in water) with the same components, resulting in the aqueous solution of 50% ethanol, 5% particles, and 0.01% TX-100.

Initially, a 4" quartz wafer (Plan Optik AG, Germany) was cleaned in the oxygen plasma at 0.7 mbar with 200 W power for 5 min and placed onto the sample stage within a funnel at a slight angle. The solution was then drop-casted on a glass slide that was partly immersed at approximately 30° into the water. Before drop-casting, the glass slide was cleaned in acetone and isopropanol followed by an oxygen plasma treatment with the same aforementioned parameters.

Upon contact with water, the particle solution spreads across the water-air interface leading to the formation of a packed layer. Ethanol enables a rapid spreading of the particle solution along the interface, while the surfactant TX-100 facilitates the transition to a packed monolayer avoiding significant voids and unordered domains [122]. In addition, a low surface charge of particles tends to keep the beads only partly submersed in the water medium enabling the reduction of repulsion and suitable balance between electrostatic and

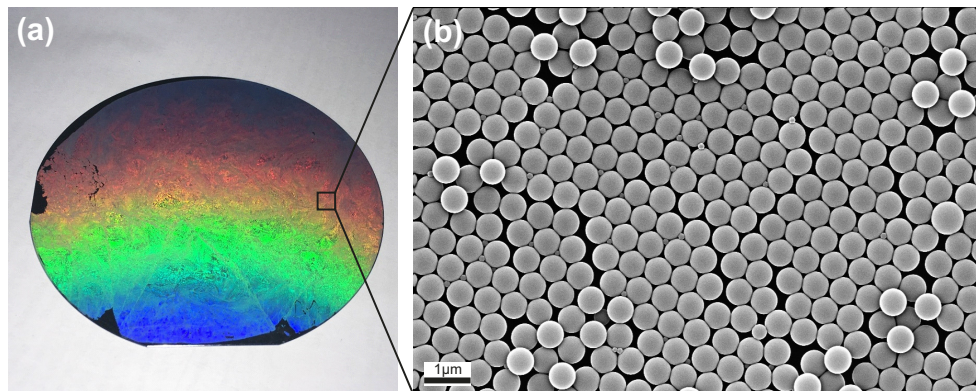


FIGURE 4.1: PS particles with a diameter of 577 nm deposited onto a SiOx substrate by means of FAIA. Photo (a) with corresponding SEM image (b), scale bar 1 μm .

capillary forces. The formation of the particle monolayer onto the water surface is followed by removing the water from the glass beaker. A highly hydrophobic plastic funnel surface creates energetically unfavorable conditions for the particles at the interface. Therefore, while the water level is reduced, the decrease of the water-air interface leads to a closed packing of the PS beads. Since the substrate is slightly tilted in comparison with the monolayer, it enables to avoid disturbances caused by particles and their agglomerations trapped between the substrate and the PS monolayer during deposition. The last step is drying, which is performed at the same angle as the substrate was placed onto the sample stage to prevent the formation of voids in the PS monolayer.

As a result, closed hexagonal layers of PS beads with diameters of 198, 382, and 577 nm (Figure 4.1 b, Figure 4.3 a, b) were obtained and prepared for the next steps of structuring.

Spin-coating

As an alternative technique to interfacial assembly, spin-coating was used for microbeads with a diameter of 1050 nm. In general, unlike interfacial assembly, spin-coating yields a lower quality of the long-range assembling. However, on the other hand, this approach enables to deposit PS beads in a fast, simple, and robust way (Figure 4.2).

Spin-coating was applied for small-sized quartz samples (16x28) mm^2 . Firstly, the samples were cleaned in oxygen plasma with the following parameters: pressure 0.7 mbar, power 200 W, and time 5 min. The initial concentration of the purchased particle dispersion (10% in water) was too low to support the assembling process during spin-coating. Therefore, the 1050 nm PS colloids (Bang Laboratories, USA) were centrifuged to obtain the 25% particle concentration in an aqueous solution. In the last step, the PS particle

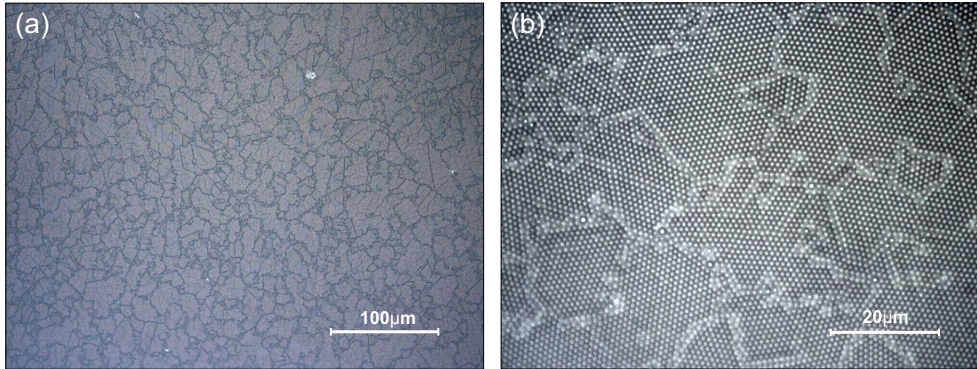


FIGURE 4.2: PS particles with a diameter of 1050 nm deposited onto quartz substrate by means of spin-coating at 8000 rpm for 2 min with 550 rpm/s acceleration. (a) scale bar of 100 μm , (b) scale bar of 20 μm .

dispersion was dropped onto the quartz samples and rested for 2 min to support the self-assembling, followed by spinning at 8000 rpm for 2 min with 550 rpm/s acceleration.

As expected, in the long-range the PS beads assembled with some disturbances in a particle monolayer (Figure 4.2 a). Mostly, the particles formed certain clusters with approximate size of $\sim 20 - 500 \mu\text{m}^2$, which were uniformly distributed with random orientation (Figure 4.2 b).

4.1.2 REDUCTION OF PARTICLES

Generally, the deposition of beads onto a substrate is the first step of nano-patterning followed by subsequent steps, e.g., dry etching [126], epitactic growth, and material deposition. Here, to fabricate nanohole arrays, colloids were utilized as a shadow mask for the final metallization.

As mentioned above, the main workflow consists of the following steps: PS particle deposition onto the substrate, reduction of the particles utilizing a dry etching technique, metallization, and particle lift off as depicted in Figure 4.3. In order to deposit particles, the two aforementioned techniques (section 4.1.1) FAIA and spin-coating were employed resulting in hexagonal monolayers of PS beads (Figure 4.3 a, b). To reduce the particle size, RIE was used employing the gas mixture of O_2 and CHF_3 [145]. Depending on the initial diameter of the PS beads and size of the substrate, different etching times were chosen keeping other parameters constant (see section A.1). Therefore, the etching time can be used as a varying parameter to control the resulting hole diameter of nanohole arrays (Figure 4.4).

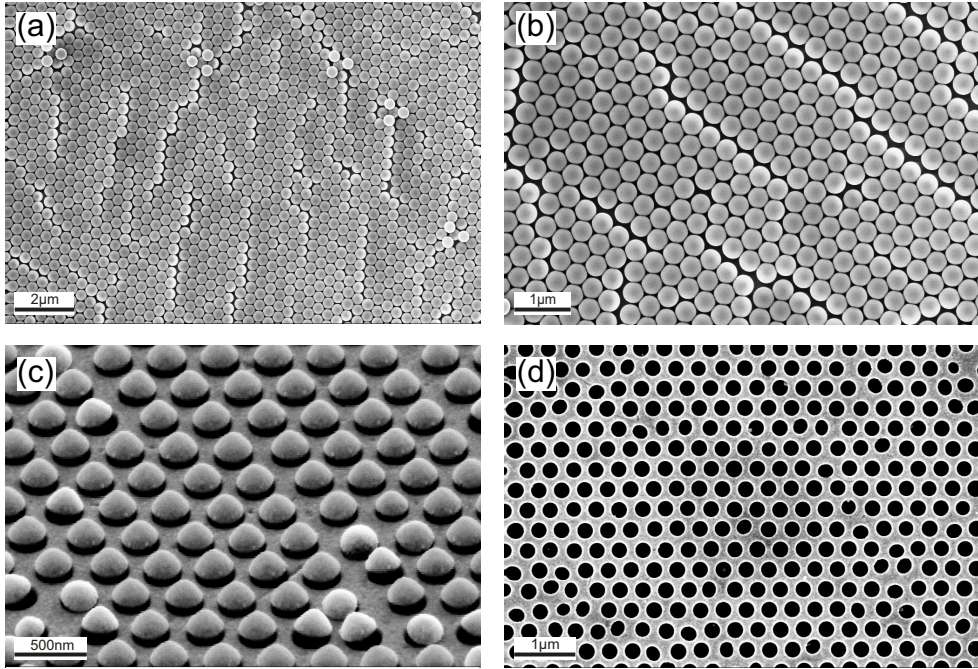


FIGURE 4.3: Workflow of nanohole array fabrication. Monolayer of PS particles with diameter of 382 nm (a) scale bar of $2\ \mu\text{m}$, (b) scale bar of $1\ \mu\text{m}$, (c) Reduced by RIE PS particles with evaporated metal layers of Ti 5 nm and Au 40 nm (SEM image is taken at 50°), (d) Nanohole arrays with a lattice constant of 372 nm and a hole diameter of 245 nm.

In order to find out the capability of the etching process, its quality, and the rate, PS beads of 382 nm diameter were transferred onto $10 \times 10\ \text{mm}^2$ size SiOx samples by utilizing the FAIA approach. The thin layer of chromium (30 nm) was deposited by e-beam evaporation followed by particle lift off by means of an adhesive tape. Noteworthy, the original diameter of PS bead size could be reduced by a maximum of 43% from $379 \pm 9\ \text{nm}$ to $216 \pm 6\ \text{nm}$. A longer etching process could destabilize the PS layer leading to the disruption in the assembled lattice and deprivation of spherical shape exhibiting randomly shaped elliptical holes. The etching process possesses a linear trend with a constant rate of 52.8 nm/min (Figure 4.5). Moreover, it was found that due to the specification of the RIE process, the etching rate decreases with increasing sample sizes. The etching rate of the same particle of 382 nm becomes slower for 4" wafers in comparison to the previously described $10 \times 10\ \text{mm}^2$ size samples and appears to be approximately 25.2 nm/min.

It is worth noticing that the thickness of the metal that can be deposited by this approach is limited by the diameter of the particles. During fabrication, it was empirically found that the diameter should be at least around 4 times larger than the thickness of the

4. Sample fabrication & characterization

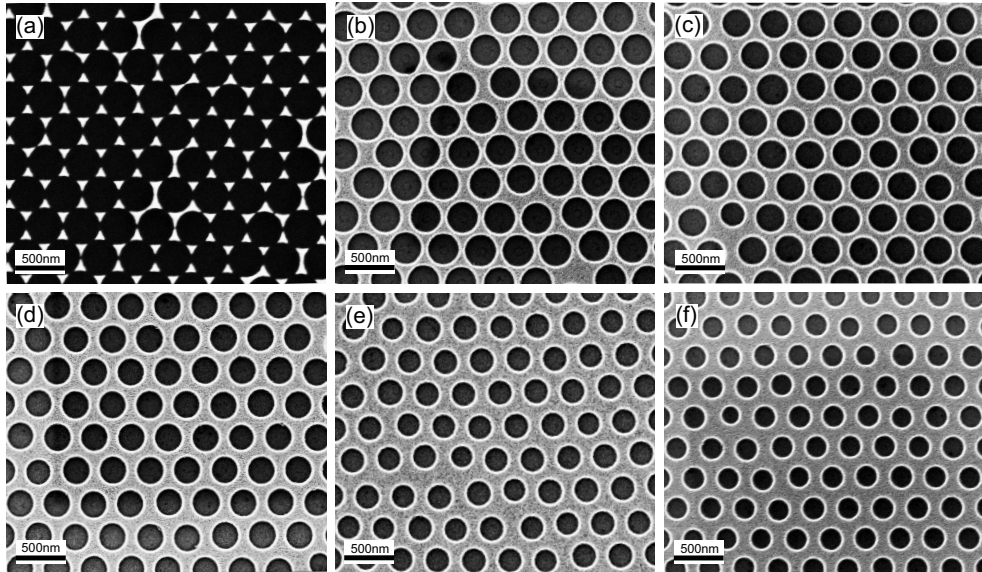


FIGURE 4.4: Nanohole arrays with a varying diameter of holes. The PS beads of an initial diameter of 382 nm were deposited by means of FAIA onto $10 \times 10 \text{ mm}^2$ sized SiO_x . The etching time of RIE and resulting hole diameter, respectively, are (a) 0 s, $381.8 \pm 8.6 \text{ nm}$, (b) 90 s, $303.9 \pm 5.2 \text{ nm}$, (c) 120 s, $280.5 \pm 4.7 \text{ nm}$, (d) 140 s, $264.8 \pm 6.3 \text{ nm}$, (e) 160 s, $240.4 \pm 5.2 \text{ nm}$, (f) 180 s, $216.1 \pm 6.3 \text{ nm}$.

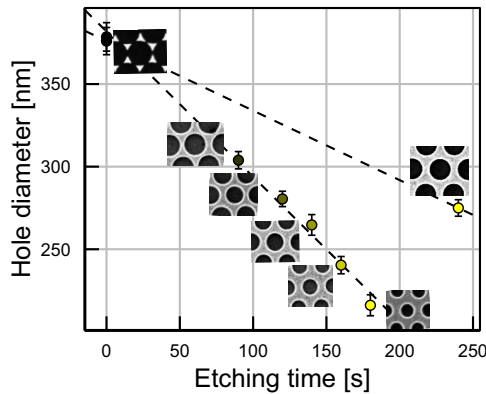


FIGURE 4.5: The hole diameter in nanohole arrays with the constant pitch of 376 nm (Figure 4.4) depending on the etching time utilizing RIE. The etching rate varies depending on the substrate dimensions appearing to be 52.8 nm/min for $10 \times 10 \text{ mm}^2$ surface and 25.2 nm/min for 4" wafer size substrates.

deposited metal. Thereby, in the subsequent metallization step to fabricate gold nanohole arrays on quartz substrates (Figure 4.3 d), two metal layers (5 nm Ti; 40 nm Au) were e-beam evaporated onto the sample decorated with the colloidal layer. The Ti plays a

role of an adhesion layer, while 40 nm of Au is thick enough in order to provide sufficient electrical conductivity and simultaneously support the SPP excitation (see section 5.2). Finally, the particles were stripped-off by means of an adhesive tape followed by sonication in acetone.

4.1.3 CHARACTERIZATION OF PARTICLE MONOLAYERS

The aforementioned way of nanofabrication introduced as NSL brings several advantages, in particular, the upscaling to wafer size with appropriate quality. However, monitoring the quality of the particle layer deposition remains challenging. Optical tools cannot be applied due to the diffraction limits, and techniques like AFM and SEM are time-consuming enabling to characterize only micro dimension areas, and, in case of SEM, require an additional conducting layer. Several approaches have been proposed including Fourier transform [126, 146], which allow checking the long-range quality of particle assemblies with high precision.

As an alternative, a more straightforward and simple approach can be applied using UV-vis-spectroscopy as introduced in [145], parts of which are described here. This method utilizes the radiative losses of photonic modes created by particle crystals into dielectric substrates. Besides enabling to monitor the quality of the colloidal monolayer during assembling, this technique allows one to track the size evolution of polymer beads during etching. This helps to precisely control the fabrication of nanohole arrays by NSL.

The extinction spectrum of PS particles deposited onto a glass substrate exhibits a distinct peak, which consists of two sub-peaks caused by the excitation of two photonic modes (Figure 4.6 a, black solid line). Noteworthy, the small dips, which appear at small wavelengths (< 380 nm) are associated with the Mie scattering of PS particles. In par-

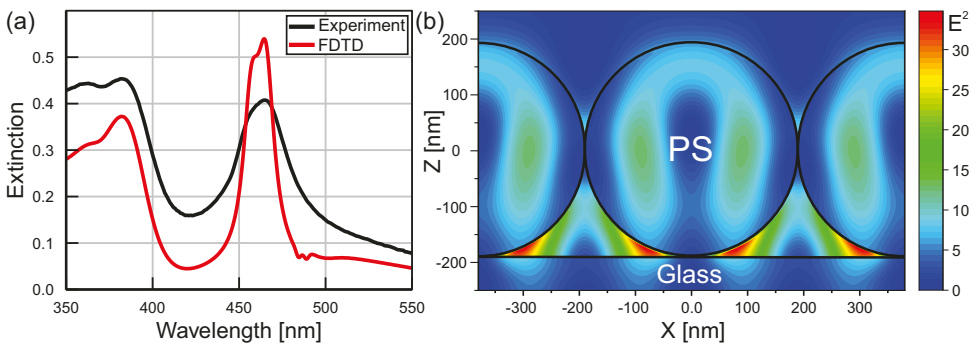


FIGURE 4.6: (a) Extinction spectra of a monolayer of PS particles of 380 nm diameter on a glass substrate, black - experimental data, red - FDTD simulation. (b) 2D electrical field distribution of 380 nm PS particles on glass, taken at the resonance wavelength.

4. Sample fabrication & characterization

ticalar, 380 nm PS beads assembled onto a glass surface reveal a peak at around 465 nm. To corroborate this experimental finding, the FDTD simulation was carried out. The working environment involves only two dielectrics introduced as glass substrate and PS particles with default refractive indices of 1.45 and 1.6, respectively. Thus, the transmission configuration of hexagonally assembled PS spheres of 380 nm diameter was simulated onto glass substrate. The obtained extinction spectrum (1-Transmission) reproduces well the experimental results (Figure 4.6 a, red solid line) revealing the main features of the spectrum.

Moreover, the 2D cross-section of the electrical field distribution obtained at the extinction resonance (Figure 4.6 b) reveals a confined intensity of the field associated with the first photonic modes [147]. The hexagonal layer of PS beads exhibits the highest values of intensity in the vicinity of the glass surface, which represents the coupling of the photonic modes into a dielectric substrate.

The reduction of the particle size during dry etching by oxygen plasma or RIE leads to a change of the effective refractive index of the particle monolayer (equation 4.1)

$$n_{eff}^2 = n_a^2 f_a + n_b^2 f_b \quad (4.1)$$

where n_a , n_b and f_a , f_b are refractive indexes and filling factors of materials a and b ,

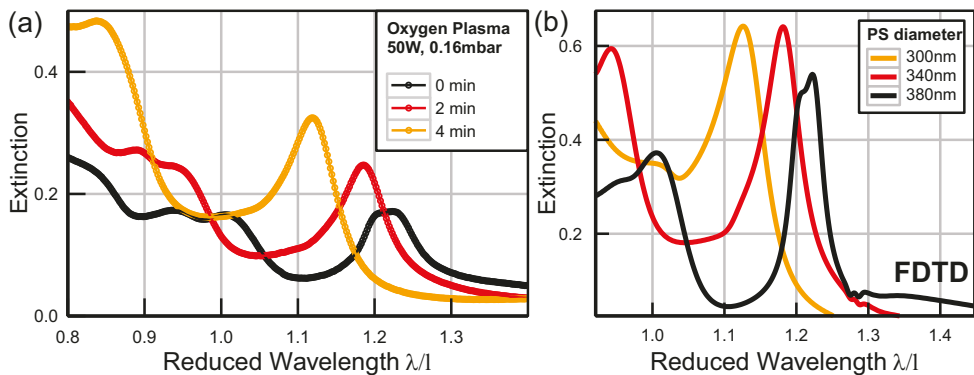


FIGURE 4.7: (a) Extinction spectra of a monolayer of PS particles of 520 nm diameter on glass showing a clear blue-shift of the extinction peak with increasing etching time in oxygen plasma. Figure is adapted from [145], (b) FDTD simulated extinction spectra of PS particles of diameters 380, 340, and 300 nm with a constant pitch of 380 nm on glass.

respectively.

This leads to the blue shift of the extinction resonance, while the diameter of the particles decreases (Figure 4.7 a). The experimentally obtained spectra were verified with FDTD simulation for 380 nm diameter PS particles (Figure 4.7 b). The obtained data

was plotted for experimental and simulated findings versus the reduced wavelength $\frac{\lambda}{l}$, where λ is a wavelength and l corresponds to the diameter of the particle. In this case, the extinction resonance appears at around 1.22λ . Noteworthy, the overall extinction increases, while the particle size reduces, which are corroborated by both experimental and simulated data. This general increase in extinction for shorter wavelengths is associated with increased Mie scattering efficiency of the PS beads.

4.2 BOTTOM ELECTRODE FABRICATION

The workflow of the crossbar fabrication realizing large-area molecular junctions in vertical geometry consists of several steps including the fabrication of bottom and top electrodes with the molecular diarylethene layer sandwiched in between. Thereby, it demands distinct requirements of both top and bottom layers of electrodes. To support surface plasmon-enhanced switching (see 5.3), the leads of the bottom electrode should be fabricated as gold nanohole arrays (nicknamed as "holey" hAu electrodes) on transparent quartz substrates maintaining a sufficient conductance, while the top electrode needs to complete the contact preventing possible formation of shortcuts and damaging of the molecular layer.

Therefore, two main strategies of bottom electrode fabrication were developed and tested to fulfill the aforementioned requirements. The first one involves the fabrication of nanohole array leads on quartz utilizing NSL [148]. In this approach, the leads were embedded in the substrate leveling out the surface to prevent a shortcut formation.

As an alternative, a second strategy was developed involving the fabrication of nanohole leads by utilizing an electron beam lithography to increase the quality of the nanohole arrays order. To avoid possible shortcut formation and current leakage, a thin layer (< 15 nm) of Ta_2O_5 was deposited to play the role of a passivation layer.

4.2.1 BOTTOM ELECTRODE FABRICATION BY NSL

Generally, the fabrication process follows a standard workflow with only one additional step of NSL. Thereby, it can be easily implemented for microelectrode fabrication where a plasmonic, transparent, and conductive material is demanded to enhance the functionality. For instance, microelectrode arrays (MEA) with nanohole array gold electrodes were developed to read out an electrical signal from biological cells as introduced in [149].

The fabrication workflow of the bottom electrode was carried out on 4" quartz wafers (Plan Optik AG, Germany) for implementing nanohole arrays and on 4" SiOx wafers for compact bottom electrodes as reference testing samples. The detailed fabrication protocol is described in section A.1 and Figure A.1. In order to provide a sharp undercut for the successive metal lift-off process, two layers of resists were employed. Firstly, a LOR3B resist was spin-coated followed by the deposition of the negative photoresist nLOF2020 resulting in a ~ 5 μm thickness double layer. In the subsequent step, the photoresist was exposed by a mask aligner with the dose of 55 mJ/cm^2 and 40 mJ/cm^2 UV light for quartz and SiOx, respectively. The bright field photomask was applied with the pattern depicted in Figure A.6. To define the designed structure composed of straight electrodes

by removing the unexposed areas, the photoresist was developed in MIF326 developer (Figure A.2).

To embed the leads, dry etching of the substrate material was applied utilizing RIE resulting in etched channels for metal wires. For this reason a combination of CHF_3 and Ar was employed.

As can be seen from figure 4.8 b, the etching process followed a linear trend revealing a constant etching rate of 12.9 nm/min. The depth of trench during the RIE process

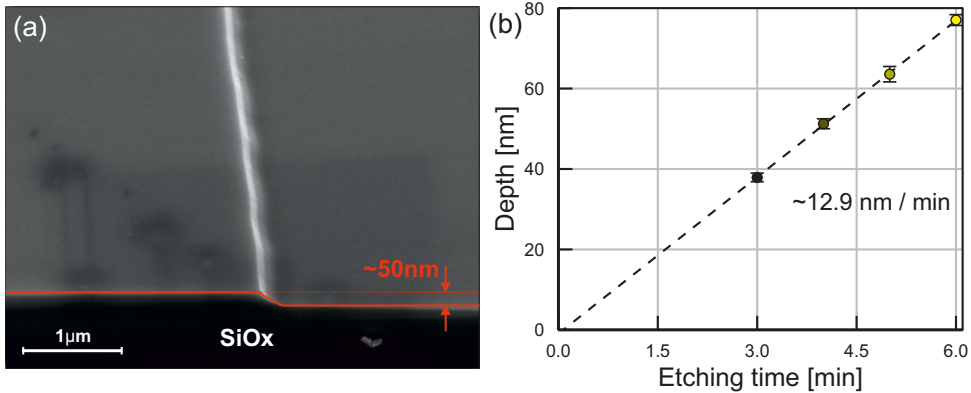


FIGURE 4.8: (a) SEM image of SiO_x etched by means of RIE to create trenches for embedding electrodes. The substrate was broken and the image was taken at 55°. The depth of the trench is approximately 50 nm, scale bar 1 μm. (b) The depth of the trench vs etching time dependence revealing an etching rate of 12.9 nm/min.

was measured by a surface profilometer (Dektak 150, Bruker Corporation, USA) after removing the small area of photoresist, which was designed in particular for this test (Figure A.6). Thus, to level out the bottom electrode surface by embedding the leads, a minimum time of 4 min was chosen. This gives approximately 50 nm of channel depth, which aims to precisely level out a 45 nm of metal consisting of 5 nm Ti and 40 nm Au (chapter 4.1).

Subsequently, the FAIA technique was employed following the steps described in details in section 4.1.1. Briefly, the quartz wafer with structured photoresist was cleaned in the oxygen plasma followed by placing it in the water medium onto the stage according to the FAIA protocol. During the particles' deposition, the wafer was tilted in the direction along the trenches in the central part of the chips to minimize disruptions of the layer and provide successive transfer inside the trenches of the photoresist. The PS bead deposition was followed by RIE to reduce the particles' size. As a result, the particle layer features local voids, which appear at the edges of the trenches, noteworthy, more frequently inside the narrower trenches in the resist (Figure 4.9).

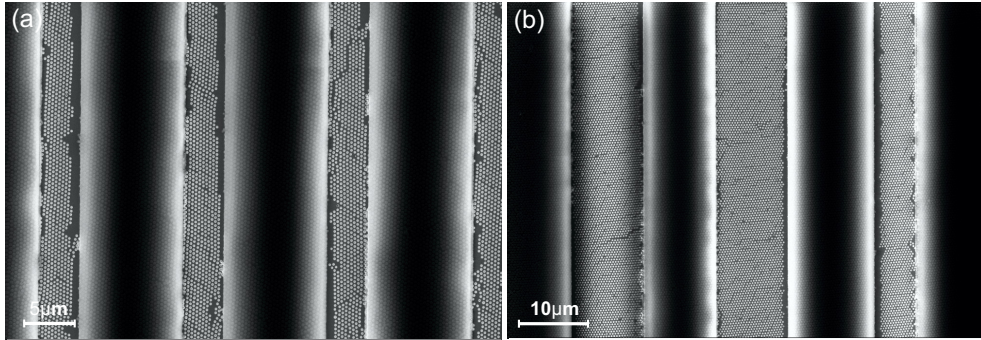


FIGURE 4.9: SEM image of structured photoresist with trenches of ~ 70 nm and assembled 382 nm PS beads etched by means of RIE for 4 min (a) scale bar 5 μm , (b) scale bar 10 μm .

In the subsequent step, two metal layers (Ti 5 nm and Au 40 nm) were e-beam evaporated (Leybold GmbH, Germany) onto the substrate. The resist lift-off was carried out in acetone followed by immersing in isopropanol and deionized water consecutively. The particles were removed by means of adhesive tape resulting in nanohole arrays implemented in the bottom electrode. (Figure 4.10). To remove the organic residuals of the resist, a RIE was employed utilizing O_2 gas.

In general, the nanoholes are distributed uniformly along the leads without major inhomogeneities. Several compact areas are observed, which are caused by disruptions in the PS layer. The nanohole arrays revealed a well-assembled hexagonal arrangement (Figure 4.10 c, d) showing a lattice constant of 373.6 ± 8.6 nm with a hole diameter of 265 ± 5.3 nm. However, residuals of the material appeared at the edges, which likely are either resist or evaporated gold. The metal deposition usually is carried out at a solid angle of approximately $\Omega \approx 7^\circ$. This deviation of the perpendicular deposition may lead to gold being evaporated not only within the trench in the substrate, but also on the edges.

According to the AFM images, the electrode is completely embedded into the substrate revealing a gap of around 30 nm with some residuals of resist and metal at the edges (Figure 4.11).

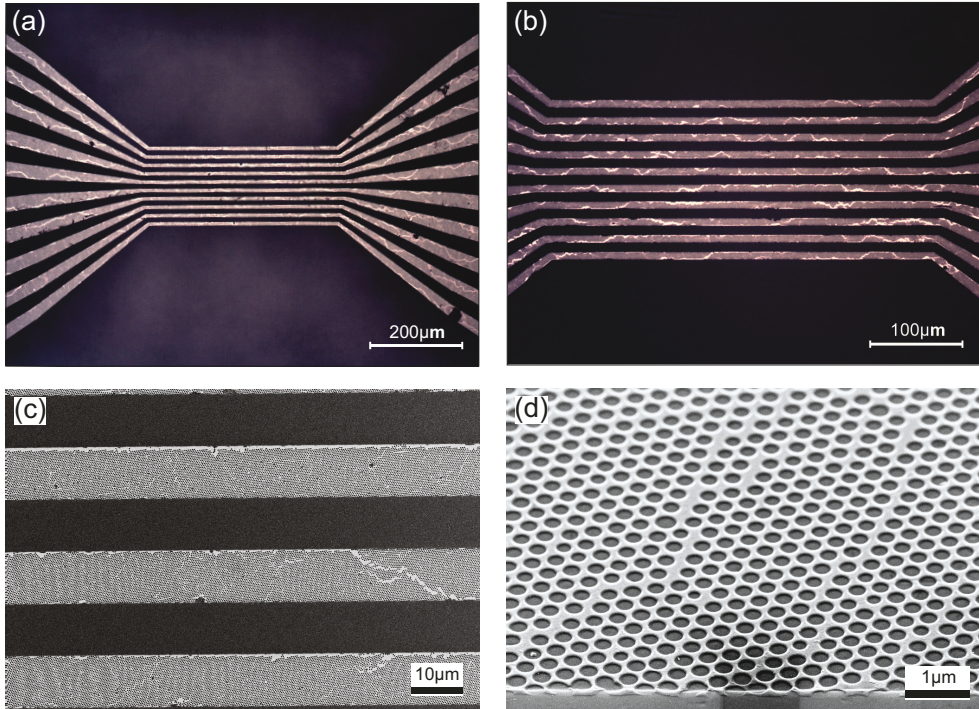


FIGURE 4.10: Optical images (a, b) of a bottom electrode with leads of $6 \mu\text{m}$ fabricated by means of combined photolithography and NSL. SEM images (c, d) of the $10 \mu\text{m}$ leads with lattice constant 373 nm and hole diameter 265 nm .

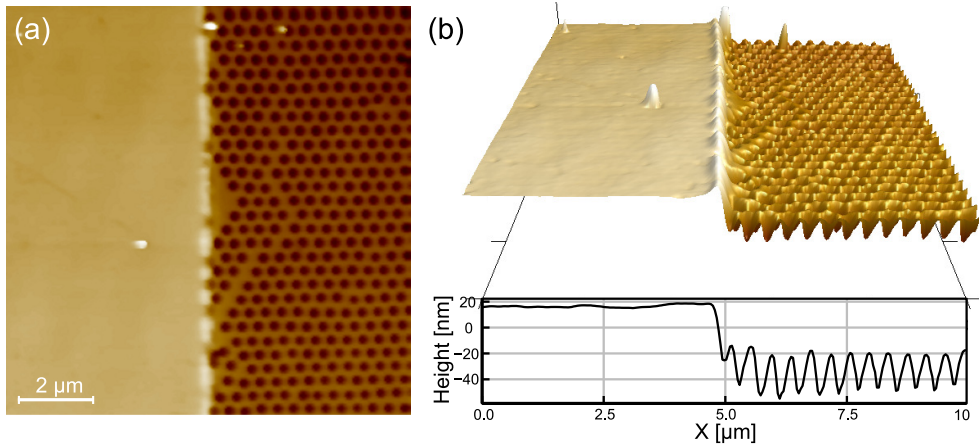


FIGURE 4.11: (a) AFM image of a bottom electrode with embedded hAu electrodes, scale bar $1 \mu\text{m}$. (b) The 3D AFM image with the height cross-section reveals the vertical level difference of around 35 nm between the quartz and the hAu electrode

4.2.2 ELECTRICAL CONDUCTIVITY OF NANOHOLE ARRAYS BOTTOM ELECTRODE

The process of perforating metal with holes reduces the area occupied with conductive material, which naturally tends to increase the overall resistance. Thereby, the question emerges what the degree of this reduction is and how it depends on the nanohole arrays' geometry. To obtain the resistance data, two approaches were applied involving simulation based on FEM and sheet resistance measurements of macro-sized samples. FEM simulation was carried out in collaboration with Z. Li and introduced in [150].

The simulation workspace of COMSOL Multiphysics involved a structure, which was designed as a plane with the following dimensions (length (L) = 50 μm , width (W) = 3 μm , and thickness 100 nm) and default gold conductivity model (electrical conductivity $4.56 \cdot 10^7$ S/m) [150]. The resistance R was obtained for two samples including 2D hexagonal lattices of 390 nm and 580 nm with varying hole diameter. Finally the sheet resistance $R_s = \frac{R \cdot W}{L}$ was plotted against the reduced diameter $\frac{d}{l}$, where d corresponds to the nanohole diameter and l being the lattice constant (Figure 4.12 a). As expected, while the nanohole diameter increases the sheet resistance rises dramatically following similar to hyperbolic trend reproducing the same behavior for both samples with lattices of 390 nm and 580 nm. As discussed in chapter 4.1, the nanohole arrays produced by NSL empirically exhibited a minimum ratio between hole diameter and lattice of 0.57. On

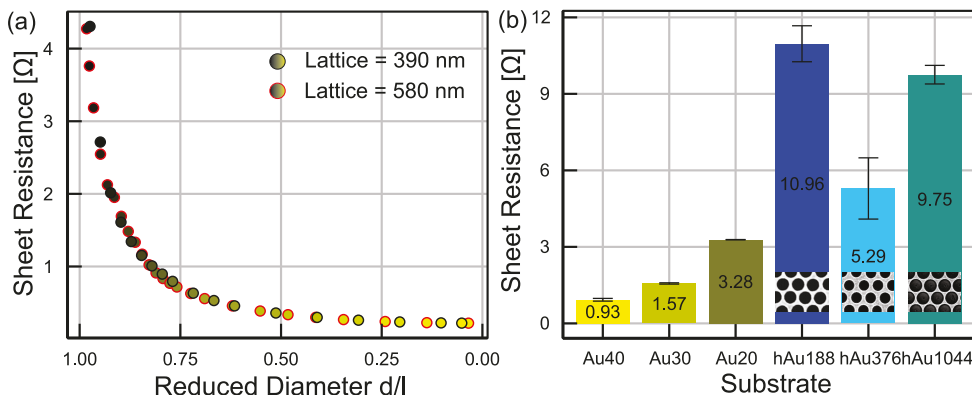


FIGURE 4.12: (a) Calculated sheet resistance R_s by COMSOL Multiphysics for the leads with width = 3 μm , length = 50 μm , and thickness = 100 nm plotted in accordance to hole diameter-lattice ratio (black - lattice 390 nm, red - lattice 580 nm); (b) The measured sheet resistance of compact Au with thickness of 40 nm (Au40), 30 nm (Au30), 20 nm (Au20), and hAu electrodes of lattice constants and hole diameters of 188 nm and 151 nm (hAu188), 376 nm and 275 nm (hAu376), and 1044 nm and 931 nm (hAu1044), respectively. The error bars were obtained as standard deviation of the mean.

average, the ratio varied between 0.6 and 0.9 meaning that according to FEM simulation the resistance for nanohole array electrodes in comparison with compact hole-free Au is expected to be increased by a factor in the range of [2 : 7].

The compact Au as expected revealed a higher conductance in comparison with hAu electrodes (Figure 4.12 b). Noteworthy, the sheet resistance increased dramatically, while the Au thickness reduced. The compact Au revealed values for 40 nm - 0.93 Ω , 30 nm - 1.57 Ω , and 20 nm - 3.28 Ω . At the same time, the nanohole arrays exhibited larger variations of sheet resistance varying from $\sim 5 \Omega$ to $\sim 11 \Omega$ depending on the ratio between hole diameter and lattice constant, and quality of hole arrangement. The larger values expectedly are observed for larger ratios: $11 \pm 0.7 \Omega$ and $9.8 \pm 0.36 \Omega$ for ratios of 0.8 ± 0.02 and 0.89 ± 0.02 , respectively.

4.2.3 BOTTOM ELECTRODE FABRICATION BY E-BEAM LITHOGRAPHY

As an alternative to bottom electrode fabrication using the NSL method, another approach that involves electron-beam lithography was chosen. Unlike NSL, the e-beam technique enables to overcome the diffraction limits of photolithography and expose resist with the resolution down to tenth of nanometers. Plus, an e-beam technique allows to define the nanohole arrays only in the central part where junctions are designed to be placed keeping the feedlines hole-free in order to conserve the overall conductivity of the gold leads.

The fabrication of the bottom electrode was carried out on the 4" quartz wafer. Firstly, to support sufficient grounding a layer of chromium (5 nm) was deposited onto a substrate followed by spin-coating a double layer of PMMA resists. The detailed workflow steps are described in section A.1. The double-layer resist was chosen to enable successive metal lift-off by providing a suitable undercut. The electron beam writing was carried out following the pattern depicted in figure A.7. Due to the different molecular weights of the selected resists, the lower layer exhibited higher sensitivity than the upper layer providing a sufficient undercut after development in AR600-55 (Allresist GmbH, Germany). This resulted in etched trenches reproducing the designed structure (Figure 4.13 a). The overall thickness of the double layer system was measured by employing the surface profilometer Dektak 150 revealing a thickness of 251 ± 4 nm.

The following step involved metalization of two layers of Ti 5 nm and Au 40 nm (Figure 4.13 b). The lift-off was done by megasonic cleaning in acetone followed by adhesive cello tape lift-off to remove minor metal residuals.

Atomic layer deposition of Ta₂O₅ was carried out to obtain the resulting thin passivation layer of 15 nm thickness. To open the layer, firstly AZ5214E resist was deposited onto the wafer and exposed by UV light through an optical mask (Figure A.8). The mask

4. Sample fabrication & characterization

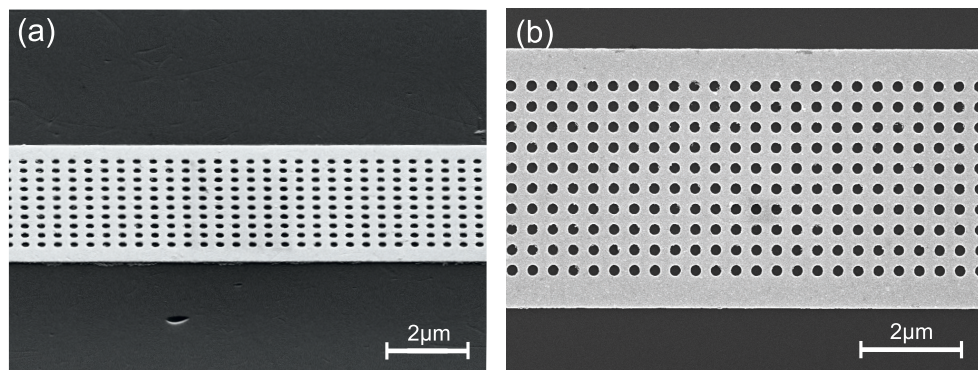


FIGURE 4.13: SEM images of 4 μm width gold nanohole array lead lift-off by acetone and adhesive cello tape.

was aligned based on the markers enabling to achieve less than one micron deviations in alignment. After development in MIF326, a layer of Ta₂O₅ was opened by RIE.

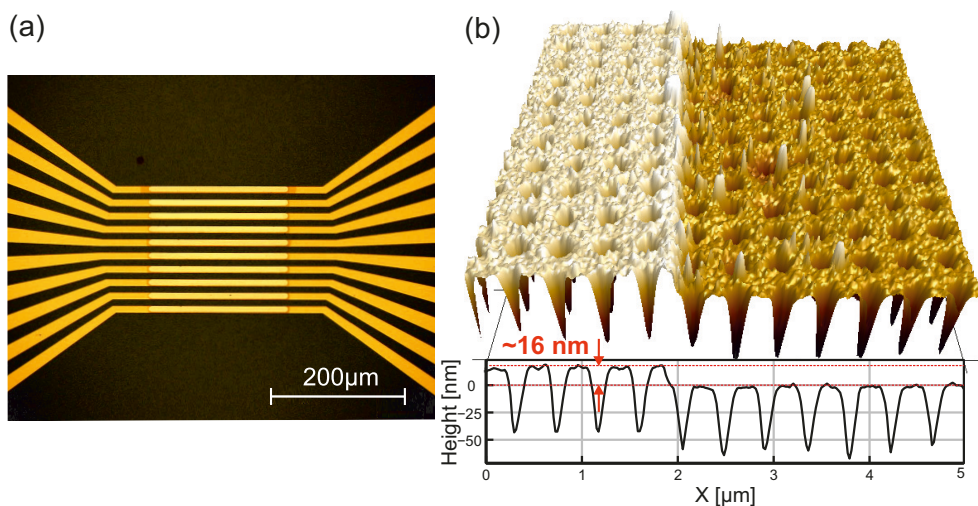


FIGURE 4.14: Bottom electrode fabricated by means of e-beam lithography with a passivation layer of Ta₂O₅. (a) Optical image of 10 μm wide leads with 8 μm wide openings, (b) AFM image showing a profile level gap of ~16 nm between Ta₂O₅ (light brown) and gold hole-patterned lead (dark brown).

The fabricated bottom electrode exhibits a profile level of ~16 nm created by Ta₂O₅ passivation layer (Figure 4.14), which can potentially be tuned to enable robust contact between molecules and top electrode.

4.3 TOP ELECTRODE FABRICATION

Molecular junctions with vertical geometry demand to fulfill certain requirements for the top electrode. The biggest challenge is to contact gold leads to the molecular layer providing a conformal contact to reduce the contact resistance and simultaneously prevent damage of the molecular species. For these reasons, in this work a top electrode is aimed to be fabricated on soft, flexible, and low stiffness substrates like PolyOlefin Plastomer (POP), which supports damage-free attachment. On the other hand, the roughness of the gold surface needs to be smaller than the dimensions of the molecular species to prevent shortcuts. Thereby, two approaches were tested. The first production workflow involves the fabrication of the leads on the solid substrate with an anti-adhesion layer to provide transfer onto the POP stamp. In this case, the roughness of the gold surface is defined by the roughness of the solid SiO_x, which is expected to be smoother than evaporated gold. The second workflow, on the other hand, is considered as being a straightforward and reference testing approach, where the gold leads are directly fabricated onto a polymer substrate. In this case, the roughness of the gold surface is higher, however, it still may be applicable to relatively thick organic films of >20 nm.

4.3.1 TOP ELECTRODE FABRICATION BY TRANSFER ONTO A POP STAMP

In general, the process combines classical photolithography techniques with chemical surface modification to provide a sufficient adhesion gradient for the successive electrode transfer. The detailed fabrication workflow is depicted in figure A.4 and described in details in A.1. The results were developed in collaboration with S. Tang and introduced in [151]. Briefly, the first step is the spin-coating of the negative resist nLOF 2020 onto a

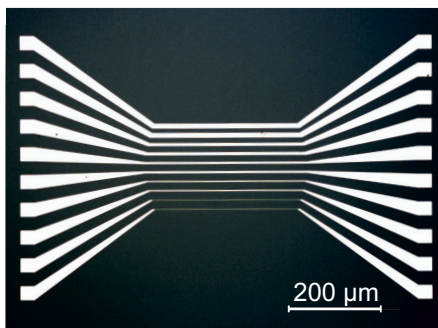


FIGURE 4.15: The "Gradient" top electrode (pairs of 2 μm, 4 μm, 6 μm, and 10 μm wide leads) on SiO_x with anti-adhesion layer of FOTCS in between.

4" SiO_x wafer, which was subsequently exposed with 40 mJ/cm² i-line (365 nm) UV light

4. Sample fabrication & characterization

and developed for 30 sec in MIF 326 in order to define the designed structure. To support the further surface modification by the perfluoro-silane FOTCS (Trichloro(1H,1H,2H-perfluorooctyl)silane, Sigma-Aldrich) the wafer was treated in oxygen plasma with the following parameters: pressure 1 mbar, power 80 W, time 5 min. A layer of FOTCS was deposited in a glove box via a gas phase deposition at 5 mbar for 90 min in a pure Ar atmosphere. In this case, not only a monolayer of silanes is covalently bound to the wafer, but also additional multilayers of physisorbed FOTCS molecules cover the surface. To increase the efficiency of physisorption, the time of deposition was extended to 90 min. In order to maximize the number of remaining silane molecules, immediately 40 nm of Au was e-beam evaporated at a high rate and low vacuum conditions. A low vacuum during metalization should maximize the chance of physisorbed FOTCS molecules remaining on the wafer. Subsequently, the lift-off of the photoresist was carried out in acetone followed by rinsing in isopropanol (Figure 4.15)

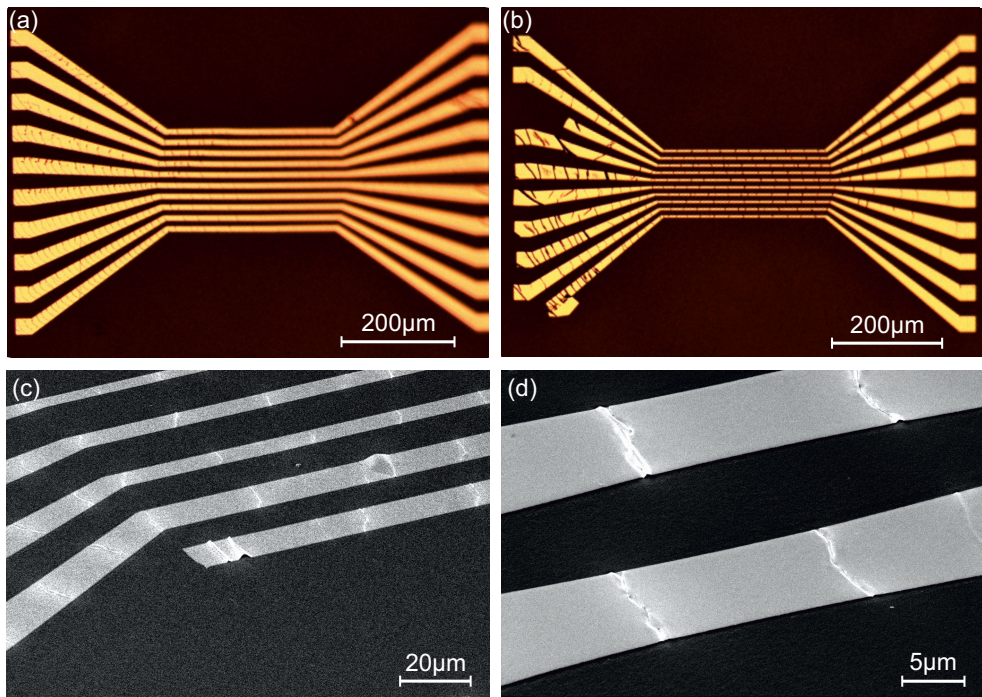


FIGURE 4.16: Optical image of a top electrode with (a) 10 μm wide leads transferred onto POP substrate, (b) 4 μm wide leads transferred onto a POP substrate, scale bar 200 μm . SEM image of a top electrode [151] with 10 μm wide leads taken at 45°, scale bar (c) 20 μm , (d) 5 μm . To image electrodes on the POP substrate, a thin layer of iridium (2 nm) was sputtered on the surface. The transferred gold leads exhibited wrinkles in the metal material, which appears as dimples and upheavals.

In the following step to make thin and smooth stamps, 0.5 mm thick pieces of Affinity POP stamps (Dow Corning, Midland, USA) were sandwiched between two previously silanized SiO_x wafers, heated up to 110 °C, and left for 30 min under pressure. The high smoothness of the stamp supports the successive conformal contact between wafer and stamp. Thereby, the gold wires can be quickly transferred onto the POP surface (Figure 4.16).

The yield of the successive transfer varies from batch to batch and, therefore, depends on the efficiency of the FOTCS deposition. The transfer was empirically found to be more efficient for leads with wider width, since in this case the silanized area is larger, which leads to a greater adhesion gradient. The areas with bad FOTCS deposition lead to a strong attachment of gold to the SiO_x wafer resulting in ruptured gold parts. Additionally, a mechanical mismatch between gold and the POP substrate leads to wrinkles in the metal surface (Figure 4.16 a, b). Plus, due to the bending, extra stress is applied that may contribute to the wrinkles' formation appearing to be a combination of dimples and upheavals (Figure 4.16 c, d), which reduce the overall conductance of the gold leads. However, the resistance of the molecule junction is still larger than the extra resistance caused by these dislocations, which makes such top electrodes suitable to complete molecule contact.

4.3.2 TOP ELECTRODE BY DIRECT FABRICATION ONTO POP

The fabrication of top electrodes by transferring them onto a polymer substrate possesses the biggest advantage of an ultra-smooth gold surface. However, the yield of fabrication is relatively low and highly depends on the fabrication factors. Additionally, due to the bending, the metal surface exhibits cracks and wrinkles, which may negatively affect the efficiency of the top-bottom electrode contact regarding mechanical and electrical properties.

To avoid the aforementioned issues, a straightforward fabrication approach was tested. The main concept consists of the direct fabrication of the gold leads onto 4" POP wafers. In this case, the smoothness of the gold surface is determined by the quality of the metal evaporation, however, the yield is expected to be high, revealing almost crack-free leads.

Firstly, the 4" POP substrate was prepared by pressing in a nanoimprint tool (Nanonex 2000, Germany) (detailed protocol is described in section A.1). The POP substrate was sandwiched between previously FOTCS modified 4" SiO_x wafers and pressed at $T = 90$ °C, pressure 60 psi (4.1369 bar) for 5 min. This results in thin and smooth POP substrates, which can be easily detached from SiO_x wafers due to the anti-adhesive layer of silanes. In the subsequent step, two metal layers of Ti 5 nm and Au 50 nm were evaporated onto the POP wafer followed by spin-coating AZ5214E positive resist at 4000 rpm for 60 sec

4. Sample fabrication & characterization

with an acceleration of 500 rpm/s. The soft-baking of the resist was carried out at a low temperature of 65 °C and a long processing time of 20 min to avoid extra expansion and bending of the POP substrate. Subsequently, the resist was exposed to 75 mJ/cm² of the i-line (365 nm) followed by a development in MIF326 for 50 sec. It resulted in the removal of the exposed area defining the designed structure.

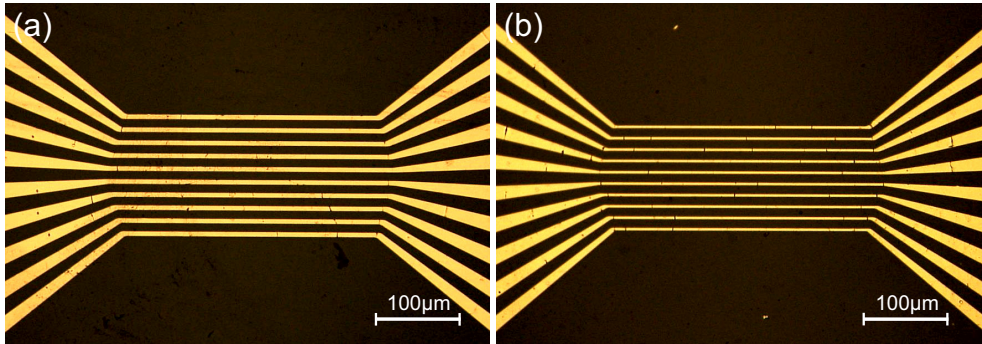


FIGURE 4.17: Optical image of top electrode fabricated directly on POP substrate with designed (a) 6 μm wide leads and (b) 4 μm wide leads.

In the subsequent step, the photoresist was used as a shadow mask for the etching of gold and titanium metal layers. Wet chemical etching was chosen to isotropically etch the metal minimizing possible damage of the POP substrate. Therefore, the wafer was immersed in TechniEtch AC12 (Microchem Corp, USA) for 1 min to remove the whole 50 nm layer of gold material followed by etching in TechniEtch TC (Microchem Corp, USA)

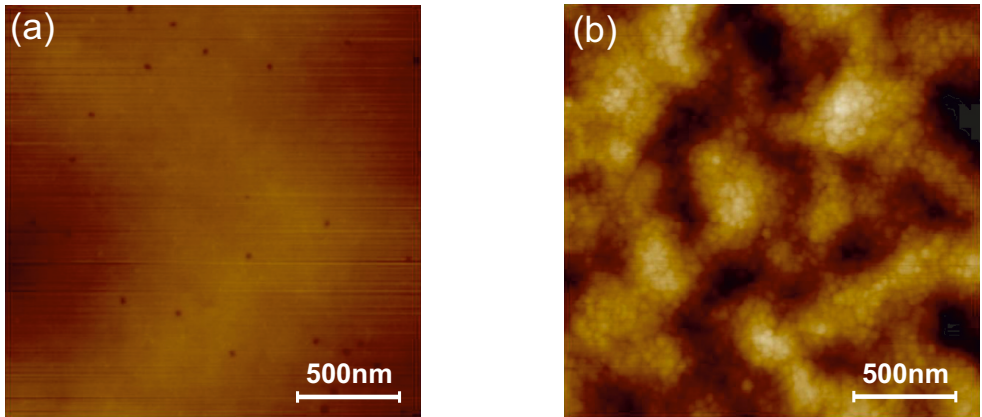


FIGURE 4.18: AFM images of the gold surface of the top electrode fabricated by (a) transfer onto a POP substrate, (b) direct fabrication onto a POP substrate. Images (a) and (b) were normalized to the same height level.

for 2-2.5 min to completely remove the residuals of underlying titanium.

According to optical images (Figure 4.17) the gold surface revealed wrinkles along the leads, which originated from the mechanical mismatch between the metal and the POP substrate.

Furthermore, to compare the surface roughness of top electrodes fabricated by the two scenarios, AFM imaging was carried out (Figure 4.18). As expected, the surface roughness of the transferred leads was smaller compared with directly fabricated on the substrate.

4.4 CROSSBARS ASSEMBLY

The process of assembly of the bottom and top electrodes into crossbars was carried out by employing a bonder Fineplacer (Finetech, Berlin, GER), which enables to align bottom and top layouts with precision of several μm . The working principle relies on

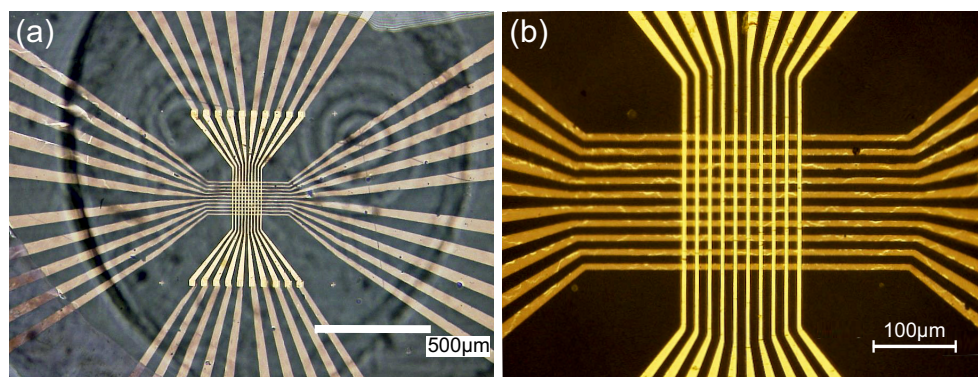


FIGURE 4.19: The optical images of assembled crossbars with the C_5FHSAc film sandwiched between nanohole array bottom electrode fabricated by NSL (width of the leads is $6 \mu\text{m}$) and top electrode on POP (width of the leads is $4 \mu\text{m}$). (a) scale bar $500 \mu\text{m}$, (b) scale bar $100 \mu\text{m}$.

the usage of beam-splitting optics, which allows simultaneous monitoring of the bottom substrate and another top layout held by a vacuum tweezer. Therefore, a top electrode can precisely be aligned and placed on the bottom electrode layout covered with a previously

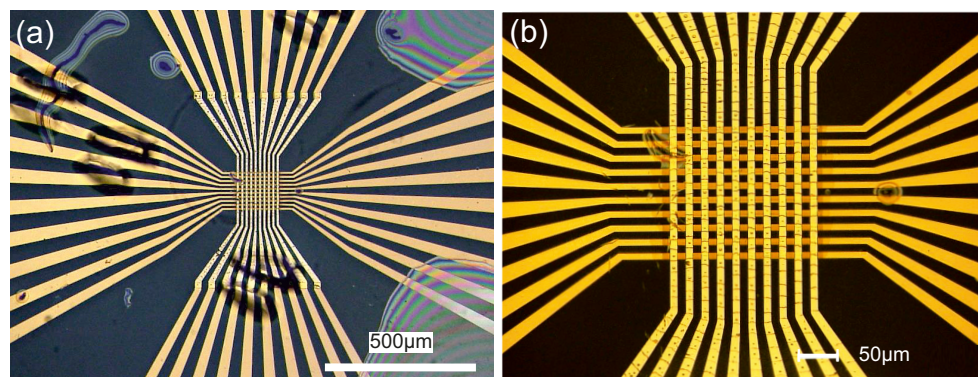


FIGURE 4.20: The optical images of assembled crossbars with the C_5FHSAc film sandwiched between nanohole array bottom electrode fabricated by electron-beam lithography (width of the top and bottom leads is $10 \mu\text{m}$). (a) scale bar $500 \mu\text{m}$, (b) scale bar $100 \mu\text{m}$. The conformal contact between the POP substrate and the bottom quartz surface can be distinguished by the darker color in the central part of the image compared to grey and slightly shimmering areas.

deposited C_5FHSAc film. Firstly the bottom electrode was chemically cleaned in acetone

and isopropanol followed by oxygen plasma treatment and gold oxide reduction in ethanol. Then the C_5FHSAc film was deposited onto the surface by spin-coating at 300 rpm for 90 sec. Then the top electrode was aligned accordingly to the bottom layout and placed onto the surface (Figure 4.19).

Due to the smooth POP surface and overall softness, a successive conformal contact can be achieved preventing air from being trapped in between. The contact can be optically distinguished by light contrast, which appears to be darker for conformal contact.

CHAPTER 5

RESULTS & DISCUSSION

5.1 CHARACTERISTIC OF DIARYLETHENES IN THE SOLID AND LIQUID STATE

There are different types of photochromic molecules including spiropyran, azobenzenes, fulgides, or diarylethenes. The latter ones exhibit thermal irreversibility and, more importantly, high fatigue resistance enabling several thousand reversible switching [7, 9], which all together make diarylethenes suitable for various applications e.g. optical memories, switches, and transistors. In this work, an approach for the transition of diarylethenes from the liquid to the solid state was developed together with the following characterization method.

The results described in this section are repeated in [106].

5.1.1 CHEMICAL & OPTICAL PROPERTIES

The diarylethene molecules used in this work are $C_{51}H_{30}F_6O_4S_2$ [152], abbreviation: C_5FHSAc . Generally, the chemical composition of the molecule can be divided into a central switching unit and two side chains (Figure 5.1, a). The switching core possesses double bonds, which can be reversibly isomerized due to the exposure to either visible or UV light. To prevent the coupling of the central unit to gold electrodes, the switching core exhibits furan groups instead of the commonly used thiophene groups. Moreover, the two conjugated side chains of the oligophenyleneethynylene are designed to feature high mechanical stiffness and relatively high conductance in both states. During the UV light-initiated photocyclization, the overall electronic structure alters from non-conjugation (open state) to end-to-end conjugation (closed state). The cycloreversion is initiated by

5. Results & Discussion

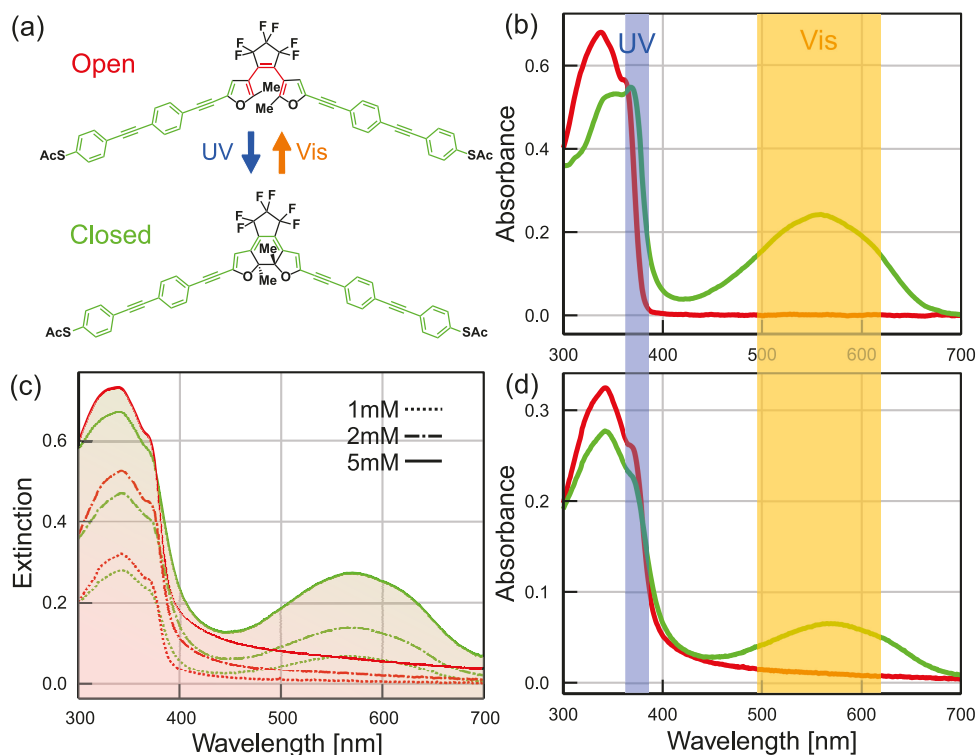


FIGURE 5.1: (a) Chemical structure of the C₅FHSAc molecule in open and closed configuration, (b) Absorption spectrum of C₅FHSAc molecules in closed (green) and (open) configuration dissolved in CHCl₃ with a concentration of 10 μM, (c) Extinction spectra of the molecule film in both forms closed (green) and open (red) on quartz substrate after spin-coating at 300 rpm for 90 s for different concentrations of C₅FHSAc in CHCl₃ (solid line – 5mM, dashed dotted line – 2mM, dotted line – 1mM), (d) Absorption spectrum of C₅FHSAc molecules spin-coated onto quartz substrate at 300 rpm from the initial concentration of 2mM resulting in ~18nm film thickness.

irradiation with visible light. These changes in the molecular geometry can be revealed optically by measuring UV-Vis absorption spectra. Usually, the transition between two states is carried out at the wavelength that corresponds to the maximum of absorption, since in this case the efficiency of switching is high.

To record an optical response, solid C₅FHSAc molecules were dissolved in CHCl₃ resulting in the 10 μM concentration. Closed molecules exhibited strong absorption in the visible and ultraviolet range while the open form absorbed only UV light, but more pronounced than the closed form (Figure 5.1 b). The obtained spectrum reproduced the main features of previously reported optical responses of the diarylethene molecules in the liquid form [62, 152].

5.1. Characteristic of diarylethenes in the solid and liquid state

There are various studies reporting on the investigation of diarylethenes in the liquid form [62], however, the transition to solid films brings several issues, especially related to the electrical measurements. Thereby, conductive matrices have been used e.g. P3HT [153]. Here, in order to investigate pure molecules' optical and electrical response, the straightforward approach of deposition such as spin-coating (see section 3.1.4) was chosen, avoiding interfering properties between diarylethenes and polymer matrices.

The film possesses a smooth morphology with a root mean square roughness of ~ 0.6 nm for a scan size of $4 \mu\text{m}^2$ (Figure 5.2). Only rarely local dimples of approximately 1-2

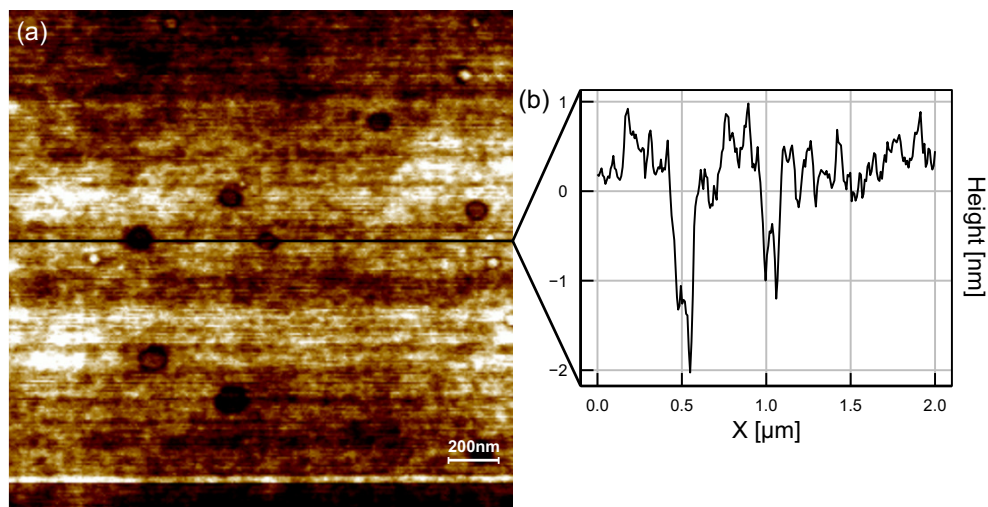


FIGURE 5.2: (a) AFM image of a C_5FHSAc film spin-coated on SiO_x with an oxide layer thickness of 100 nm. (b) Corresponding height cross-section along a horizontal line (black color).

nm are observed, which are likely caused by inhomogeneous evaporation of the volatile solvent. The film was capable to cover smooth surfaces homogeneously without cracks or other defects. During the deposition, the molecules are expected to adopt a haystack-like random orientation keeping the optical response similar to the one recorded in solution reproducing the main features of the corresponding absorption spectrum (Figure 5.1 b and d). Noteworthy, the isosbestic point (wavelength at which the total absorbance does not change during switching) was red shifted from 367 nm to 378 nm. The reproduced absorption features can be effectively used to transform molecules from the open to the closed state and vice versa. Therefore, light source 3.2 was employed fitting the visible absorption peak (Figure 5.1, orange range), while UV light irradiation (violet range) corresponds to the range near the isosbestic point.

5. Results & Discussion

Furthermore, the different initial concentrations of molecular species lead to a uniform change in the extinction spectrum (Figure 5.1 c). As expected with the increase of concentration, the molecular species form thicker films, which leads to stronger absorption properties. Noteworthy, all optical features including extinction peaks and isosbestic point remained unaltered along wavelength spectrum for all C_5FHSAc film thicknesses.

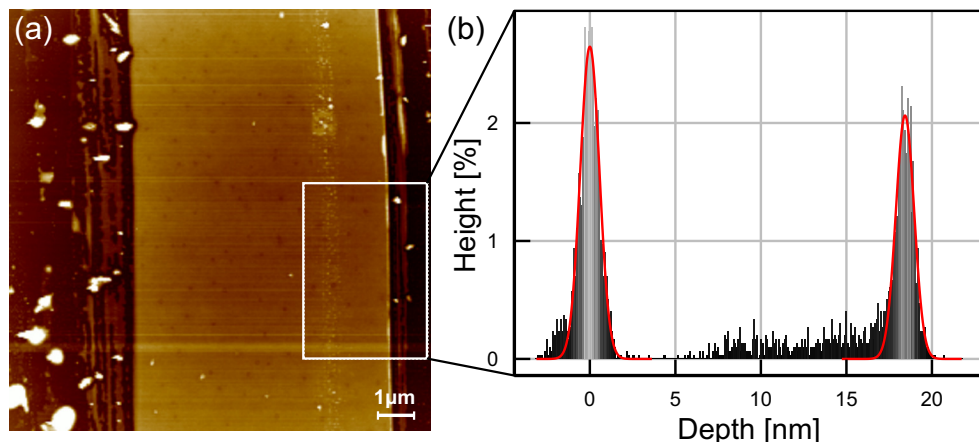


FIGURE 5.3: (a) AFM image of a C_5FHSAc film spin-coated and scratched on a SiO_x substrate with an oxide layer thickness of 100 nm. Bright brown color denotes the C_5FHSAc film, dark brown represents a SiO_x height level. (b) The depth distribution within the defined area (white frame).

In order to determine the thickness of the C_5FHSAc film deposited from 2 mM molecular solution, a scratch (Figure 5.3, dark brown areas) was made. The scratch was done with a soft PTFE tip in order to avoid damaging the substrate, which may have distorted the thickness measurements. A histogram shows two distinct peaks with 18 ± 0.8 nm relative height difference, which can be attributed to the molecular film thickness (Figure 5.3).

To perform the fatigue resistance measurements, the molecular film was switched from open to close states and vice versa to the saturation point by exposure to UV and visible light, respectively (Figure 5.1 c). The extinction at saturation degrades with the increasing number of switching cycles, which reproduces previously reported studies [7]. Noteworthy, the decay rate of the closed state degradation (UV initiated process) is larger (0.24) in comparison with the open state (0.016), which is initiated by visible light. Therefore, the UV-initiated process of closing degrades faster due to the dual absorption of UV light by open and closed molecules.

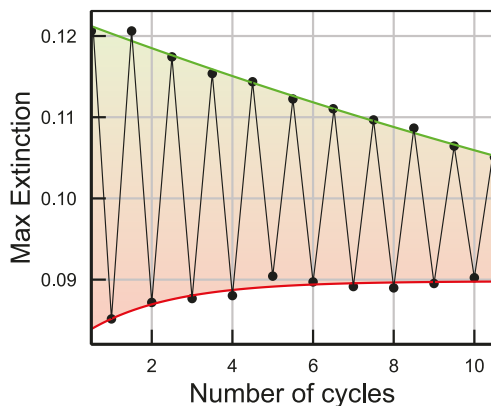


FIGURE 5.4: Fatigue resistance of the C_5FHSAc film measured as extinction at saturation vs number of switching cycles (green - closed state, red - open state),

5.1.2 REFRACTIVE INDEX ESTIMATION

One of the most common approaches to determine the refractive index (RI) of the material with a known thickness is using ellipsometry [154]. This method measures a change in polarization as a result of reflection and transmission of light from a material. Furthermore, it can be used to easily determine the film thickness of e.g. dielectrics, semiconductors, organics, and composites of materials.

However, the C_5FHSAc film investigated here exhibits absorption in both UV and visible range. This creates certain issues during an ellipsometry analysis. Firstly, the light used for the analysis may be absorbed during measurements, which affects the output results. Secondly, due to the sophisticated absorption spectrum, it is relatively difficult to find a proper model for the RI over the investigated wavelength range. A molecular film in the open state exhibits one absorption peak in UV, while closed molecules possess two peaks in both UV and vis range. The variation of the RI of these two states is the main focus of the further simulation (FDTD) analysis and, therefore, demands an accurate determination.

In order to overcome the aforementioned issues, the combination of the Lambert-Beer law together with the Kramers-Kronig relation [155] was chosen to determine the optical constants. On the one hand, the Lambert-Beer law enables to directly relate the absorption coefficient α to the absorbance (A) as follows $\alpha = \frac{A}{d}$, where d represents the thickness of the film (18 nm as shown in Figure 5.3). Therefore, an imaginary part of refractive

5. Results & Discussion

index, also known as extinction coefficient k , can be derived knowing both absorbance and thickness of the film according to the following equation 5.1 [155]

$$k(\lambda) = \frac{\alpha\lambda}{4\pi} = \frac{1}{4\pi} \frac{A\lambda}{d}. \quad (5.1)$$

On the other hand, the Kramers-Kronig relation allows to extract the real part of the refractive index $N=n+ik$ by utilizing the connection between real n and imaginary part k of RI (equation 5.2)

$$n(\omega) = 1 + P.V. \int_0^\infty \frac{\omega'k(\omega')}{\omega^2 - \omega'^2} d\omega'. \quad (5.2)$$

where ω is the angular frequency and $P.V.$ denotes the principal value of the improper integral. The limits of the integral are 0 and ∞ , which requires information on extinction coefficient over the wide frequency range. The measured frequency spectrum is usually truncated and limited by the scan range, therefore, the Kramers-Kronig relation can be applied to quantitatively estimate the real part of RI only. In this work, the discrete datapoints were measured on the interval $[\lambda_{\min}:\lambda_{\max}]$ with the wavelength step of $\Delta\lambda = 1$ nm. To facilitate the calculation, the dataset was converted to a frequency interval $[\omega_{\min}:\omega_{\max}]$ with a varying frequency step $\Delta\omega$. In order to avoid the singularity of the Kramers-Kronig integral, two meshes are introduced resulting in the following expression (equation 5.3) [156]

$$n(\omega)^{KK} = n_h + \frac{2}{\pi} \sum_{m=0}^{M-1} P.V. \int_{\omega'_m}^{\omega'_{m+1}} \frac{\omega'k(\omega')}{\omega^2 - \omega'^2} d\omega'. \quad (5.3)$$

where M denotes the number of datapoints and n_h is a constant, which compensates the truncation of the integral.

Taking the first-order approximation into account, where the imaginary part of the RI is considered to be a linear function over the frequency interval of $[\omega_m:\omega_{m+1}]$, the real and imaginary part of RI for both open and closed states of the C_5FHSAc film can be obtained (Figure 5.5). In order to determine the unknown constant n_h as well as to obtain the continuous dataset of the RI, the calculated datapoints were fitted with a multi-coefficient model in the Lumerical FDTD tool. The obtained parameters were chosen and used for the further FDTD results in this work to reproduce the experimental data with the highest possible accuracy.

Due to the direct correlation between the extinction coefficient and absorption (equation 5.1), in general, the imaginary part of the RI reproduces the absorption spectrum of the film (Figure 5.1 b) for both open and closed states (Figure 5.5, red dash-dotted line and green dash-dotted line, respectively). On the other hand, the calculated real part of

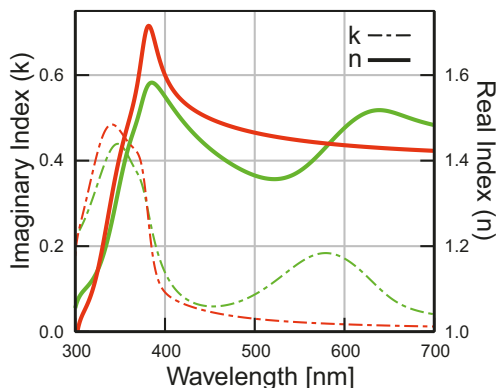


FIGURE 5.5: Calculated real (n) and imaginary (k) part of the refractive index ($N=n+ik$) for the C_5FHSAc film (red – open form, green – closed form, solid – real RI, dash-dotted – imaginary RI).

the RI reveals a resonance S-shape for the closed state in the visible range (Figure 5.5, green solid line), while there is no resonance for the open state (Figure 5.5, red solid line).

5.1.3 SWITCHING KINETICS

One of the most crucial characteristics of any switch is its kinetics. The kinetic parameters are well described and established for various photochromic systems. The switching kinetics is characterized by the energy required to convert the molecule from one stable form into the other. Generally, the photochromic molecules e. g. spiropyrans and diarylethenes are investigated in solution, and a first-order model is applied for the corresponding kinetics [10, 157]. The molecules in the liquid state show a good agreement with experimental data enabling the extraction of the main parameters like quantum yield ϕ and absorption coefficient σ . However, while the opening process fits well with the first-order kinetics, the description of the reversed closing reaction demands complex analytical analysis, due to the simultaneous absorption of UV light by open and closed molecules. Moreover, the conversion of molecules into the solid state brings in additional factors, in particular, local light beam distributions. Since the first reported kinetic model [158], there have been various attempts to develop the analytical solution for both opening and closing processes considering the aforementioned factors.

In this work, to facilitate the analysis of the kinetic parameters, the extinction was chosen. The extinction permits to take into account the change of transmitted light during exposure by external light. To characterize the switching kinetics, the molecular film was completely switched with the time steps, the obtained extinctions were subtracted from the extinction at saturation, and this difference was plotted versus the input light

5. Results & Discussion

exposure $H_e = I \cdot t$, where I - the intensity of input light measured as mW/cm^2 and t - time of exposure. Then the kinetic coefficient can be defined as a product of intensity I_a , quantum yield ϕ and absorption coefficient σ , which results in $k = I_a \cdot \phi \cdot \sigma$.

In order to determine the kinetic coefficients for the opening process, the spectra were recorded over the whole wavelength range of investigation with the illumination of visible light in between. The determination of the closing rate of the molecular film was performed by recording after UV illumination the extinction at a fixed wavelength corresponding to the maximum of the absorption in the visible range (see section 3.2). The procedure was repeated after each exposure to reach the saturation of extinction. The intensity of light during recording was much smaller than the one employed for switching, which prevented possible extra deviations in kinetic measurements.

Empirically it was found that the opening process follows well the first-order kinetics (equation 5.4), where the change of extinction is fitted by an exponential decay (Figure 5.6, orange datapoints). Here, ΔE stands for the change of extinction, ΔE_0 denotes the change of extinction at saturation.

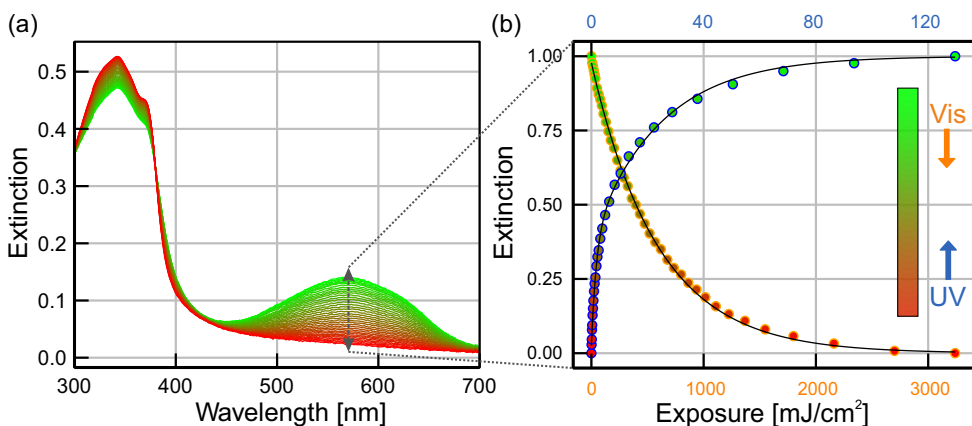


FIGURE 5.6: (a) Extinction spectrum of C_5FHSAC film on a quartz substrate during switching. (b) Kinetic characteristics of a C_5FHSAC film on quartz for the opening (orange) and closing (blue) process. The red to green color gradient indicates the degree of switching, where green denotes the closed form and red denotes the open form. Visible light (orange) converts the film from the closed to the open form (opening), while UV light (blue) triggers the reversed reaction (closing).

$$\Delta E = \Delta E_0 e^{-kH_e} \quad (5.4)$$

Unlike the opening, the reverse closing process follows a sum of two exponential functions where the first exponent determines the rate of initial switching (Figure 5.6, blue datapoints). The experimental data strongly deviate from a simple exponential decay as given in equation 5.4. However, the sum of two exponential decays (equation 5.5) shows

a suitable description of the kinetic rate of the closing process (Figure 5.7). The ratio between the two coefficients k_1 and k_2 is around one order of magnitude, which suggests two independent processes occurring with different rates. The faster one dominates in the

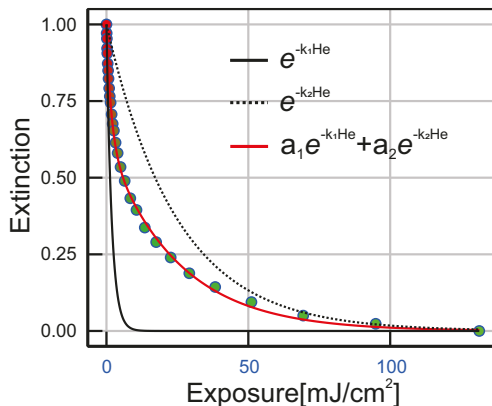


FIGURE 5.7: Kinetic closing trace for C_5FHSAc film spin-coated onto quartz substrate with the sum of two exponential decays fitting (red). Black curve denotes the exponential decay fitting with the coefficient k_1 , black dashed curve stands for the exponential decay with the coefficient k_2 .

beginning until approximately $\frac{1}{e}$ of the film is switched and the influence of the formed product can be neglected. This process is determined by the coefficient k_1 , which was chosen as a closing coefficient for all experimental data. The slower process dominates at the end of the switching, which may occur due to the additional absorption of light during closing, because of the absorption of UV light by both closed and open molecules. This residual closing can be described by the coefficient k_2 in the second exponential decay. To reduce its contribution the UV illumination was carried out at 379 nm (Figure 3.2), which corresponds to the isosbestic point of C_5FHSAc film.

$$\Delta E = \Delta E_{01} e^{-k_1 H_e} + \Delta E_{02} e^{-k_2 H_e} \quad (5.5)$$

By utilizing equations 5.4 and 5.5 the kinetic coefficients characterizing the opening and closing kinetics can be extracted. The C_5FHSAc film deposited onto quartz and illuminated from the top side reveals the coefficients of 0.011 ± 0.0008 and $0.046 \pm 0.010 \text{ s}^{-1}$ for opening and closing, respectively. The obtained values are in the same order as in a previously reported study for the C_5FHSAc film [148]. Furthermore, the overall dose required to completely open the film was determined to be $2.94 \pm 0.17 \text{ J/cm}^2$, while complete closing required only $0.125 \pm 0.009 \text{ J/cm}^2$, confirming the fact that the closing process occurs faster for the investigated C_5FHSAc film than the opening process.

5.2 OPTICAL PROPERTIES OF NANOHOLE ARRAYS

Depending on the application of nanohole arrays, their design and way of fabrication can be chosen based on several factors e.g. type of periodicity, lattice constant, thickness, material, etc. All these factors can be considered to modify the surface plasmon properties over the broad optical spectrum from the visible to the infrared (IR) range.

5.2.1 TUNING THE SURFACE PLASMON RESONANCES

As mentioned above, there are various approaches to fabricate nanohole arrays among which NSL is found as a versatile, fast, and wafer-scale method. The latter approach facilitates the manufacturing of nanoholes in a metal film arranged in hexagonally periodic arrays, where the lattice constant is defined by the initial size of the particles. Here, four

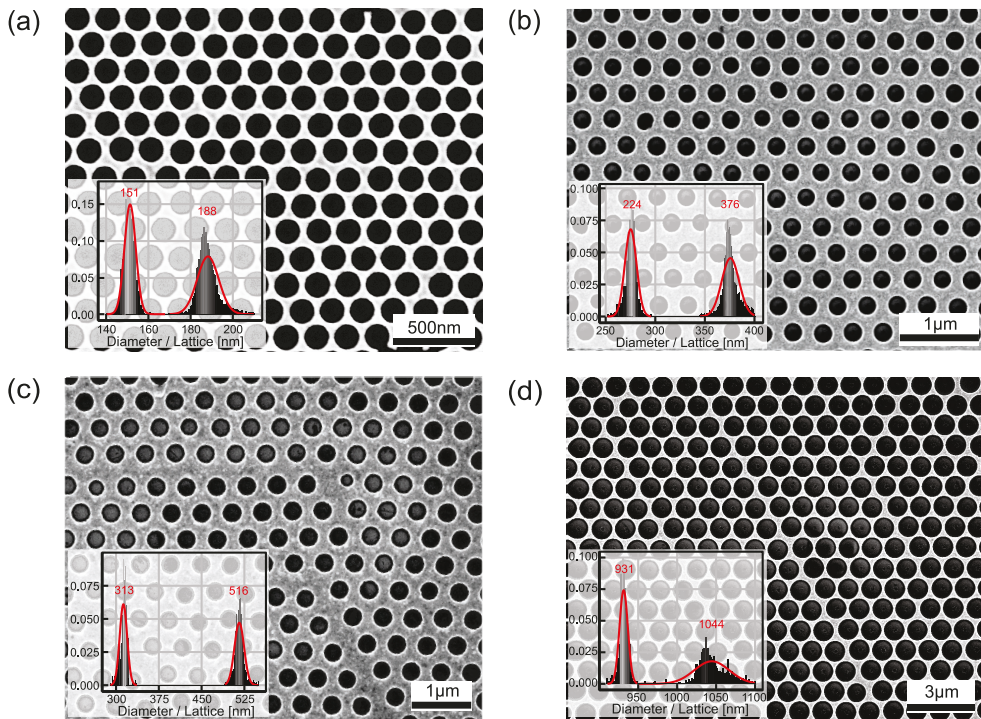


FIGURE 5.8: SEM images of hAu electrodes and corresponding distance histograms (insets) from which the lattice constants and hole diameters of (a) 188 ± 5 and 151 ± 3 nm, (b) 376 ± 12 and 224 ± 7 nm, (c) 516 ± 8 and 313 ± 7 nm, and (d) 1044 ± 22 and 931 ± 5 nm, respectively, can be determined.

types of nanohole arrays were fabricated by means of NSL utilizing different particles' diameters to obtain the SPP resonance in the broad optical window covering the visible

5.2. Optical properties of nanohole arrays

		Lattice constant [nm]			
		188	376	516	1044
SPP Resonance [nm]	Quartz (1,0)	500	570	700	1340
	Air (1,0)	390	480	520	917

TABLE 5.1: The position of Surface Plasmon Polariton (SPP) resonances calculated according to the equation 2.18 for hexagonal gold nanohole arrays with lattice constants of 188, 376, 516, and 1044 nm. The resonance wavelengths are determined for the first mode ($m=1$, $n=0$) and two interfaces such as quartz-gold and air-gold.

and near IR range. The PS beads with the initial diameters of 198, 382, 577, and 1050 nm were applied to fabricate hAu electrodes resulting in lattice constants of 188 ± 5 , 376 ± 12 , 516 ± 8 , and 1044 ± 22 nm, respectively (Figure 5.8).

In general, the assembly of nanoholes exhibits a uniform long-range arrangement with narrow distributions of lattices and hole diameters (Figure 5.8, insets). Noteworthy, the pitch distribution is larger for the hAu electrode fabricated by spin-coating (Figure 5.8 d). Due to the weak packing provided by the spin-coating, the interspace between PS beads cannot be strongly minimized like in the interfacial assembly, which leads to the larger deviations of the lattice constant value.

The equation 2.18, which defines the position of the SPP resonance, contains several parameters such as lattice constant, the dielectric permittivity of metal and substrate, and type of hole arrangement (e.g. hexagonal, square arrays). Most of the metals exhibit a negative real part of the dielectric permittivity (ϵ_m) in the visible range. In particular, gold reveals a negative permittivity, the value of which drops dramatically for the wavelength above 500 nm (Figure A.10, black line) [159]. Taking into account the wavelength dependence of the dielectric permittivity, the position of the SPP resonances can be determined as an intersection of two variables such as wavelengths at which resonances occur calculated according to equation 2.18 and the real part of the dielectric permittivity (Figure A.11).

The SPP resonances were calculated for nanohole arrays with the lattice constants of 188, 376, 516, and 1044 nm considering all aforementioned factors. Additionally, two interfaces, namely quartz-gold and air-gold, may contribute to the optical response affecting the resonance. The SPP resonance is expected to be located at approx. 500 nm for the nanohole arrays with the lattice constant of 188 nm (Table 5.1). This value corresponds to the first mode ($m = 1$, $n = 0$) and the interface gold-quartz, where the dielectric permittivity $\text{Re}(\epsilon_{\text{quartz}}) = 2.14$, while the gold-air interface gives resonance at approx. 390 nm. As expected, with the increase of the lattice constant, the SPP resonance shifts to higher wavelengths. The gold-quartz interface gives a resonance at around 570 nm for the

5. Results & Discussion

lattice constant of 376 nm, whereas the gold-air interface exhibits a resonance at approx. 480 nm. The red shift continues for the lattices of 516 and 1044 nm resulting in resonance wavelengths of 700 and 1340 nm, respectively.

The calculation (Table 5.1) predicts a variety of SPP resonances covering the broad range of visible and infrared wavelengths. In order to check the optical response of nanohole arrays, a transmission spectrum was recorded (Figure 5.9). The optical spectrum

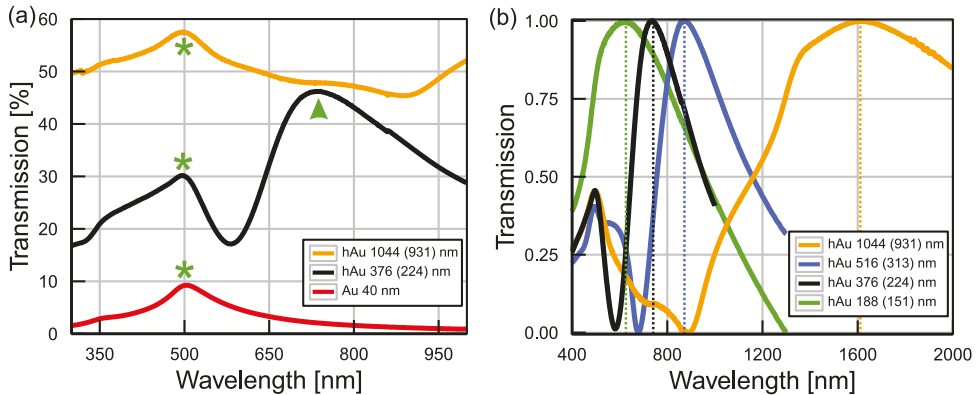


FIGURE 5.9: (a) Optical transmission spectra of hAu electrodes with lattice constants of 1044 (orange) and 376 nm (black) and compact Au of 40 nm thickness (red). The hole diameters are indicated in the brackets. Green asterisks mark a peak of Au self-luminescence that exists for both compact and hAu. The green arrowhead marks the SPP-induced transmission peak which is located at approx. 741 nm. (b) Normalized transmission spectrum of nanohole arrays with the lattice constants of 188, 376, 516, and 1044 nm.

of the hAu with lattice constant of 376 nm shows an increase of transparency compared to compact Au (Figure 5.9, red line) over the entire investigated spectral range with an enhanced transmission peak by approx. 45% positioned at 741 nm, which is associated with SPP excitations (Figure 5.9, black line). The compact Au with the same thickness exhibits only a peak at around 500 nm linked to the Au self-luminescence [160, 161] that is also observed for hAu electrodes. The nanohole arrays with the largest investigated lattice constant of 1044 nm do not show SPP-related peak in the visible range, but only the peak of Au self-luminescence. Noteworthy, the overall transmission of the latter electrode is higher across the investigated wavelengths range compared to the smaller lattice of 376 nm. This is expected due to the geometrical features of nanohole arrays, where, naturally, the metal film perforated with nanoholes leads to a continuous increase in transmission over all wavelengths. This can be seen as an increase in the peak of self-luminescence showing transmission of around 10%, 30%, and 57% for compact Au, hAu electrodes of 376 and 1044 nm, respectively.

The optical spectra of nanohole arrays show SPP resonances at 626, 741, 872, and 1611 nm for lattices of 188, 376, 516, and 1044 nm, which differ from values in table 5.1 revealing higher wavelengths than theoretically calculated. The possible reasons for this disagreement may be several factors that are neglected in the derived formula 2.18, such as hole diameter and metal thickness. The latter one plays a crucial role, especially for the optically thin metal (with a thickness in the same order of magnitude as the skin depth at the frequency of the light). In this case, the SPP modes at both interfaces (metal-dielectric and metal-air) overlap with each other inside the metal, which leads to a significant change in SPP resonance towards the measured value [162].

Furthermore, the SPP resonance reveals an asymmetric peak shape, which can be well-fitted with the Fano formula [163] (equation 5.6, Figure 5.10)

$$T(f) = T_0 + A^2 \frac{\left(q + \frac{2(f-f_0)}{\Delta f}\right)^2}{1 + \left(\frac{2(f-f_0)}{\Delta f}\right)^2} \quad (5.6)$$

where T_0 is a constant, A is the normalization constant, q denotes the Fano parameter, f_0 is the resonance frequency, Δf stands for the full width at half maximum. In this formula, the Fano parameter q is a measure for the asymmetry and is the key characteristic of the Fano theory. With the $q \rightarrow \pm\infty$, the formula 5.6 transforms to the classical Lorentz shape.

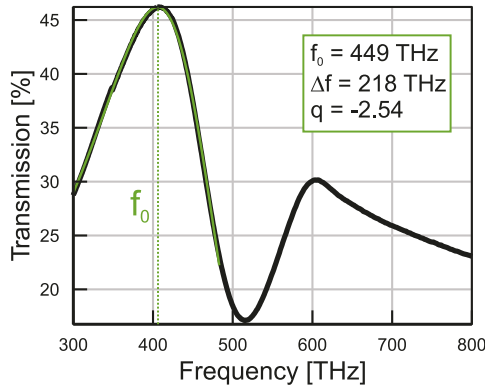


FIGURE 5.10: The transmission spectrum of nanohole arrays with the lattice constant of 376 nm and hole diameter of 224 nm plotted towards frequency range (black). The SPP resonance is fitted with the Fano formula 5.6 in the range of [300 : 480] THz (green).

As mentioned above, the formula 2.18 does not implement the contribution of factors such as e.g. metal thickness and hole diameter, which affect not only the position of the SPP resonance but also the entire transmission (Figure 5.11). To investigate the effect of the aforementioned parameters, the nanohole arrays of similar lattice constant of ~ 376 nm

5. Results & Discussion

were fabricated with the different hole diameters of ~ 224 and ~ 275 and metal thicknesses of 40 and 75 nm. As it can be seen, the entire transmission uniformly decreases with the increase of the hAu thickness, which is corroborated by FDTD simulations (Figure 5.11 a). While the thickness increases by almost the factor of 2, the transmission at the

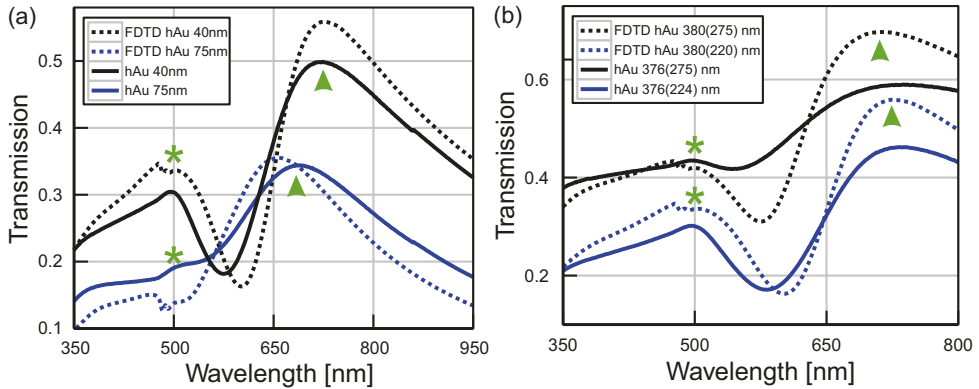


FIGURE 5.11: Experimental and FDTD simulated transmission spectra of nanohole arrays (a) with lattice constants and hole diameters of 376 ± 12 , 224 ± 7 nm and 377 ± 11 , 234 ± 7 nm and hAu thicknesses of 40 nm (black), and 75 nm (blue); (b) lattice constants of 376 ± 12 , 224 ± 7 nm and 376 ± 12 , 275 ± 5 nm. Green asterisks mark a peak of self-luminescence of Au, green arrows point stand for the corresponding SPP resonances.

SPP resonance decreases by around 15% from 50% to 35%. Additionally, the position of the SPP resonance blue shifts with the thickness increase, which can be explained by a weaker overlap between the plasmon modes at the gold-quartz and gold-air interfaces which results in smaller resonance damping.

In contrast, the increase of the hole diameter of hAu electrodes leads to a uniform increase of the entire transmission due to geometrical features. In this case, the metal openings are larger, thereby, transmitting more light. Additionally, the SPP peak appears to become broader, which can be related to the damping of the SPP lifetime. With the increase of the hole size, the free metal area where plasmons are able to exist shrinks, leading to a shorter mean free path. Additionally, the position of the SPP resonance slightly differs, which is likely to be a result of the aforementioned phenomena.

The equation 2.18 that defines the position of the SPP resonances predicts the direct dependence on the incident angle of the incoming light. Thus, to test this, optical transmission spectra were recorded with the change of the angle between light and nanohole arrays surface (Figure 5.12). The hAu electrode with the lattice constant of 376 nm and hole diameter of 224 nm showed a zero-order transmission peak at around 737 nm and a magnitude of approx. 48%. With the increase of the incident angle from 0° to 32° , the SPP resonance was red shifted from 737 nm to 818 nm. Noteworthy, the peak of

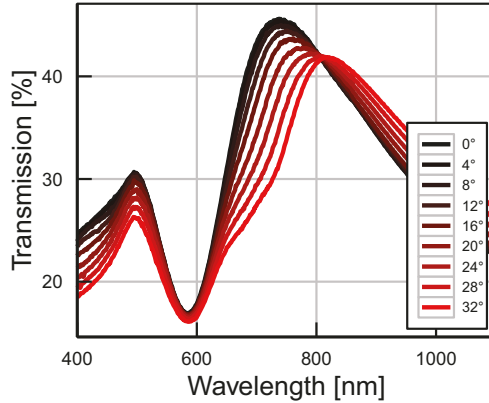


FIGURE 5.12: Transmission spectrum of nanohole arrays of lattice constant $d = 376 \pm 12$ and hole diameter 224 ± 7.44 nm depending on the angle of incident light. The color gradient (black - red) corresponds to the increase of the angle from $\theta = 0^\circ$ to $\theta = 32^\circ$.

the Au self-luminescence and the dip at around 580 nm remained unaltered, which additionally verifies the surface plasmon-related nature of the transmission peak at 737 nm. Furthermore, the entire transmission gradually drops by approx. 5% uniformly over the investigated wavelength range, which originates from light reflection. While the angle increases more, light is reflected and less reaches the detector.

5.2.2 ENHANCED TRANSMISSION BY WAVEGUIDE MODES

The optical response of nanohole arrays, as shown in the previous section, depends on several factors like e.g. lattice and dielectric constant. So far, the transmission spectra were obtained for samples surrounded by air without additional impacts on the main SPP peak that originates from the gold-quartz interface. However, for various applications such as biosensing and imaging, the nanohole arrays may be surrounded by a material with certain dielectric properties. For instance, the nanohole arrays interact with an aqueous medium enhancing transmission as was firstly introduced in [149], parts of which are repeated below.

To test the optical properties of the hybrid structure: metal nanohole arrays - medium, the hAu electrode with the lattice constant of 376 ± 12 nm and hole diameter of 224 ± 7 nm was chosen (Figure 5.8 b). As shown above, in the air this hAu electrode exhibited SPP originated transmission peak of $\sim 45\%$ at around 726 nm, which was verified with FDTD simulation (Figure 5.13 a, black). Water-based media exhibit a refractive index of 1.33 and do not absorb light in the wavelength window from ~ 500 to ~ 900 nm facilitating the optical measurements [15]. Therefore, the nanohole arrays were placed in an

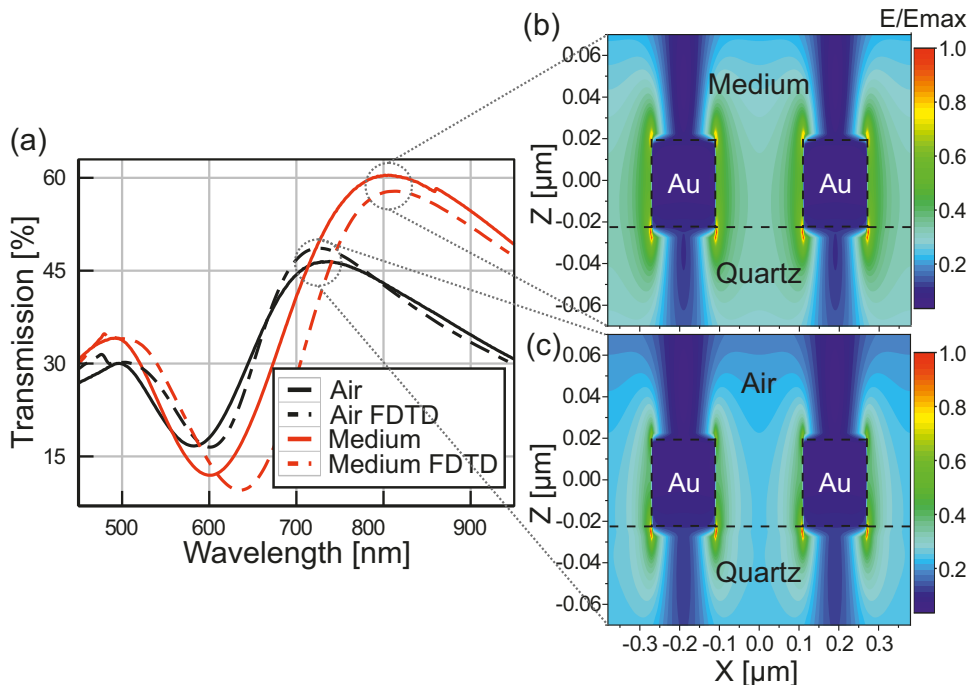


FIGURE 5.13: (a) Transmission spectra of hAu electrode with the lattice constant of 376 ± 12 and hole diameter of 224 ± 7 nm in the air (black solid line) and medium (red solid line). Dashed lines represent the FDTD simulated spectrum in the air (black) and medium (red). FDTD simulated electric field distribution in the x - z cross-section of the hAu electrode in (b) aqueous medium (RI=1.33) and (c) air captured at the wavelength of transmission peak.

aqueous medium and no reference sample was used during spectra recording. Bringing such a dielectric in the close vicinity of nanohole arrays surface leads to a red shift of the resonance, as predicted by formula 2.18. The peak shifts towards higher wavelengths by around 60 nm. Moreover, the entire transmission of the SPP induced peak increases, which could not be predicted by theoretical calculation. Furthermore, the FDTD simulation reproduces the main features of the spectra verifying the enhanced transmission by around 15% after adding the medium. Noteworthy, the peak of Au self-luminescence remained almost unaltered unlike a transmission dip, which red shifted in a similar manner as the main SPP peak.

The FDTD simulation enables to capture the electrical field distribution through nanohole arrays along the x - z plane (Figure 3.5, 5.13 b, c). If the electrical field is plotted for the hAu electrode located in the air, the field at the maximum of transmission is localized near the edges of hAu at the Au-quartz interface dropping to the center of the nanohole (Figure 5.13 c). In contrast, when cell medium is added, the electrical

field is concentrated near the edges of the hAu surface, gradually spanning inside the nanohole (Figure 5.13 c). Furthermore, when the two x - z distributions are compared, the overall electrical field magnitude is higher throughout the nanohole for hAu electrodes in medium, which leads to higher transmission. This effect originates from the edges of the nanohole cavity, which suggests that an additional component contributes to the overall electrical field intensity and, consequently, to the transmission. As discussed in chapter 2.2, the surface plasmon excitation via nanohole arrays is the result of several processes one of which is the photonic modes induced via holes. This leads to the hypothesis that nanohole walls create a Fabry-Perot resonator, which matches the resonance frequency of the SPP, thereby, enhancing the overall intensity of the electrical field inside the nanohole. This also explains, why the phenomenon becomes less pronounced when the medium is removed from only the nanohole area and when the dielectric constant of the medium exhibits smaller values.

Furthermore, the electrical field seems to cover more area above the hAu electrode surface in the medium compared to the same nanohole arrays in air. If the value of the electrical field is plotted versus vertical coordinate z , it reveals an exponential decay exhibiting the decay length of ~ 27.5 nm (Figure 5.14). There is a small deviation of

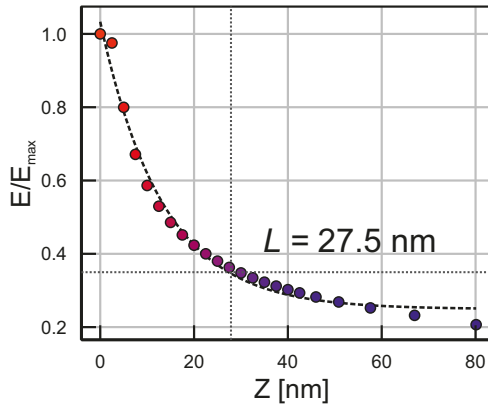


FIGURE 5.14: The decay of electrical field magnitude towards z axis starting from the top edge of hAu electrode surface located in an aqueous medium. The datapoints are fitted with exponential decay giving a decay length of 27.5 nm.

datapoints from the exponential trend over the plotted range, in particular, for $z > 60$ nm, which can be explained by inaccuracies of simulation that highly depends on the e.g. mesh settings. Depending on the applications, the decay length can be tuned mostly by the lattice constant and by other parameters such as the metal thickness and the hole diameter.

5.3 SURFACE PLASMON-ENHANCED SWITCHING KINETICS

The surface plasmon excitation via nanohole arrays has been extensively utilized in various fields e.g. for sensors, in spectroscopy, microscopy, and photovoltaics due to the SPP-related enhancement of the electrical field at the close vicinity to the surface.

The nanohole arrays utilized in this work not only can increase the rate of photoreaction by utilizing the surface plasmon enhanced electrical field but also can be employed as conductive electrodes to support the electrical transport within a molecular junction. The results described below were firstly introduced in [106].

5.3.1 MORPHOLOGY OF THE C_5 FHSAC FILM ON NANO HOLE ARRAYS

The first question that emerges is how well the molecular film can be deposited onto such a complicated topography like nanohole arrays. The set metal thickness of the nanohole arrays was around 40 nm (Figure 5.8), while the film covers smoothly the flat surface with the thickness of around 18 nm (section 5.1.1). Due to the wetting properties, the film may penetrate inside the holes spanning the whole space within the hole.

To deposit the C_5 FHSAC film onto the hAu electrodes, the same procedure was applied as for the smooth surface (section 3.1.4). Three nanohole array electrodes with lattice constants of 188 nm, 376 nm, and 1044 nm were tested (Figure 5.8).

Before spin-coating, the hAu electrodes exhibited vertical topographic features of around 40 nm peak-to-peak height as expected from the metal film thickness (Figure 5.15 b). After

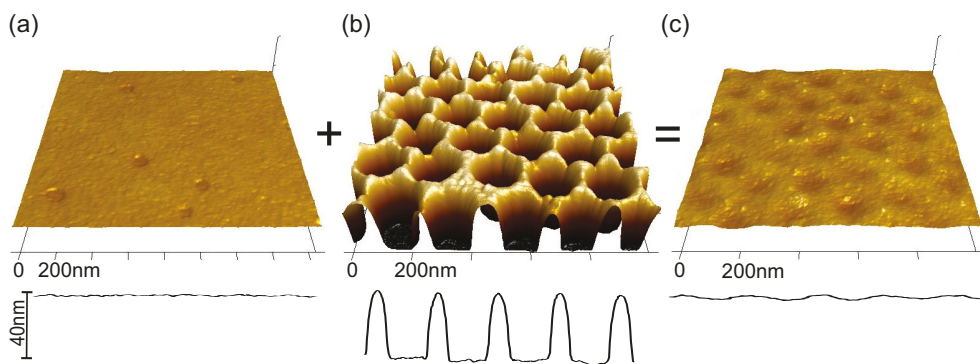


FIGURE 5.15: A C_5 FHSAC film on nanohole arrays with the lattice constant of 188 ± 5 nm. (a) AFM measured surface topography of the C_5 FHSAC film on the SiOx substrate. (b) AFM measured surface topography of bare nanohole arrays with 188 nm lattice and 45 nm metal thickness (Au 40 nm and Ti 5 nm). (c) Surface topography of the C_5 FHSAC film on the 188 nm lattice nanohole arrays.

spin-coating, the nanohole arrays were covered with a smooth molecular film leveling-out

the corrugations of the underlying electrodes. According to AFM measurements of hAu electrodes with a hexagonal lattice constant of 188 ± 5 nm, the variations in topography decreased to less than 3 nm (Figure 5.15 c).

For other tested nanohole arrays (376 nm and 1044 nm lattice constants), the spin-coated film covered the nanohole arrays homogeneously without defects following the morphology of the hAu electrode (Figure 5.16). The C_5FHSAc film did not level out

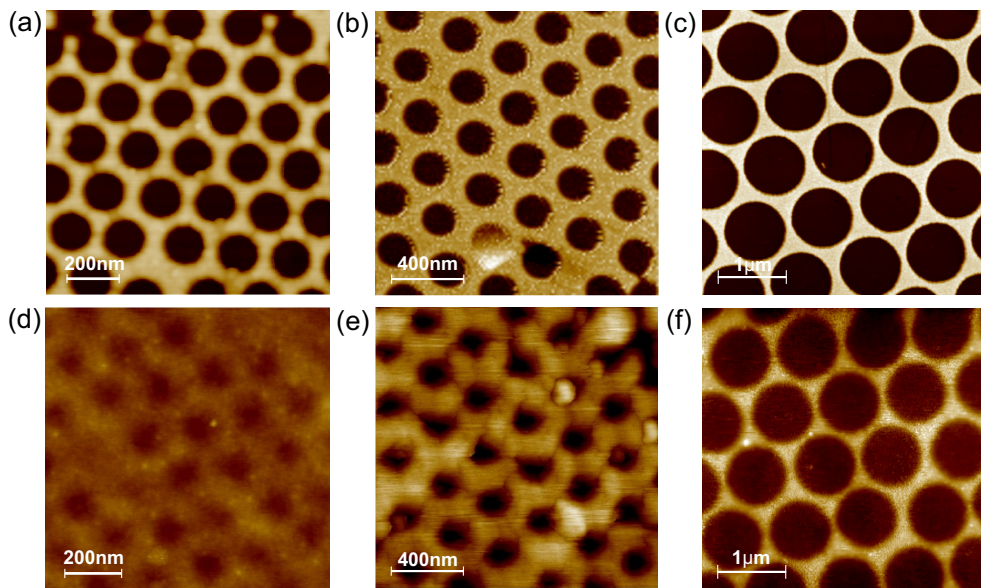


FIGURE 5.16: Top row: AFM images of bare nanohole arrays with the lattice constant of (a) 188 nm, (b) 376nm, and (c) 1044 nm. Bottom row: AFM images of nanohole arrays with spin-coated C_5FHSAc film on lattice constants (d) 188 nm, (e) 376nm, and (f) 1044 nm, revealing a variation of topography less than 3 nm, 14 nm, and 13 nm, respectively. Bottom row images are normalized to the same height scale. Scale bars (a), (d) - 200 nm, (b), (e) - 400 nm, and (c), (f) - 1 μ m.

completely the corrugations of the underlying hAu electrodes revealing variations of the topography of less than 14 nm for the 376 nm lattice (Figure 5.16 e) and less than 13 nm for the 1044 nm lattice constant (Figure 5.16 f). To clarify the height difference, the AFM images were normalized to the same height scale (Figure 5.16, bottom row). The small variations of the color level indicate that differences in topography are small for 188 nm lattice in comparison with other nanohole arrays. As it can be seen, while the lattice constant increases, the variations of the topography rise as well. If 376 nm and 1044 nm nanohole arrays are compared, considering the hole diameter and lattice constant, the filling factor is lower for the 1044 nm than for the 376 nm lattice. Thus, the C_5FHSAc

film covers the 1044 nm lattice hAu electrode with the constant thickness of around 25 nm inside the holes and shows additional coverage spikes of 13 nm height at the hole edges.

5.3.2 OPTICAL RESPONSE OF THE C₅FHSAC FILM ON NANO HOLE ARRAYS

As it was shown in chapter 5.2, the SPP excitation conditions depend on several factors as e.g. lattice constant, incident angle, dielectric permittivities of the metal, and the dielectric at the surface (section 5.2). Thereby, the variation of any of these parameters leads to a direct change in the SPP excitation.

The C₅FHSAC film exhibits a decent refractive index spectrum for both real and imaginary parts (Figure 5.5). While the imaginary part follows the absorption spectrum due to the absorption properties of the film, the real part exhibits more complex dependence revealing an S-shape curvature at the absorption resonance. In the visible range, the value of the RI varies from around 1.35 to 1.5, which, thereby, can lead to the red shift of the SPP resonance (Figure 5.17 a, b).

As discussed in section 5.2, the nanohole arrays show an increase in transmission over the entire investigated spectral range compared with compact Au of the same thickness (Figure 5.17, black curves). The compact Au reveals one decent peak around 500 nm (Figure 5.17, d), whereas the optical spectra of the hAu with lattice constants of 188 and 376 nm showed enhanced transmission peaks positioned at around 600 and 720 nm, respectively.

The AFM measurements (Figure 5.16) revealed that the film fully spans the space inside the nanohole forming a meniscus and covering the hAu surface completely. This means that within the penetration length of the SPP, the refractive index increased leading to a red shift of the transmission peak by around 80 nm (Figure 5.16 a, b, red and green curves). Moreover, since the film is trapped within the nanoholes, the formed Fabry-Perot resonator waveguides the light leading to the enhanced transmission by around 7% corroborated by FDTD simulation (Figure A.12). The transmission spectra of the open (red) and closed (green) C₅FHSAC film deposited on nanohole arrays can be unambiguously distinguished from the compact Au by the absorption in the UV and visible range, which features pronounced similarities to the spectra of the same film on quartz (Figure 5.1). Noteworthy, the position of the absorption peak in the UV range remained unaltered for all hAu electrodes, which indicates that there is no plasmon-matter interaction in this spectral region.

The C₅FHSAC film can also clearly be switched on compact Au (Figure 5.16 d) showing optical spectra superimposed with the self-luminescence peak of the Au. Similar features were observed and FDTD simulated for the Au with smaller thicknesses of 20 and 10

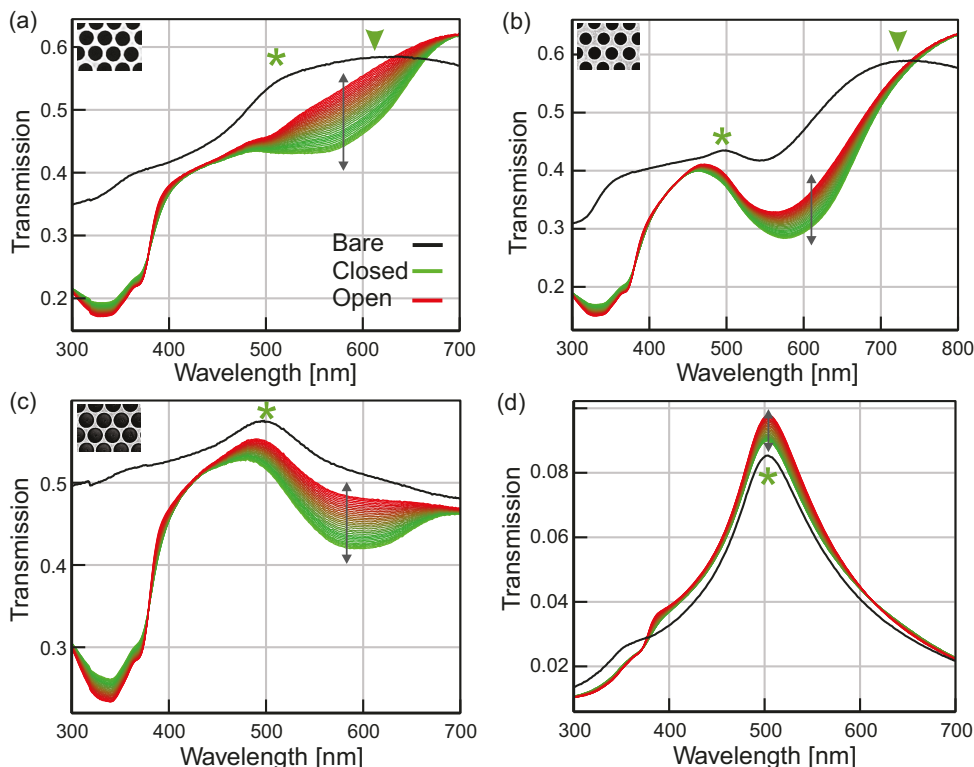


FIGURE 5.17: Optical response of the C_5FHSAc film on compact Au and nanohole arrays. Transmission spectra of C_5FHSAc film on (a) nanohole arrays with a lattice of 188 nm, (b) 376 nm, (c) 1044 nm, and (d) compact Au of 40 nm thickness (black, bare electrode; red, open film on the hAu electrode; green, closed film on the hAu electrode). Green asterisks mark the peak of the Au self-luminescence that exists for both compact Au and hAu. The green arrowhead marks the SPP-induced transmission peak of the hAu. The gray double-headed arrow marks the maximum change of absorption, where the kinetic characteristics are recorded.

nm (Figure A.13). The bands associated with the molecular film gradually rise and the Au features disappear with decreasing Au thickness. Noteworthy, the transmission considerably increased for hybrid structures of compact Au- C_5FHSAc for all samples. The experimentally recorded and FDTD simulated spectra corroborate that an increase occurs for wavelengths larger than ~ 380 nm. The effect may be explained by waveguided light within the film trapped between two different media.

None of the aforementioned features is observed for the hAu electrodes with the largest lattice constant of 1044 nm. This nanohole arrays- C_5FHSAc structure does not exhibit SPP-related optical features but instead shows a drop in transmission superimposing the main features of the pure molecular spectrum on quartz within the UV-vis wavelength range.

5.3.3 SWITCHING KINETICS OF THE C₅FHSAC FILM ON NANO HOLE ARRAYS

As described in section 5.1.3, the opening and closing processes follow different trends of kinetics. While the opening reaction can be fitted with the first-order kinetics (equation 5.4), the opposite closing process empirically follows the formula consisting of a sum of two exponents (equation 5.5). Based on the obtained spectra the C₅FHSAC film can be reversibly switched through different substrates like Au, nanohole arrays (hAu electrodes), and almost fully transparent quartz (Figure 5.17).

In order to investigate the kinetics on different substrates and evaluate the contribution of SPPs on the switching processes, two scenarios were tested. The first one was introduced as the C₅FHSAC film, which is positioned behind the substrate forming a transmission structure (light source - substrate - C₅FHSAC film). Thereby, the light has to pass through the substrate material to reach the film, which reduces the light intensity at the film and is expected to affect the switching rate. In contrast, the second scenario involves the switching from the frontside, where a C₅FHSAC film is sandwiched between a light source and the substrate forming the configuration (light source - C₅FHSAC film - substrate). In this scenario, the reduction of the transmitted light intensity due to the filtering by the substrate is disregarded, highlighting only the interaction between light at the substrate surface and the film.

Back-side switching (light source - substrate - C₅FHSAC)

In order to determine the back-side switching kinetics, the same evaluation methods as for the quartz substrate were applied as described in section 5.1.3. The opening process, which is initiated by visible light corresponds to the first-order kinetics and follows the equation 5.4. The extinction spectra (1-Transmission) are recorded with the light exposure in between and the corresponding kinetic coefficients can be extracted from the experimental traces.

In parallel, to corroborate the obtained kinetic coefficients, FDTD simulation was applied using the calculated refractive index of the C₅FHSAC film (Figure 5.5). The simulation confirmed the experimental transmission spectra in good agreement closely reproducing the main features of the nanohole array-C₅FHSAC structure (Figure A.12). However, there is no straightforward algorithm established to evaluate the switching kinetics in particular for absorbing materials like molecular films. Therefore, here a simple method was developed to quantitatively evaluate the kinetics on different substrates including compact Au, nanohole arrays, and quartz.

Generally, according to the formula $k = I_a \cdot \phi \cdot t$, the kinetic coefficient k is linearly proportional to the light intensity absorbed by the molecular film during switching, which is in the same terms linearly proportional to the square of the electrical field. Therefore, if the value of the square of the electrical field is determined within a molecular film, it can serve as a comparison factor to evaluate the rate of kinetics for all substrates.

The FDTD simulation enables to capture the electrical field within the x - z cross-section (Figure 3.5) of the substrates. The field is determined with high resolution in each node of mesh showing a nonuniform and complex distribution, in particular for hAu electrodes. Based on AFM measurements of the C_5FHSAc film (Figure 5.2 and 5.16), the FDTD simulation model assumes that for the hAu electrodes the nanoholes are completely filled with molecules and covered with an additional molecular layer of 18 nm thickness on top of the hAu surface. For hole-free substrates such as quartz and compact Au, the C_5FHSAc film is modeled to uniformly cover the surface with 18 nm thickness. The FDTD simulation corroborated with a good agreement the transmission spectrum of hybrid C_5FHSAc - nanohole arrays and C_5FHSAc - compact Au structures (Figure A.12 and A.13 b, d).

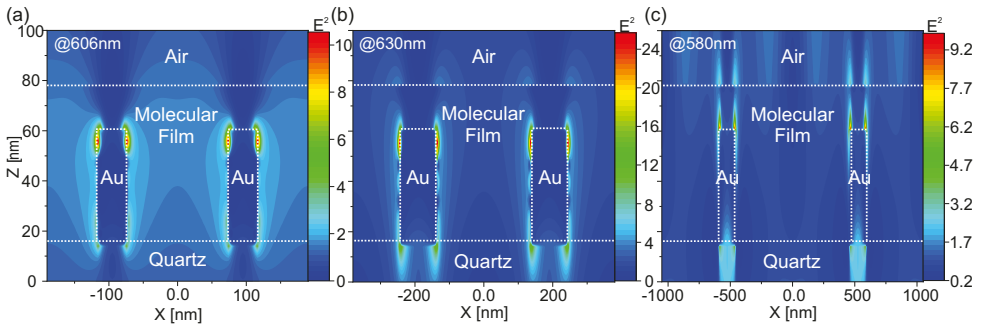


FIGURE 5.18: Spatial distribution of the square of the electrical field in the cross-section of hAu electrodes with molecular films at the wavelengths (606 nm, 630 nm, 580 nm) of the maximum extinction in the visible range (corresponding to the opening process): (a) lattice constant of 190 nm and cross-section at the wavelength of 606 nm, (b) lattice constant of 380 nm and cross-section at wavelength of 630 nm, (c) lattice constant of 1050 nm and cross-section at the wavelength of 580 nm.

The features related to the surface plasmon-molecular film interaction are expected to be observed in the visible range for the lattice constants of 190 and 380 nm. In particular, at the maximum of extinction of the C_5FHSAc film, where light is absorbed with the highest efficiency, the kinetic parameters were determined. The 2D cross-section through the square of the electrical field distribution of nanohole arrays with the lattice constant of 190 nm showed a high intensity (around 10 arb. units) at the edges of the hAu, which are ascribed to SPP formation (Figure 5.18 a). The field intensity decreases gradually with the distance from the hAu surface to values between approximately 1 and 3 arb.

5. Results & Discussion

units, while for 380 nm lattice the field drops from approx. 25 arb. units to similar values around 2 arb. units. (Figure 5.18 b). As predicted, the hAu electrode with the largest lattice constant of 1050 nm showed a more uniform distribution within the molecular film revealing values around 1 arb. units. The highest intensities observed (around 9 arb. units) are located at the edges of the hAu surface and under the film, which are ascribed to edge effects and reflection, respectively.

The spatial distribution of the square of the electrical field showed a complex spreading, which leads to the question of how to evaluate the intensity of light absorbed by the molecular film. The field is defined for different sample dimensions and mesh parameters making the summing of the values not sufficient for representing a comparison factor. On the other hand, the distribution revealed a wide spectrum of intensities with a pronounced peak at mean and median values (Figure 5.19) with the latter one being around the maximum of distribution. Thereby, the averaged median value was chosen to evaluate and

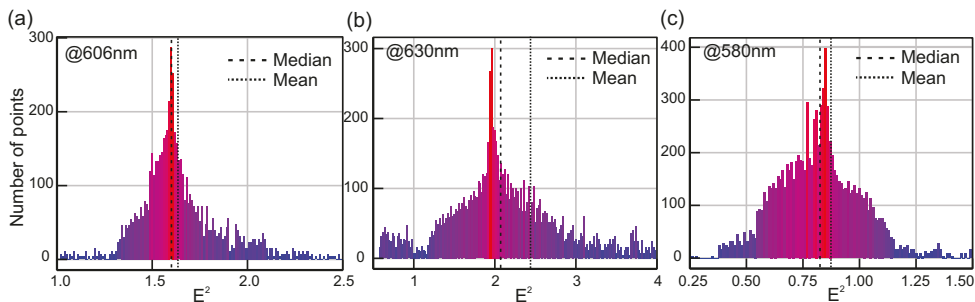


FIGURE 5.19: Histogram of the square of the electrical field values extracted within the molecular film for hAu electrodes with lattice constant of (a) 190nm, (b) 380nm, (c) 1050nm, which correspond to the electrical field distribution in Figure 5.18. The histograms show blow-ups of the distribution around the median and mean values.

compare the kinetics for the different substrates used here. Additionally, to quantitatively estimate the error of averaging, the absolute median deviation was calculated.

The 2D cross-section through hole-free surfaces such as quartz and compact Au showed a relatively uniform spatial distribution of the square of the electrical field (Figure A.14), making a small median deviation.

Furthermore, the opening process is triggered by a white-light source with a broad wavelength range from 450 nm to 700 nm (Figure 3.2), matching with the absorption range of the closed film leading to a non-uniform absorption efficiency, which depends on the respective wavelength. To take into account this feature and evaluate the opening kinetics, the median value of the square of the electrical field was determined at each wavelength within the closed C_5 FHSAc film. Firstly, the wavelength range of the largest white light absorption was defined for each sample. It corresponds to the FWHM of the

absorption spectrum obtained by subtraction of the spectra of the closed and open isomer (Figure 5.20).

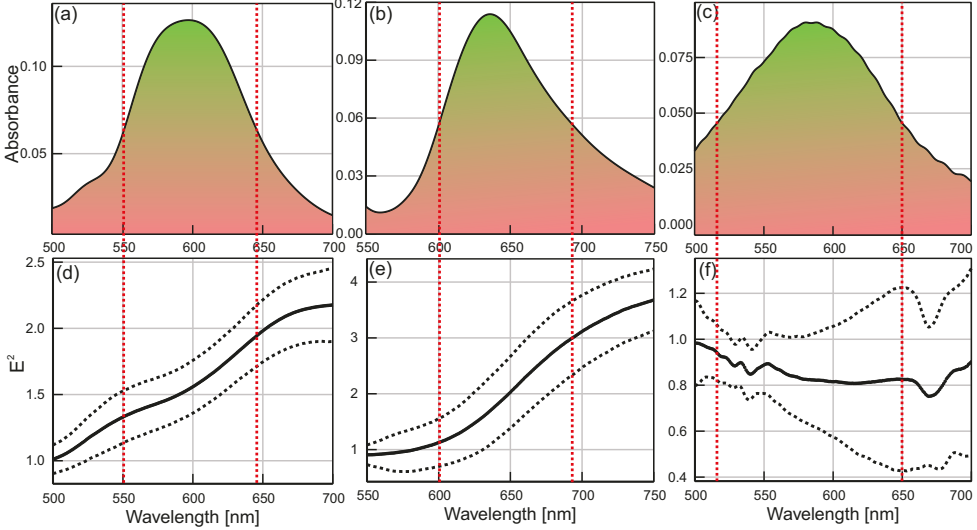


FIGURE 5.20: FDTD simulated absorption obtained as a difference between the absorption spectrum of open and closed films on hAu electrodes with lattice constant of (a) 190 nm, (b) 380 nm, (c) 1050 nm. Red dotted lines correspond to the full width at half maximum. Median values of the square of the electrical field inside the closed molecular film (represents an opening process) within the visible range for hAu electrodes with lattice constants of (d) 190 nm, (e) 380 nm, and (f) 1050 nm. Dotted lines denote the error obtained as median absolute deviation for each wavelength.

The FWHM was obtained for all substrates: quartz, compact Au, and nanohole arrays. The hAu electrode with the lattice constant of 190 nm showed the FWHM of 95 nm with a maximum at 597 nm (Figure 5.20 a), while the 380 nm lattice revealed the FWHM of 70 nm with a maximum at 642 nm (Figure 5.20 b). The nanohole arrays with a lattice of 1050 nm showed the FWHM of 134 nm with a maximum at 588 nm (Figure 5.20 c). Noteworthy, the median value increased with the wavelength towards the visible spectral range for lattices of 190 and 380 nm, while for 1050 nm it remained relatively constant deviating by around 0.8 arb. units.

The averaging of the square of the electrical field over the wavelengths in the range of FWHM was carried out according to the formula (equation 5.7) that represents the weighted mean value with absorption as weighting coefficient.

$$\langle E^2 \rangle = \frac{\sum_{i=\lambda_{min}}^{\lambda_{max}} A_i \cdot E_i^2}{\sum_{i=\lambda_{min}}^{\lambda_{max}} A_i} \quad (5.7)$$

5. Results & Discussion

where E_i^2 is the square of the electrical field at wavelength $\{i\}$, A_i is the absorption at wavelength $\{i\}$, $[\lambda_{min} : \lambda_{max}]$ corresponds to the FWHM range.

Considering all aforementioned conditions, both experimental and FDTD simulated kinetic coefficients were obtained (Figure 5.21). The experimental values were extracted

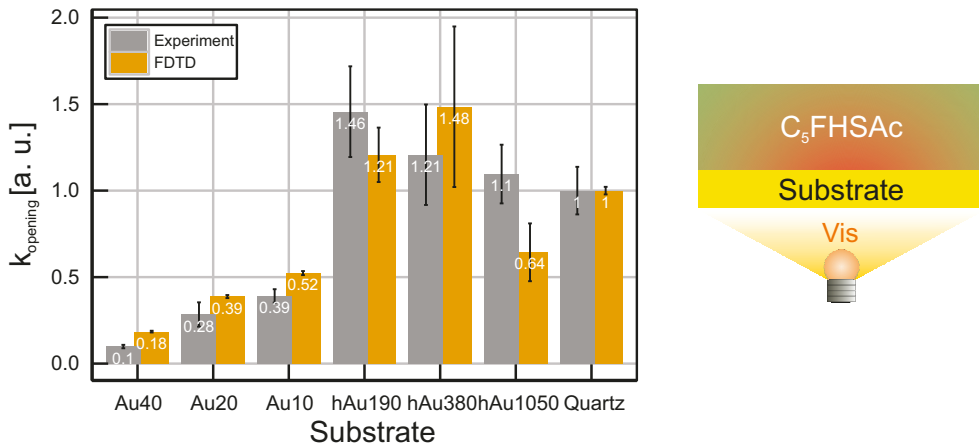


FIGURE 5.21: Kinetic coefficients of the opening process for back-side switching (light source-substrate- C_5FHSAc film). The experimental kinetic coefficients (gray) and error bars were extracted from the fitting by first-order kinetics 5.4 and standard deviation of the mean, respectively. The median values of the square of the electrical field (orange) within the molecular film with error bars obtained as median absolute deviation. Both experimental and simulated coefficients with respective errors were normalized by the corresponding value of the coefficient for the quartz substrate.

from kinetic traces recorded at the maximum of extinction, while weighted mean was applied to average median values of the square of the electrical field within the C_5FHSAc film. The errors are obtained as standard and absolute median deviation for kinetic traces and FDTD simulated data, respectively. In order to compare experimental and FDTD data, each coefficient together with errors was normalized to the reference value of the molecular film on quartz.

Clearly, the fastest opening kinetics is observed for the C_5FHSAc film on nanohole arrays, in particular, for the lattices with constants of 188 and 376 nm. The experimental coefficients appear to be by 46% and 21% faster for hAu electrode with lattice constant of 188 and 376 nm, respectively, in comparison with the almost fully transparent quartz substrate. Generally, the small deviation within the error range observed between the experimental and simulated data can be explained by several approximations applied during FDTD evaluation. As expected, the coefficients are strongly reduced for compact Au due to the limited ability of the light to reach the molecular film. This led to slow kinetic rates reduced by 90%, 72%, and 61% for 40, 20, and 10 nm Au thickness, respectively. The hAu

electrode with the largest lattice constant of 1050 nm showed a large deviation between experimental and simulated data in comparison with other samples, however, the kinetics reveal a relatively low coefficient that is by 36% smaller compared to quartz according to FDTD simulation. This may suggest the absence of surface plasmon enhancement for this lattice constant, which, however, was clearly observed for other hAu electrodes with lattices of 190 and 380 nm.

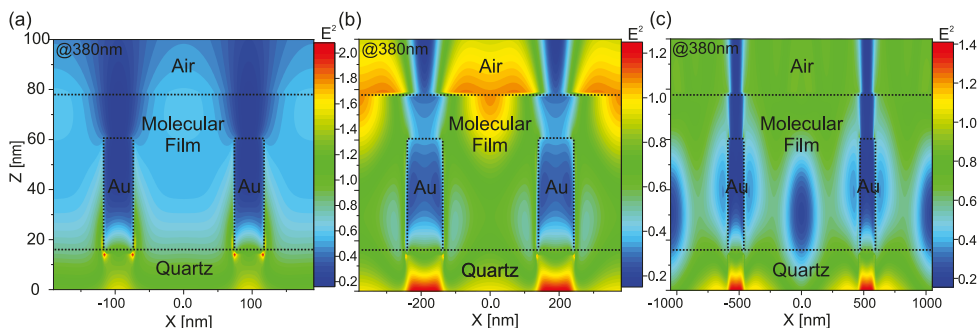


FIGURE 5.22: Spatial distribution of the square of the electrical field in the cross-section of hAu electrodes decorated with the molecular film for irradiation with $\lambda = 380$ nm (corresponding to the closing process): (a) lattice constant of 190 nm, (b) lattice constant of 380 nm, (c) lattice constant of 1050 nm.

Unlike the opening, the closing process is triggered by UV illumination within the narrow irradiation spectrum around 380 nm (Figure 3.2), which facilitates the kinetic evaluation. This means that the square of the electrical field can be straightforwardly captured at $\lambda = 380$ nm via 2D cross-section through substrates with an open C_5FHSAc film (Figure 5.22).

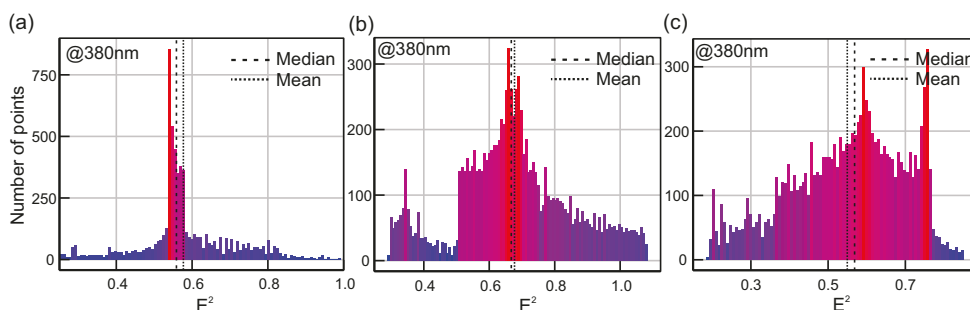


FIGURE 5.23: Histogram of the square of the electrical field values extracted within the molecular film for hAu electrodes with lattice constant of (a) 190 nm, (b) 380 nm, (c) 1050 nm, which correspond to the electrical field distribution at Figure 5.22. The histograms are zoomed around the median and mean values.

5. Results & Discussion

The spatial distributions for 190, 380, and 1050 nm nanohole array lattices as expected did not show SPP-related features but were rather affected by attributes ascribed to edge effects and reflectance. Moreover, the values of the square of the electrical field within the film laid in the range around 0.5 - 0.8 arb. units, which can be clearly observed in histograms (Figure 5.23). The distribution, in general, revealed a broader peak-to-peak spectrum of the square of the electrical field in comparison with the distribution for the opening process. However, the determined mean and median values are in close vicinity of the maximum, especially the latter one, which, similarly to the opening, was chosen to evaluate the closing process, too.

Furthermore, the experimental coefficients were extracted from the kinetics traces at the maximum of extinction. Therefore, in the same manner as for the opening process, both experimental and FDTD simulated values were normalized by the respective kinetic coefficients of the film on the quartz substrate (Figure 5.24).

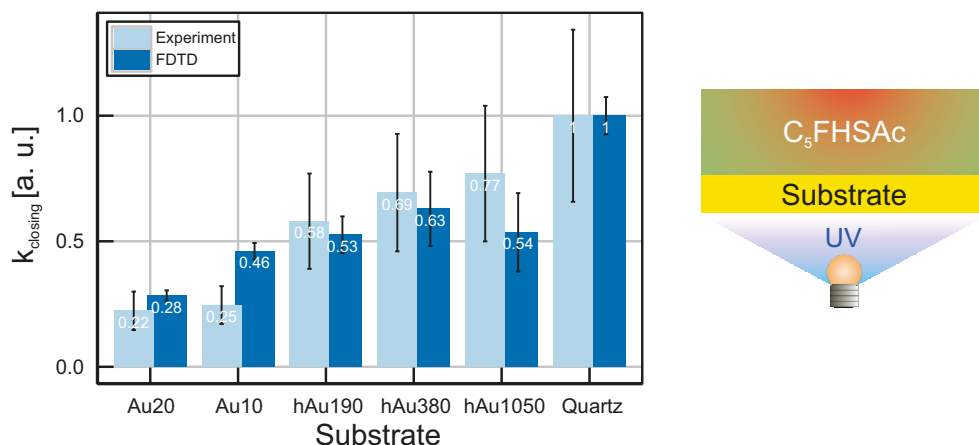


FIGURE 5.24: Kinetic coefficients of the closing process for back-side switching (light source-substrate-C₅FHSAc film). The experimental kinetic coefficients (light blue) and error bars are extracted from the fitting with equation 5.5 and standard deviation of the mean, respectively. The median values of the square of the electrical field (dark blue) within the molecular film with error bars obtained as median absolute deviation. Both experimental and simulated coefficients with respective errors bars are normalized by the corresponding value of the coefficient for the quartz substrate.

Unlike opening kinetics, both experimental and FDTD simulated values for all investigated nanohole arrays reveal slower closing rates in comparison with quartz substrates. In particular, the hAu electrodes of lattice constants 190, 380, and 1050 nm show slower kinetics by 42%, 31%, and 23%, respectively. As expected the compact gold films sufficiently filtered the UV light leading to much slower kinetic rates by 78% and 75% for thicknesses of 20 and 10 nm, respectively. There is a noticeable trend observed that the

5.3. Surface plasmon-enhanced switching kinetics

rate of kinetics increases from almost opaque substrates such as compact Au to more transparent materials like nanohole arrays and almost fully transparent quartz. This suggests that the closing kinetics for all substrates are directly linked to the transmission.

If the experimental results of closing (Figure 5.24, light blue) and opening (Figure 5.21, grey) are compared, the latter process exhibited smaller error bars in comparison with closing. Unlike the opening, where the error is the combination of the statistical error of the experiment and the fitting deviation based on the two-coefficient formula (equation 5.4), the fitting formula of the closing process (equation 5.5) consisted of four coefficients, which results in larger error bars. Additionally for FDTD obtained values, the closing process exhibited bigger error bars as well, which originate from much broader peak-to-peak field distributions in comparison with the values obtained for the opening process.

As mentioned above, the transmission configuration (light source - substrate - C_5 FHSAc film) involves light to be filtered by the substrate. The list of investigated substrates varies from almost fully transparent quartz material to an almost opaque compact Au. The nanohole arrays, due to the hole-patterned metal, owned higher transparency than a compact film of the same thickness and, therefore, have a less pronounced effect on the switching rate as a compact electrode. To take into account this geometrical feature

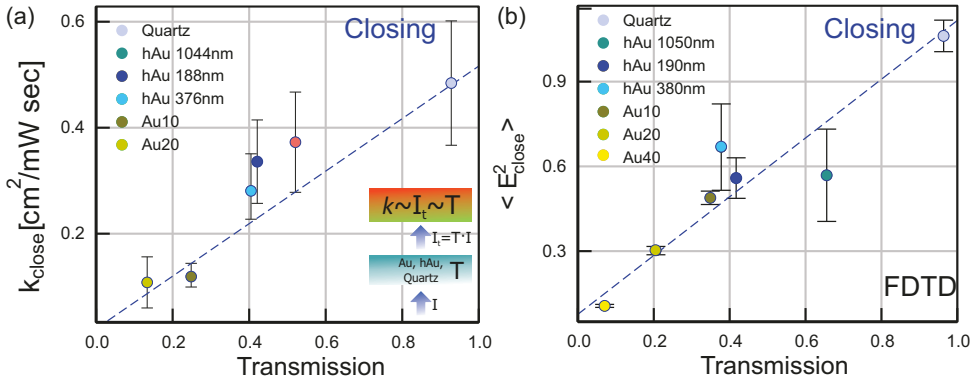


FIGURE 5.25: (a) Extracted kinetic coefficients of the closing process at the maximum of extinction for quartz, Au of different thicknesses, and hAu of different lattice constants plotted against the transmission of respective bare substrates. (b) Median value of the square of electrical field within a molecular film in open form (represents a closing process) on quartz, Au, and hAu substrates plotted correspondently against transmission of the respective bare substrate. The error bars in (b) are determined as median absolute deviation. The linear fitting is carried out for datapoints that correspond to compact substrates (Au, quartz).

and, thus, consider the contribution of the light intensity that is transmitted through the bare substrate and, thereby, is expected to be absorbed by the C_5 FHSAc film, the kinetic values obtained for both opening and closing processes by experimentally recorded traces and FDTD simulation (Figure 5.24 and 5.21) were plotted versus the transmission

5. Results & Discussion

of the bare substrate (Figure 5.25 and 5.26). Both experimental and simulated closing data (Figure 5.25) showed a linear dependence on the transmission through the respective sample. These results indicate that there is no significant influence of the nanohole arrays on the switching kinetics for the closing reaction which is in agreement with the expectation according to the determination of the kinetic coefficient $k = I_a \cdot \phi \cdot t$. In this case, only transmitted UV light contributed to the switching reaction without additional enhancement (e.g. surface plasmon enhancement).

In the same manner as the closing was analyzed, the opening kinetic coefficients were plotted versus the transmission of the bare substrates (Figure 5.26). Similar to the reverse

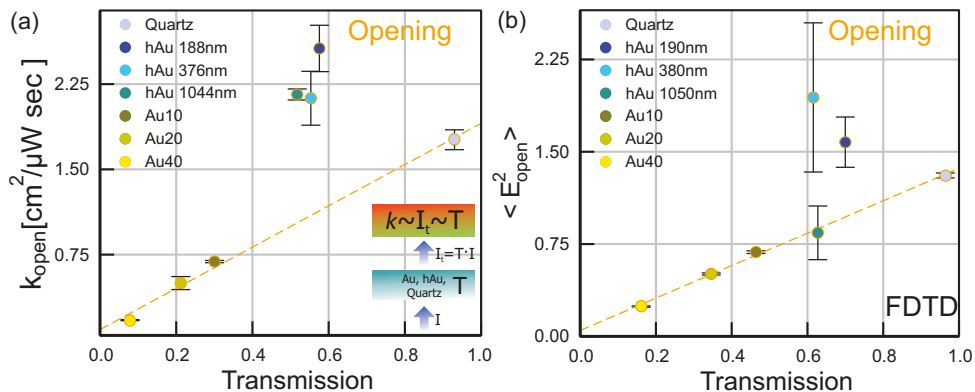


FIGURE 5.26: (a) Extracted kinetic coefficients of the opening process at the maximum of extinction for quartz, Au, and hAu substrates plotted versus the transmission of the bare substrate. (b) Median value of the square of the electrical field within a molecular film in the closed form (represents an opening process) on quartz, Au, and hAu substrates scaled to the transmission of bare substrate. The error bars in (b) are determined as median absolute deviation. The linear fitting is carried out for datapoints that correspond to compact substrates (Au, quartz).

closing reaction, here for the opening process, the compact Au and the quartz substrate reveal a linear dependence of k with the transmission. Assuming that there are no additional enhancing effects on the switching, the kinetic coefficients for hAu electrodes should also follow the aforementioned linear trend, as observed for the closing reaction. However, as already verified (Figure 5.21), there is an enhancement of the electrical field leading to faster kinetics than through quartz substrate. This leads to the fact that, for instance, the 188 nm lattice nanohole arrays revealed an ~ 2.3 times faster opening than expected based on the reference line, while 376 nm lattice hAu electrode showed ~ 2.1 times faster opening reaction. The measured and simulated accelerated opening kinetics can be assigned to the excitation of SPP which enhanced the strength of the electrical field, in particular, in the vicinity of the holes

The FDTD simulated kinetic characteristic for the largest lattice constant of 1050 nm is in good agreement with the reference line, which corroborates that molecules remained unaffected by surface plasmon enhancement and are switched only by the transmitted white light. The experimental results for this type of nanohole arrays showed faster opening kinetics than expected, presumably because of the somewhat smaller molecular film thickness of this electrode compared with other hAu electrodes as verified in section 5.3.1.

Front-side switching (light source - C_5FHSAc - substrate)

The transmission configuration (light source - substrate - C_5FHSAc) confirmed the surface plasmon enhanced field intensities, which lead to a faster opening reaction than through quartz substrates. This makes nanohole arrays suitable for vertical geometry devices, where they can serve as a conductive electrode that accelerates visible-light-triggered chemical reactions including molecular switching. However, the effect may be even stronger if the light illumination is performed directly on molecular films deposited onto nanohole arrays. In this scenario, the light is not filtered by the substrate leading to full conversion of the incident light into surface plasmon excitation. Additionally, the reflected light may play a role in further enhancing the switching reaction.

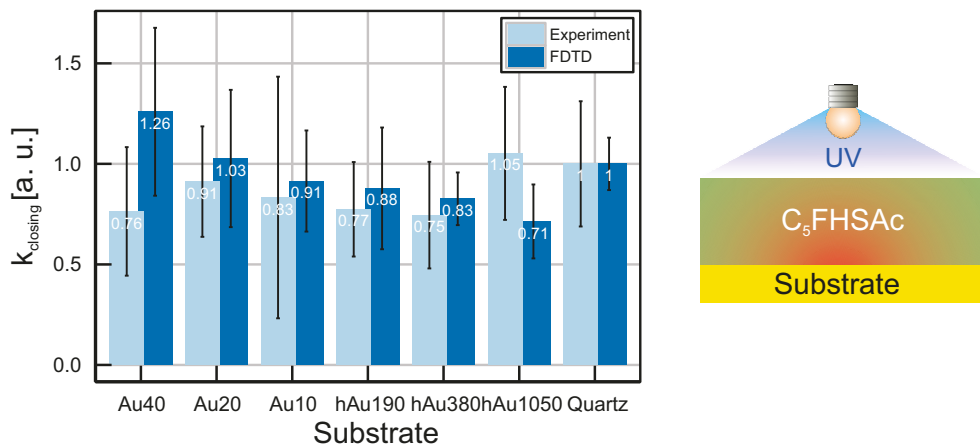


FIGURE 5.27: Kinetic coefficients of the closing process for front-side switching (light source- C_5FHSAc film-Substrate). The experimental kinetic coefficients (light blue) were extracted from kinetic traces by fitting with equation 5.5, the error bars were obtained as standard error of the mean. The FDTD simulated median values of the electrical field (dark blue) within the molecular film with error bars obtained as median absolute deviation. Both experimental and simulated coefficients with respective error bars were normalized by the corresponding value of the coefficient for the quartz substrate.

The front-side switching was characterized in the same manner as the back-side configuration. In the working space of the FDTD simulation only the position of the light

5. Results & Discussion

source was replaced with the output detector maintaining the position of the structure and electrical field monitor. The averaged median values were obtained for the opening and closing processes, while kinetic coefficients were extracted from experimental traces.

As verified, the closing process should not reveal additional surface plasmon assigned enhancement, but only kinetic rates defined by the incident light intensity. The results obtained for front-side closing reaction showed a relatively small deviation from the kinetic coefficient of the C_5FHSAc film on quartz (Figure 5.27). Almost all samples, in particular, nanohole arrays exhibited slower experimental and FDTD simulated kinetic values in comparison with quartz substrate. Furthermore, the results are obtained with relatively large errors, which makes the comparison more difficult. However, the general trend suggests that there is no sufficient enhancement occurring, but kinetics are affected by other factors e.g. reflection.

Unlike closing, the opposite process of opening as expected revealed certain enhancements, particularly, for nanohole arrays (Figure 5.28). Even though the experimental

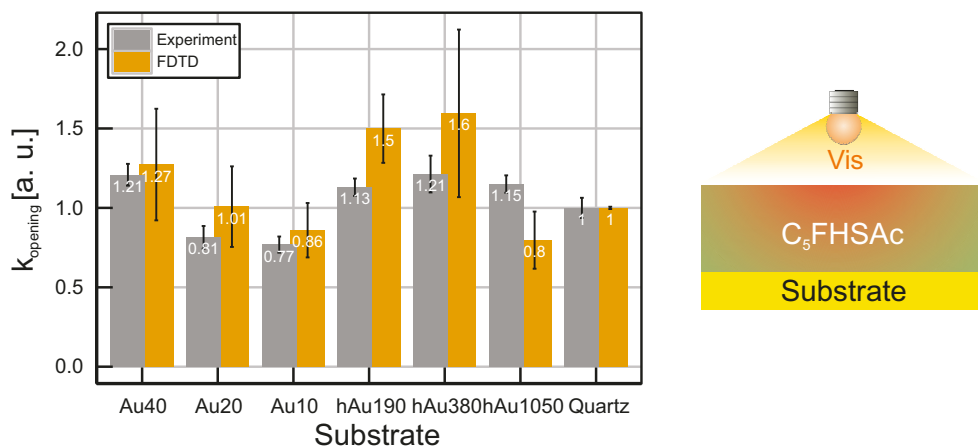


FIGURE 5.28: Kinetic coefficients of opening process for front-side switching (light source- C_5FHSAc film-substrate). The experimental kinetic coefficients (gray) and error bars were extracted from the fitting by first-order kinetics 5.4 and standard deviation of the mean, respectively. The median values of the square of the electrical field within the molecular film with error bars obtained as median absolute deviation. Both experimental and simulated coefficients with respective errors were normalized by the corresponding value of the coefficient for the quartz substrate.

data showed an increase in kinetic rates by 13% and 21% for hAu electrodes with lattices of 188 and 376 nm, respectively, the FDTD values revealed enhancement by 50% and 60%. These results indicate a surface plasmon assigned increase in light intensities, which does not occur for other substrates. Noteworthy, the gold films exhibited an increase in kinetics with the Au thickness. The compact Au with 40 nm thickness revealed 21% faster

kinetics than quartz substrate, which may be related to the reflection. The intensity of reflected light increases with the Au thickness, which suggests this to be the origins of the enhanced kinetics on compact films for front-side switching.

Impact of C_5FHSAc film thickness on kinetics

The results obtained here revealed some deviation between experimental and FDTD simulated data, which originates from several factors such as fitting algorithm, statistical deviation, and molecular film thickness. The latter may play a significant role, particularly, for nanohole arrays, since due to the geometrical features the thickness of the molecular film may greatly vary leading to somewhat thinner films.

In order to evaluate the impact of the film thickness on the switching kinetics, C_5FHSAc species was deposited onto quartz substrate from different initial concentrations of 1, 2, and 5 mM resulting in film thicknesses of around ~ 9 , ~ 18 , and ~ 36 nm, respectively. The approximate thickness was calculated according to the Lambert-Beer law based on the measured maximum extinction in respect to the known reference of the 18 nm film (Figure 5.29 a).

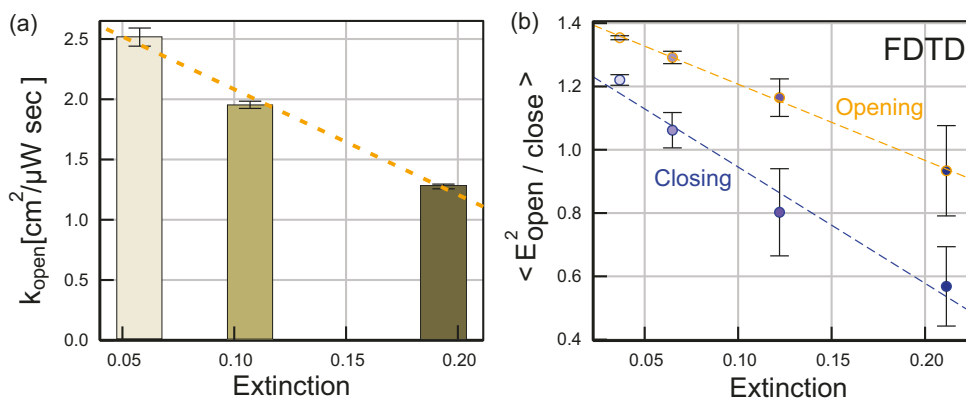


FIGURE 5.29: (a) Extracted kinetic coefficients for the opening process for the films of different thicknesses on quartz plotted versus the maximum value of extinction in the visible range. (b) Extracted values of the median values of the square of FDTD simulated electrical fields vs maximum extinction for the molecular film of 9 nm, 18 nm, 36 nm, and 72 nm thicknesses at 380 nm (blue) and averaged in the visible range (orange).

The switching was performed from the backside according to the configuration (light source - quartz - C_5FHSAc film) and the opening process was characterized based on the first-order kinetics (equation 5.4). As it can be seen (Figure 5.29 a), while the extinction increases, the opening kinetic coefficient decreases. This means that the rate of switching is directly correlated with the film thickness revealing an almost linear trend. To verify the

experimental results, FDTD simulation was performed testing film thicknesses of 9, 18, 36, and 72 nm (Figure 5.29 b). Both processes of opening and closing were characterized according to the aforementioned algorithm of capturing a square of electrical field and analyzing it in terms of averaging median values. FDTD simulations corroborated the experimental results confirming a linear decrease of the square of the electrical field in respect to the increase of the maximum extinction. According to the obtained results, the intensity of the electrical field for the opening process drops by around 30% with the increase of the thickness by a factor of 8. In contrast, the experimental results show a larger decrease by approx. 50% with the increase in thickness by a factor of 4.

Furthermore, the aforementioned decrease in kinetic rate with the thickness suggests that the enhancement of switching on nanohole arrays may be even stronger in comparison with hole-free flat surfaces. Especially, the quantitative disagreement between FDTD simulated and experimental kinetic results for the hAu electrode with the largest lattice constant of 1050 nm may originate from C₅FHSAc film thickness.

5.4 ELECTRICAL MEASUREMENTS OF DIARYLETHENES

Electrical reversible switching of diarylethenes was reported in single-molecule junctions as well as in the form of thick organic films mixed with conductive polymers. Here, along with the optical measurements, in order to test the electrical response of the C_5 FHSAc film, the pure solution of molecular species was employed without adding extra components e.g. polymer matrices. This was done to prevent the possible interference of the responses.

The electrical measurements of a C_5 FHSAc film sandwiched between bottom and top electrodes in the crossbar configuration were carried out according to the methods described in sections 3.3 and 4.4. Firstly, the switching ability of molecular species was tested by performing separated measurements of open and closed states employing hole-free bottom electrodes. Subsequently, the UV-vis live switching was tested utilizing nanohole perforated bottom electrodes. The results described below were conducted in collaboration with S. Tang and introduced in [151].

5.4.1 SWITCHING ABILITY OF C_5 FHSAC MOLECULES

To test the switching ability of C_5 FHSAc molecules, two independent scenarios were performed. The molecular species with an initial concentration of 5 mM were initially exposed to visible light converting the solution to the open state. Subsequently, the molecules were deposited by means of spin-coating (see section 3.1.4) and sandwiched

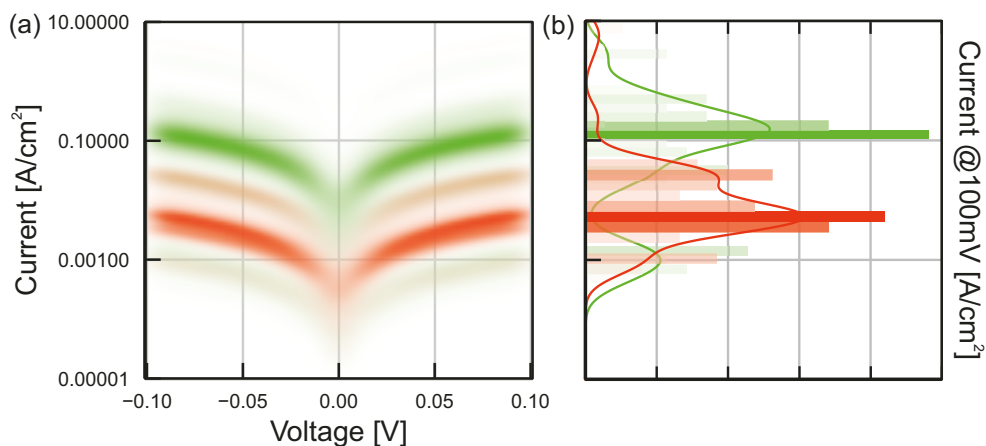


FIGURE 5.30: (a) Current density distribution with corresponding (b) frequency histogram measured on crossbars with compact bottom and top electrodes with junction area of $16 \mu\text{m}^2$. The red and green I-V curves stand for the C_5 FHSAc film spin-coated in open and closed form, respectively.

between hole-free compact bottom electrode and top electrode fabricated by transfer onto

POP substrate. Both electrodes possessed 4 μm wide leads forming a junction area of 16 μm^2 . The current density-voltage traces were recorded in the range of $\pm 100\text{mV}$ and plotted correspondingly (Figure 5.30 a, red). The same preparation procedure was carried out with initial UV light exposure to record response of closed C_5FHSAc molecules (Figure 5.30 a, green).

If the cross-section at 100 mV is taken and plotted correspondingly as a frequency histogram (Figure 5.30 b), two decent current density peaks can be distinguished. These peaks can be attributed to closed and open C_5FHSAc molecules. Noteworthy, the 5 mM solution was expected to form relatively thick films of approx. 70 nm, meaning that hopping electron transport should be dominating. Additionally, the current density for each state exhibited a wide distribution, however, narrow enough to conclude around one order of magnitude difference between open and close states. The obtained current values showed a good agreement with already reported diarylethene-based large-area junctions [11].

5.4.2 LIVE SWITCHING OF C_5FHSAc MOLECULES

In order to test the live switching ability of C_5FHSAc molecules, the molecular solution of 1 mM concentration was deposited on bottom electrodes fabricated by NSL by means of spin-coating (see section 3.1.4). Before deposition, the molecules were switched to open state to test the UV light initiated closing and to closed state to check the visible light-triggered opening process.

In case of closing (Figure 5.31 a), the C_5FHSAc molecules were sandwiched between 10 μm wide bottom and 6 μm wide top electrodes. As can be seen, the current increases during the UV illumination approx. by the factor of 6 confirming the expected trend. Noteworthy, there is a drop of current occurring after reaching saturation, which is repeatedly observed for the other experiments [151]. After this drop, the signal stabilizes in time, which can be attributed to the open state. Moreover, the noise associated with the signal (Figure 5.31 a, grey lines) dramatically increases near the peak subsequently reducing after the current drop. These two effects such as noise increase and current drop may be linked to each other and related to the molecular order. During UV triggered closing process, molecules tend to alter their chemical configuration, which consequently makes the molecular film a disordered matrix with more scattering centers for the electrons.

To test the opening of C_5FHSAc molecules, they were sandwiched between 6 μm wide bottom and top electrodes. Unlike the closing, for opening process the current associated with the molecular signal is expected to decrease during visible light illumination. As can be seen in Figure 5.31, b), there is no change of the signal during the opening process, which repeatedly was observed for other tests in [151].

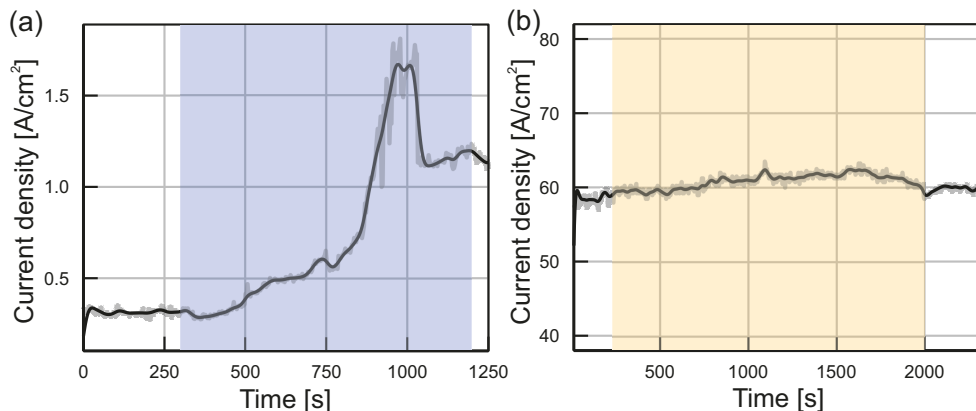


FIGURE 5.31: Live switching of C_5FHSAc molecules. (a) UV light initiated closing (corresponds to the violet range) showing an increase of current density, (b) Visible light-initiated opening (corresponds to the orange range) showing stable signal, which was expected to decrease. The original current time traces (grey lines) were smoothed out with low frequency filter (black lines).

Unidirectional electrical switching with only closing occurring was already reported for other geometries e.g. multilayer graphene electrodes [11], suggesting that the electronic couplings Γ (see section 2.1.1) correlate with the photoswitching behavior. In this case, the coupling may be stronger for closed molecules supporting proper electron transport. Additionally, the lack of free volume for a conformational change in the molecules within the solid film may contribute to the quenching of the opening process [73].

Noteworthy, molecules were able to support bidirectional optical switching on hAu electrodes revealing two stable states. Thereby, surface plasmon-related heating or other factors should not hinder the electrical switching capability.

CHAPTER 6

SUMMARY & OUTLOOK

Plasmonic large-area molecular contacts based on nanohole arrays were realized enabling to increase the switching rate of photochromic molecules via surface plasmon-enhanced fields. Diarylethenes served as the model compound to study the influence of SPPs on the kinetic coefficients of visible-light-triggered reactions such as molecular switching.

The excitation of SPPs via nanohole arrays fabricated by nanosphere lithography (NSL) were investigated as a function of geometrical features like lattice constant, metal thickness, hole diameter, incident angle, and surrounded media showing a strong optical transmission (around $\sim 60\%$) and an enhancement of electrical field intensities up to a factor of 25 inside diarylethene solid films. Two different scenarios of back- and front-side switching were studied to evaluate the contribution of SPPs to kinetic rates. The experimental data were evaluated by FDTD simulations confirming an SPP-induced enhancement up to 50% compared to quartz substrate of the visible-light-triggered switching opening reaction on nanohole arrays.

Based on the systematic analysis of the SPP resonance as a function of kinetic parameters, it was confirmed that the enhancement effect is strongest when the wavelength range of the SPP resonance overlaps with the range of molecular absorption. Moreover, modifying the SPP resonance parameters and thickness of the molecular film can lead to even faster kinetics than observed in this work.

To realize the electrical switching the fabrication methods to implement nanohole arrays into large-area molecule junctions were developed proposing two schemes for completing nanohole arrays-molecule-metal contact. Unidirectional switching of diarylethenes was achieved enabling the UV-activated closing reaction and hindering the visible-light-triggered cycloreversion. Taking into account the fact that optical responses of bidirectional switching were observed, this suggests several factors that can be modified to

6. Summary & outlook

improve the electrical opening. The coupling between molecule and, in particular, the top metal electrode should play a key role. This can be improved by modifying the junction geometry e.g. roughness of the electrodes, thickness of the passivation layer, molecule film thickness, etc.

ACKNOWLEDGEMENTS

I would like to extend my deepest gratitude to my colleagues, friends, and family who helped and encouraged me during all the steps of completing this PhD path. I very much appreciate your support and would like to pay my special regards to the following people:

Dr. Dirk Mayer: I'm extremely grateful to you for the patient guidance, enthusiastic encouragement, and useful critiques during my PhD research journey. Your extensive suggestions helped me not only to grow professionally but also to develop my personal skills. Thank you for continuous support, help, and empathy.

Prof. Dr. Elke Scheer: I would like to sincerely thank you for your great supervision of my work. Your guidelines have been invaluable to me since I started my PhD. Thank you for shaping my experiment methods and critiquing my results. Your insightful feedback and immense knowledge helped to bring my works to a higher level.

Prof. Dr. Andreas Offenhäusser: I would like to thank you for supervising and supporting my work. Thanks to you, our institute became a place with a friendly work environment and atmosphere, where it is only a pleasure to work at.

Dr. Thomas Huhn, Prof. Dr. Johannes Boneberg, Mikhail Kabdulov: Many thanks for the useful discussions and practical support of all parts of this project. Special thanks to **Thomas** and **Mikhail** for synthesizing molecules, which without doubt are one of the main components of this work.

Dr. Volker Schöps: I very much appreciate your support and help, especially at the beginning of my PhD journey, which helped me to have a smooth start.

Songyao Tang: Thank you for contributing results to this work and project in total, which greatly helped me. I had the great pleasure of working with you and be your supervisor.

Prof. Dr. Svetlana Vitusevich: Thank you for relentless support, especially before I even started, which helped to make this PhD journey possible.

Timm J. J. Hondrich, Gabriela Figueroa-Miranda, Antonio Minopoli, Viviana Rincón Montes: Many thanks to you all for the collaborative ideas we imple-

mented and realized as novel projects. It has been an incredible experience and pleasure working with you together.

Regina Stockmann, Michael Prömpers, Marko Banzet, Elke Brauweiler-Reuters: I would like to thank you for your extensive support, help, and practical suggestions regarding technical issues of cleanroom fabrication.

Nazarii Boichuk, Hossein Hassani, Dr. Sergii Snegir, Dr. Gillian Kiliani: Many thanks go to you for helpful scientific discussions on mathematical modeling and experimental support, which helped to shape this project.

Zidu Li, Ivan Pavlushko: Special thanks go to you for contributing results to our collaborative projects. It was a great pleasure and experience supervising you.

Dr. Stefan Trelenkamp, Dr. Florian Lentz, Dr. Elmar Neumann, Stephany Bunte, and other HNF staff: Many thanks to you for supporting my work with electron-beam lithography, SEM, FIB, and various useful cleanroom-related discussions.

Mirjam Seller, Roswitha Gielen, Sabine Wallrabe, Eva Dutt, Susanne Bipus, Sabine Lucas: I would like to thank you all for continuous support and help with the huge amount of bureaucracy I had to deal with during all years of PhD.

Tina Breuer, Dr. Vanessa Maybeck: Thank you for the great positive vibes and for rescuing the institute from all organizational problems. Special thanks to **Vanessa** for organizing the annual pumpkin carving.

Martin Prestel, Sergej Andreev: Many thanks for helping with all the bureaucracy related to the submission of the dissertation.

Sascha Thiele, Stefan Kirch, and other IT staff: Thank you for your constant support with technical IT issues.

Jamal, Pegah, Viviana, Ekaterina, Kagithiri, Erfan, Nouran, Lena, Timm, Gabriela, Nazarii, Ihor, Volodymyr, Yurii, Corrina, Chris, Jelena, Dominik, Frano, and other members of **IBI3:** Thank you all for an incredible experience and unforgettable adventure. I very much appreciate you being always supportive, enthusiastic, and amusing colleagues and friends. I'm taking away some great memories of not only working with you all, but our numerous activities like winter and summer schools, and others.

I am also grateful to my friends **Mathis, Anzhela, Alexey, Nikolai, Karina** who I can always count on in daily life.

My family: I am deeply thankful to you for your boundless love and support. Thank you for always being there whenever I need you. Your guidance, patience, and care encouraged me to pursue my dreams. I am forever indebted to you for giving me the experience and knowledge that always inspired me during all these years. You have always believed in me, which helped me reach where I am today.

APPENDIX A

APPENDIX

A.1 PROTOCOLS

Bottom electrode by NSL

- Dehydration of 4" quartz or SiO_x wafer on the hot plate at 150°C for approximately 10 min.
- Spin-coating of LOR3B resist at 3000 rpm for 40 sec with an acceleration of 500 rpm/s. Spin-coating is carried out with closed lid.
- Soft baking at 150°C on the hot plate for 5 min to evaporate the residues of resist solvent.
- Spin coating of nLOF2020 photoresist at 3000 rpm for 40 sec with an acceleration of 500 rpm/s (closed lid).
- Soft baking at 100°C for 2 min.
- Exposure by a Mask Aligner (i-line) with 55 mJ/cm² and 40 mJ/cm² for quartz and SiO_x substrate, respectively. The utilized mask is shown in figure A.6.
- Post-exposure baking on the hot plate at 110°C for 1 min.
- Development in MIF 326 for 35 sec. Constant moving during process to support uniform development followed by rinsing in DI water.
- Cleaning RIE chamber in the following conditions:
 - SF₆ (100 sccm), RF power 200 W, ICP power 2000 W, time 20 min.
 - SF₆/Ar/O₂ (40/10/50 sccm), RF power 200 W, ICP power 2000 W, time 20 min.

A. Appendix

- Ar/O₂ (20/40 sccm), RF power 200 W, ICP power 2000 W, time 40 min.
- Conditioning RIE chamber with the etching protocol: Ar/CHF₃ (30/5 sccm), RF power 120 W, pressure 0.02 mbar, time 20 min. The Helium flow is kept constant at around 5 sccm.
- Etching the quartz/SiO₂ substrate. The time is chosen based on the rate of 12.9 nm/min (Figure 4.8). To get the trench of around 50 nm depth, the time of etching is 4 min.
- Cleaning the substrate in oxygen plasma to prepare for the following PS particle deposition. The parameters: O₂, pressure 0.7 mbar, power 200 W, time 5 min.
- PS particle deposition is described in section 4.1.1.
- Cleaning the RIE chamber with the aforementioned protocol.
- Conditioning RIE chamber with the particle etching protocol: O₂/CHF₃ (40/10 sccm), RF power 30 W, pressure 0.026 mbar, $T = 0^{\circ}\text{C}$, time 20 min.
- Etching particles. The time is chosen based on the particles' diameter and dimensions of the substrate (section 4.1).
- Metalization of titanium 5 nm at the deposition rate of 0.1 nm/s followed by Au deposition 40 nm at the rate of 0.5 nm/s.
- Lift-off of the nLOF2020 resist in acetone (app. 10 h) followed by immersing in MIF326 developer to remove residuals of LOR3B resist. Rinsing the substrate in isopropanol and DI water.
- Particle lift-off by means of an adhesive tape followed by ultrasonication in acetone, isopropanol and DI water.
- Conditioning RIE chamber with the following protocol: O₂, RF power 200 W, pressure 0.026 mbar, $T = 20^{\circ}\text{C}$, time 20 min.
- Etching the residuals of resist: O₂, RF power 200 W, pressure 0.026 mbar, $T = 20^{\circ}\text{C}$, time 5 min.
- Dicing into 13.5x13.5 mm² chips.

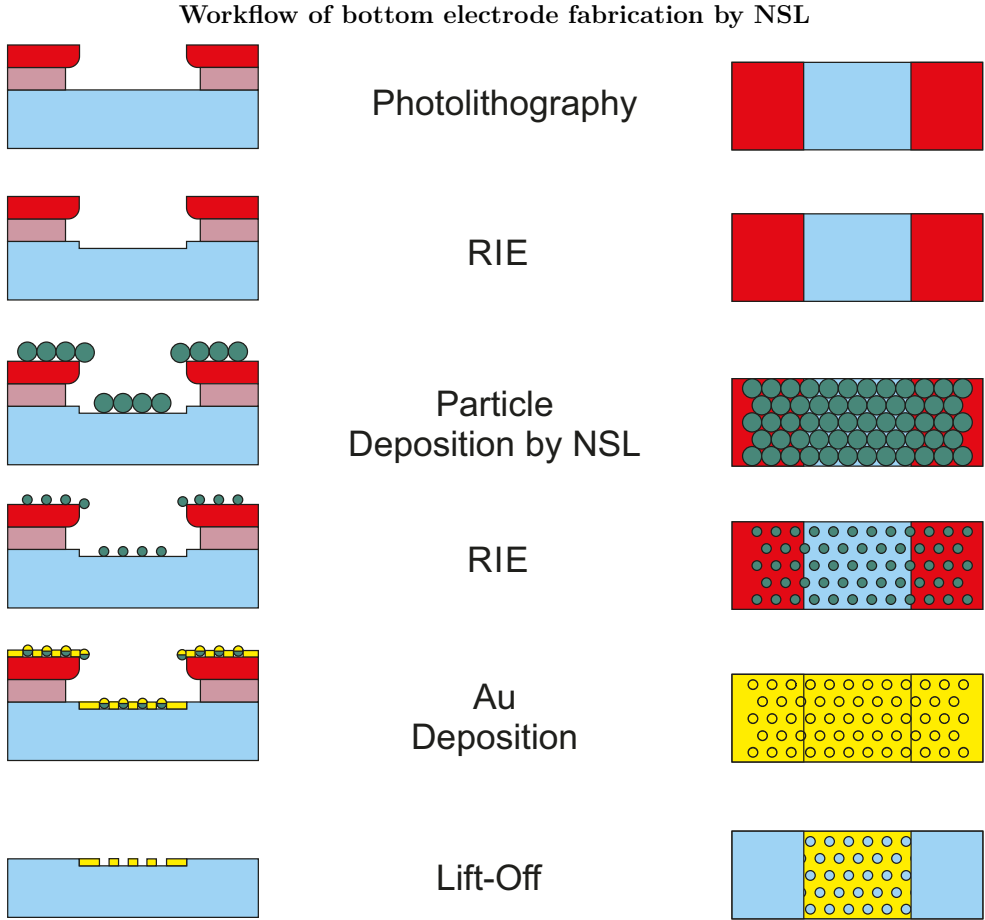


FIGURE A.1: Schematic drawing representing bottom electrode fabrication by NSL. Left column - side view, right column - top view.

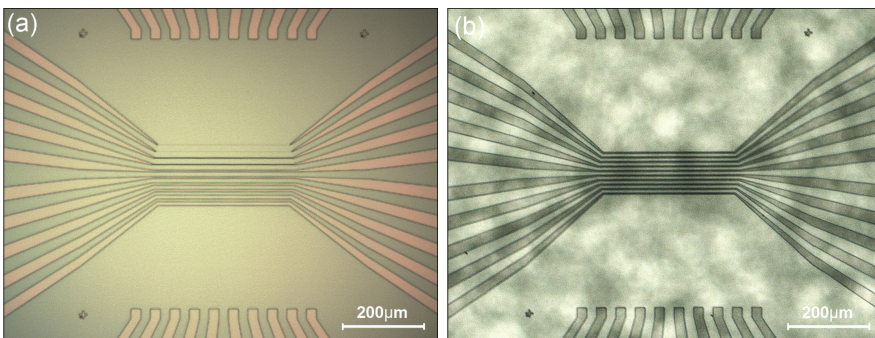


FIGURE A.2: Double layer LOR3B and negative photoresist nLOF2020 after development showing a designed pattern of the bottom electrode. (a) SiO_x substrate, "Grad" chip with the pair leads of 10 μm , 6 μm , 4 μm , 2 μm , and 1 μm ; (b) Quartz substrate, chip with 4 μm wide leads.

Bottom electrode by electron-beam lithography

- Metal deposition of chromium (Cr) 5 nm at 0.1 nm/s onto 4" quartz wafer.
- Dehydration of the wafer on the hot plate at 185°C for approximately 5 min.
- Spin-coating of PMMA resist AR-P 639.04 50K at 2000 rpm for 60 sec with an acceleration of 500 rpm/s. Spin-coating is carried out with closed lid.
- Soft baking at 185°C on the hot plate for 5 min to evaporate the residues of resist solvent.
- Spin coating of PMMA resist AR-P 649.04 200K at 2000 rpm for 60 sec with acceleration of 500 rpm/s (closed lid) followed by soft-baking at 180°C for 2 min.
- Electron-beam writing of the mask A.7 with dose of 375 $\mu\text{C}/\text{cm}^2$ and acceleration voltage of 100 kV.
- Development in AR 600-55 for 2 min with constant moving to support uniform development.
- Rinsing in isopropanol for 5 min.
- Metalization of Cr 3 nm at the deposition rate of 0.1 nm/s followed by Au 40 nm at rate of 0.5 nm/s. The Ar sputtering is carried out before Cr deposition with voltage of 80 V and current of 2 A for 15 sec.
- Lift-off of the PMMA double layer resist in acetone (app. 1 h) followed by immersing in isopropanol and DI water.
- Lift-off of the resist residues by means of adhesive scotch tape.
- Lift-off of the resist and tape residuals by Megasonic (50% power, 20 min) followed by immersing in IPA and DI water.
- Conditioning RIE chamber with the chromium etching protocol:
 - Cl_2/O_2 (30/20 sccm), RF power 25 W, ICP power 1800 W, pressure 0.03 mbar, $T = 20^\circ\text{C}$, time 5 s.
 - Cl_2/O_2 (30/20 sccm), RF power 25 W, ICP power 1000 W, pressure 0.03 mbar, $T = 20^\circ\text{C}$, time 20 min.
- RIE etching of chromium layer:
 - Cl_2/O_2 (30/20 sccm), RF power 25 W, ICP power 1800 W, pressure 0.03 mbar, $T = 20^\circ\text{C}$, time 5 s.
 - Cl_2/O_2 (30/20 sccm), RF power 25 W, ICP power 1000 W, pressure 0.03 mbar, $T = 20^\circ\text{C}$, time 10 s.

- ALD of Ta_2O_5 with the following conditions:
 - Power 300 W, pressure 0.107 mbar, $T = 200^\circ\text{C}$.
 - Number of cycles was chosen based on the desired resulting thickness according to the deposition rate of 10 nm per 125 cycles.
- Spin-coating of AZ5214E at 4000 rpm for 60 sec followed by soft baking at 105°C for 60 sec.
- Exposure with $75 \text{ mJ}/\text{cm}^2$ utilizing mask A.8.
- Development in MIF326 for 50 sec.
- Conditioning RIE chamber with the etching protocol: Ar/ CHF_3 (30/5 sccm), RF power 120 W, pressure 0.02 mbar, time 20 min.
- Etching Ta_2O_5 layer for 150 sec.
- Resist removal in acetone, isopropanol, and DI water.
- Dicing into $14 \times 14 \text{ mm}^2$ chips.

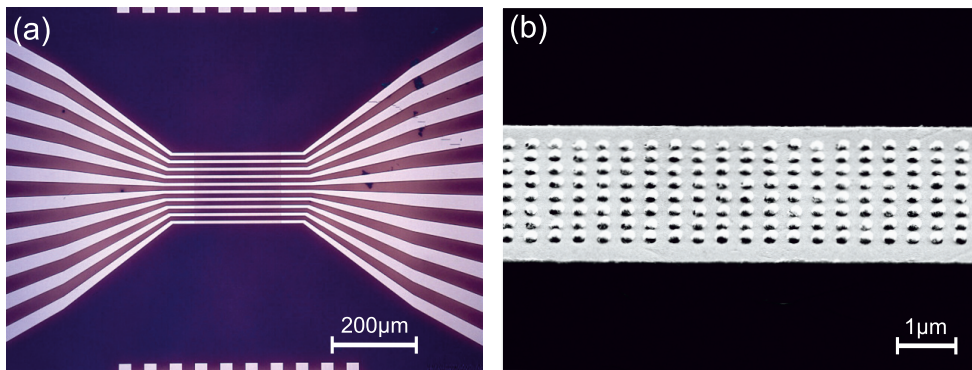


FIGURE A.3: (a) Optical image of the developed double layer of PMMA resist for $6 \mu\text{m}$ width bottom electrode, scale bar $200 \mu\text{m}$, (b) SEM image of $4 \mu\text{m}$ wide lead after deposition of Au and Ti followed by lift-off in acetone. The resist undercut was not effective enough, which led to the remaining parts inside nanoholes.

Top electrode by transfer onto POP stamp

- Dehydration of 4" SiO_x wafer on the hot plate at 150°C for approximately 10 min.
- Spin-coating of nLOF2020 photoresist at 3000 rpm for 40 sec with an acceleration of 500 rpm/s (closed lid).
- Soft baking at 100°C for 2 min.
- Exposure by a Mask Aligner (i-line) with 40 mJ/cm² utilizing mask depicted in figure A.9.
- Post-exposure baking on the hot plate at 110°C for 1 min.
- Development in MIF 326 for 35 sec. Constant moving during process to support uniform development followed by rinsing in DI water.
- FOTCS deposition in the glovebox:
 - Activation of the SiO_x by plasma treatment: gas O₂, pressure 1 mbar, power 80 W, time 5 min.
 - Transfer wafers into a desiccator, pipette 300 μL PFOTCS.
 - Set an Ar pressure in a desiccator at 5 mbar, silanize for 90 min.
- Metallization of 40 nm Au with a rate of 0.5 nm/s at low vacuum conditions.
- Lift-off in acetone for ~2 h followed by rinsing in isopropanol and DI water (acetone lift-off without ultrasonic treatment).

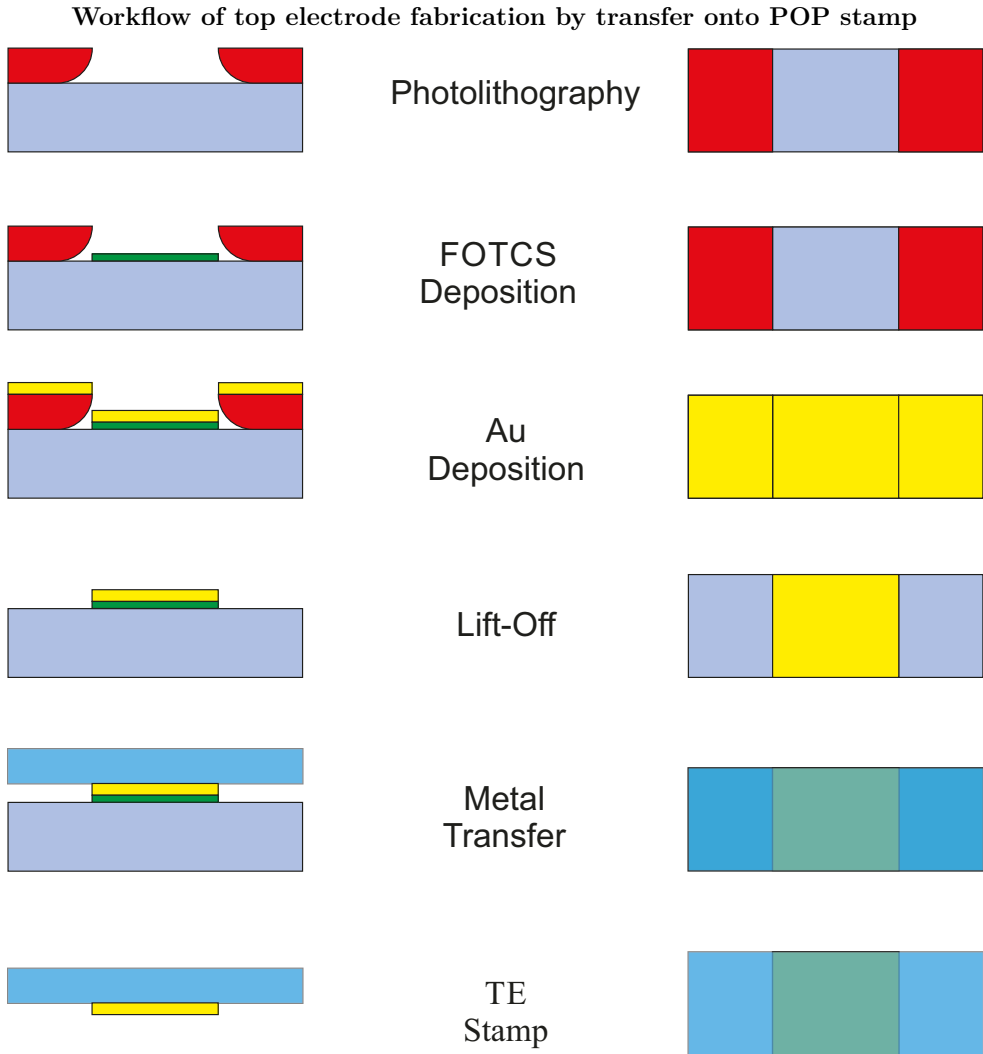


FIGURE A.4: Sketch representing top electrode fabrication by transfer onto POP stamp. Left column - side view, right column - top view.

Top electrode by direct fabrication onto POP

- FOTCS deposition onto two 4" SiO_x wafers according to the protocol described in A.1.
- Cleaning the 4" POP substrate in isopropanol and DI water.
- Imprint Nanonex 2000 (to make the surface smooth):

A. Appendix

- Sandwich POP substrate between two SiOx wafers.
 - Vacuum for 2 min.
 - Imprint at 90 °C, 60 psi (4.1369 bar) for 5min.
 - Cooling down to 35 °C.
 - Detach the POP from SiOx wafers by immersing in isopropanol.
- Spin coating of AZ5214E resist at 4000 rpm for 60 sec with an acceleration of 500 rpm/s. The spin-coating is carried out with closed lid.
 - Soft baking at 65 °C on the hot plate for 20 min.
 - Exposure by a Mask Aligner (i-line) with 75 mJ/cm² utilizing mask depicted in figure A.9.
 - Development in MIF326 for 50 sec. Constant moving during process to support uniform development followed by rinsing in DI water.
 - Wet etching of gold in TechniEtch AC12 for 1 min.
 - Wet etching of Ti in TechniEtch TC for 2.5 min.
 - Removal of the AZ5214E resist in acetone for 5 min followed by rinsing in isopropanol for 5 min.

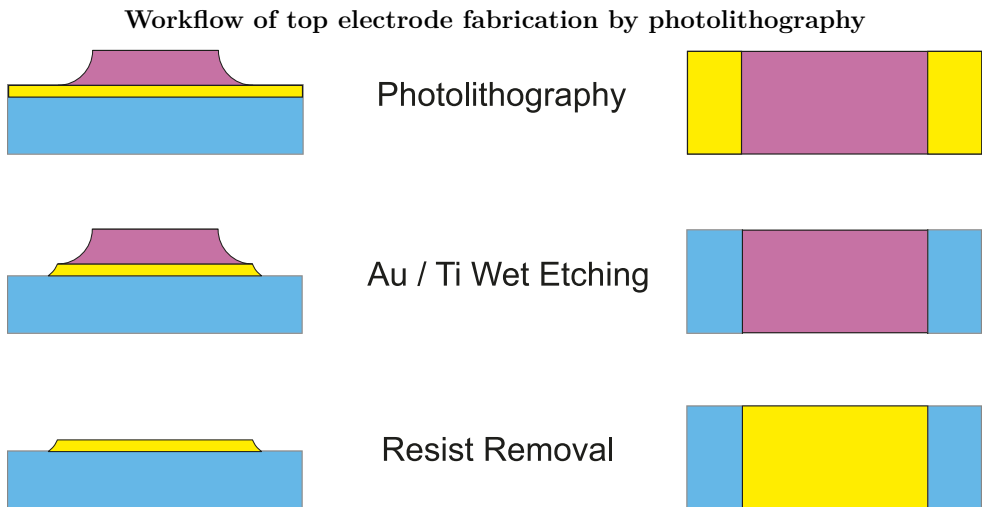


FIGURE A.5: Sketch representing top electrode fabrication by photolithography. Left column - side view, right column - top view. Blue substrate represents a 4" POP wafer, yellow color corresponds to the Au/Ti layer, violet color denotes the positive resist AZ5214E.

A.2 PHOTO- AND E-BEAM FABRICATION MASKS

Photomask design for bottom electrode fabricated by NSL

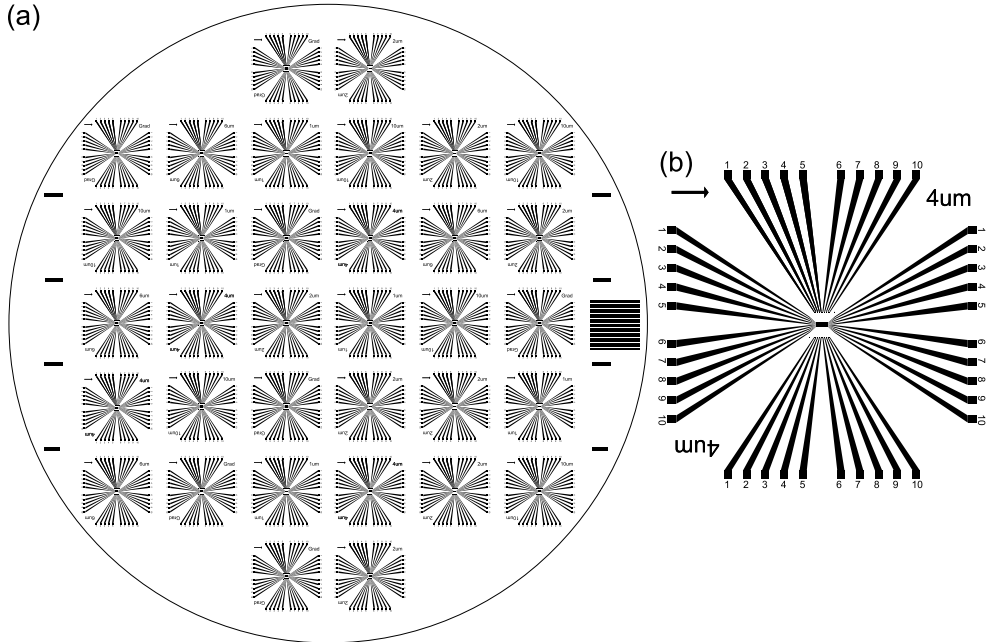


FIGURE A.6: Photomask layout for bottom electrode fabricated by NSL. (a) The mask is designed for a 4" wafer, which consists of 34 chips with etching marks on the right side for Dektak etching test. Each chip is designed to include 10 leads with different widths of 1 μm , 2 μm , 4 μm , 10 μm , and "Grad" (includes pair of all widths). The leads are positioned with 10 μm interdistance. (b) The 4 μm width chip layout, which consists of 10 leads connected to feedlines and contact pads for top electrode assembling.

Mask design for bottom electrode fabricated by e-beam lithography

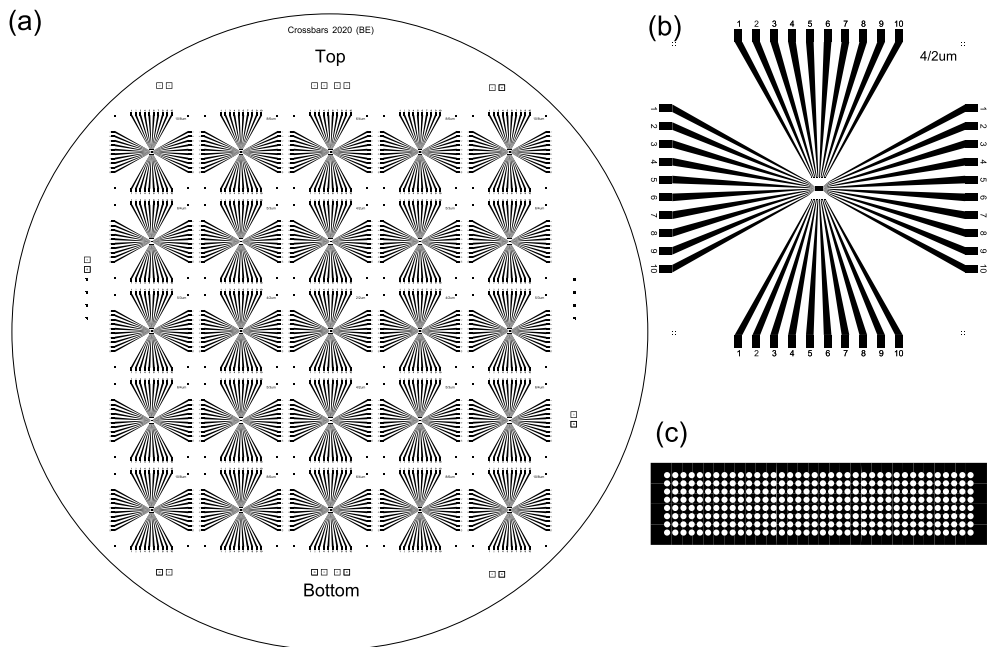


FIGURE A.7: Electron beam mask layout for bottom electrode fabrication. (a) The mask is designed for a 4" wafer, which consists of 25 chips with alignment markers for the passivation mask. Each chip is designed to include 10 leads with different width of 2 μm , 4 μm , 5 μm , 6 μm , 8 μm , and 10 μm . The leads are positioned with 10 μm interdistance. (b) The 4 μm wide chip layout, which consists of 10 leads connected to feedlines and contact pads for top electrode assembling. (c) Zoom image of 4 μm lead

Photomask design for passivation layer

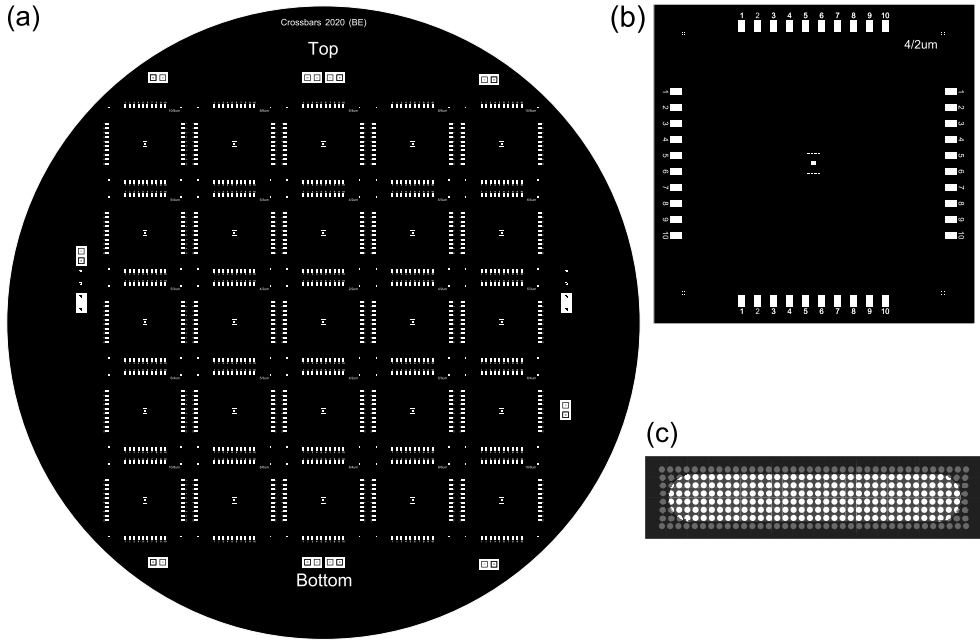


FIGURE A.8: Photomask layout for passivation layer. (a) 4" wafer designed as dark field mask with bright field alignment markers. (b) The $4\mu\text{m}$ wide chip layout, which consists of openings for feedlines, contact pads for top electrode assembling, and openings for central parts of the leads. (c) Zoom image of $4\mu\text{m}$ lead.

A.3 OPTICAL PROPERTIES OF NANO HOLE ARRAYS

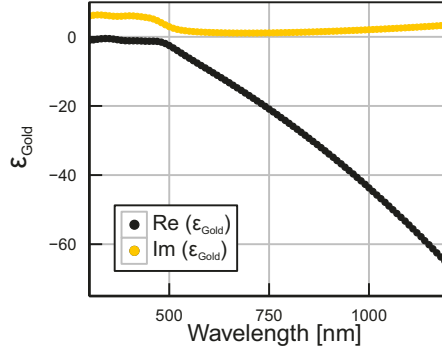


FIGURE A.10: Dielectric permittivity of gold $\epsilon_{Gold} = Re(\epsilon_{Gold}) + i \cdot Im(\epsilon_{Gold})$ (black - real part, yellow - imaginary part)

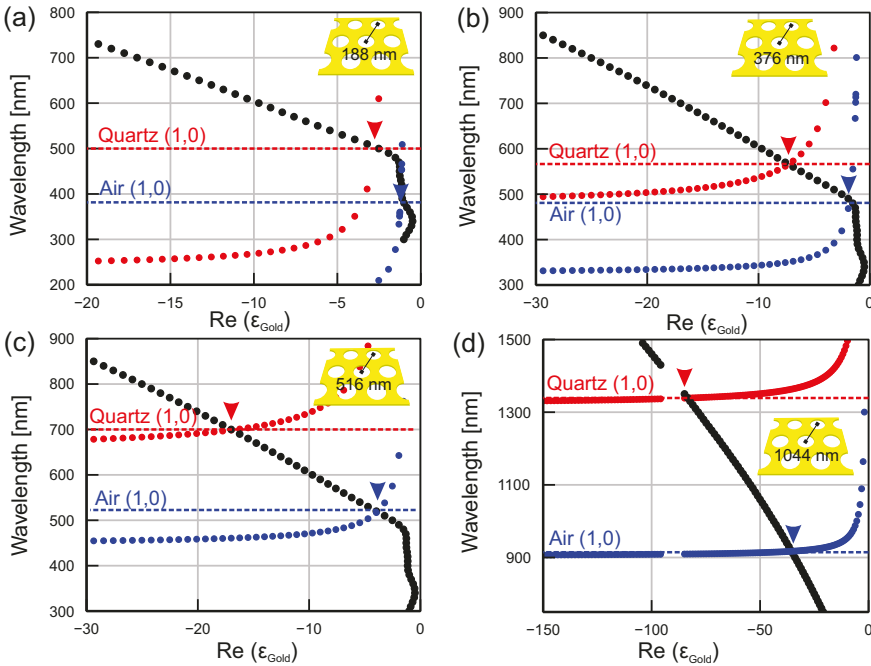


FIGURE A.11: Wavelength vs $Re(\epsilon_{Gold})$ curves calculated based on equation 2.19 for nanohole arrays with lattice constants of (a) 188, (b) 376, (c) 516 and (d) 1044 nm. Red datapoints - surface plasmon resonance that corresponds to the interface between quartz and gold for (1,0) mode; Blue datapoints - resonance between gold and air interface for (1,0) mode. Intersections with $Re(\epsilon_{Gold})$ (arrowhead marks) determine the position of SPP resonance correspondingly.

A.4 FDTD AND EXPERIMENTAL SPECTRUM

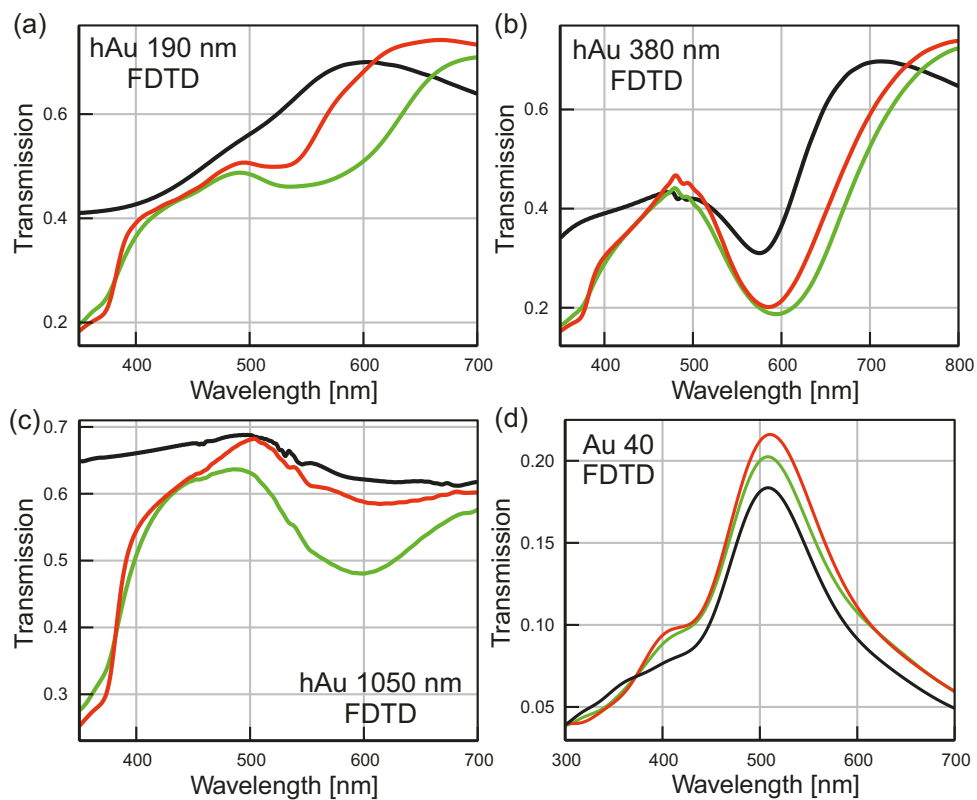


FIGURE A.12: FDTD simulated transmission spectra of C5FHSAc film on a) – hAu with lattice of 188 nm, b) – 376 nm, c) – 1044 nm, d) – solid Au of 40 nm thickness (black – bare electrode, red – open film on electrode, green – closed film on electrode)

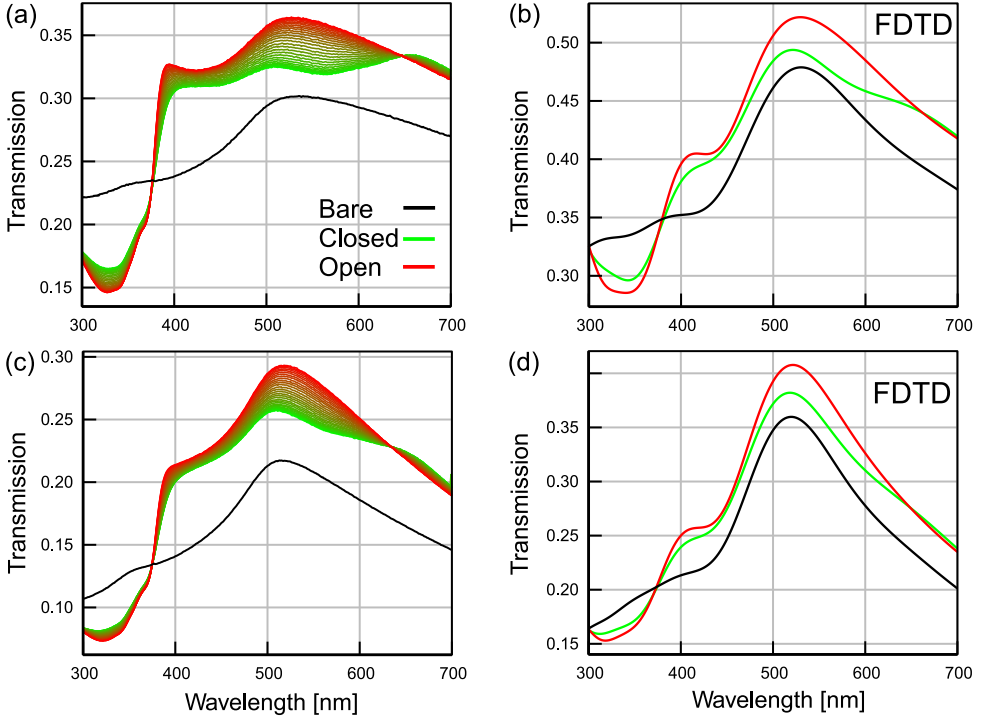


FIGURE A.13: Top row: Transmission spectrum of compact Au of 10 nm thickness (black) with spin-coated molecular film in open (red) and closed (green) form. (a) Experimental data, (b) FDTD simulation. Bottom row: Transmission spectrum of compact Au of 20 nm thickness (black) with spin-coated molecular film in open (red) and closed (green) form. (c) Experimental data, (d) FDTD simulation

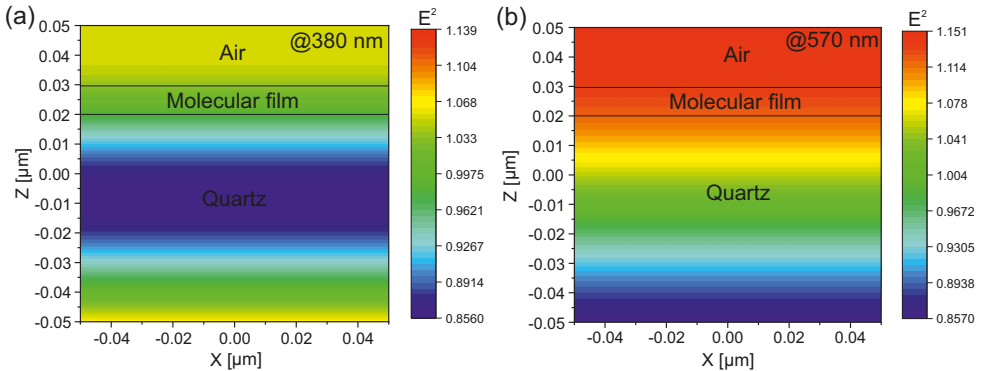


FIGURE A.14: Square of electrical field distribution in the x - z cross-section of C_5FHSAc molecular film on quartz substrate for (a) open configuration at 380 nm and (b) closed configuration at 570 nm.

REFERENCES

- [1] H. Jeong et al. “High-Yield Functional Molecular Electronic Devices”. *ACS Nano* 11.7 (2017), pp. 6511–6548.
- [2] M. Irie et al. “Photochromism of Diarylethene Molecules and Crystals: Memories, Switches, and Actuators”. *Chemical Reviews* 114.24 (2014), pp. 12174–12277.
- [3] Y. Wakayama et al. “Photochromism for optically functionalized organic field-effect transistors: a comprehensive review”. *Journal of Materials Chemistry C* 8.32 (2020), pp. 10956–10974.
- [4] Y. Li et al. “Light-driven photochromism-induced reversible switching in P3HT–spiropyran hybrid transistors”. *J. Mater. Chem.* 22.10 (2012), pp. 4261–4265.
- [5] Y. Kim et al. “Charge Transport Characteristics of Diarylethene Photoswitching Single-Molecule Junctions”. *Nano Letters* 12.7 (2012), pp. 3736–3742.
- [6] S.-Z. Pu et al. “Recent advances in diarylethene-based multi-responsive molecular switches”. *Journal of Materials Chemistry C* 4.15 (2016), pp. 3075–3093.
- [7] M. Herder et al. “Improving the Fatigue Resistance of Diarylethene Switches”. *Journal of the American Chemical Society* 137.7 (2015), pp. 2738–2747.
- [8] F. Meng et al. “Orthogonally modulated molecular transport junctions for resettable electronic logic gates”. *Nature Communications* 5.1 (2014), p. 3023.
- [9] G. Pariani et al. “New Insight into the Fatigue Resistance of Photochromic 1,2-Diarylethenes”. *The Journal of Physical Chemistry C* 121.42 (2017), pp. 23592–23598.
- [10] M. Maafi. “Useful Spectrokinetic Methods for the Investigation of Photochromic and Thermo-Photochromic Spiropyrans”. *Molecules* 13.9 (2008), pp. 2260–2302.
- [11] J. Koo et al. “Unidirectional Real-Time Photoswitching of Diarylethene Molecular Monolayer Junctions with Multilayer Graphene Electrodes”. *ACS Applied Materials & Interfaces* 11.12 (2019), pp. 11645–11653.
- [12] D. Dulić et al. “One-Way Optoelectronic Switching of Photochromic Molecules on Gold”. *Physical Review Letters* 91.20 (2003), p. 207402.
- [13] J. Langer et al. “Present and Future of Surface-Enhanced Raman Scattering”. *ACS Nano* 14.1 (2020), pp. 28–117.
- [14] L. M. Almeahmadi et al. “Surface Enhanced Raman Spectroscopy for Single Molecule Protein Detection”. *Scientific Reports* 9.1 (2019), p. 12356.
- [15] B. Lenyk et al. “Dual-Transducer Malaria Aptasensor Combining Electrochemical Impedance and Surface Plasmon Polariton Detection on Gold Nanohole Arrays”. *ChemElectroChem* 7.22 (2020), pp. 4594–4600.

- [16] A. Minopoli et al. “Ultrasensitive antibody-aptamer plasmonic biosensor for malaria biomarker detection in whole blood”. *Nature Communications* 11.1 (2020), p. 6134.
- [17] L. Feng et al. “Recent Advances of Plasmonic Organic Solar Cells: Photophysical Investigations”. *Polymers* 10.2 (2018), p. 123.
- [18] S. Mubeen et al. “On the Plasmonic Photovoltaic”. *ACS Nano* 8.6 (2014), pp. 6066–6073.
- [19] Y. H. Jang et al. “Plasmonic Solar Cells: From Rational Design to Mechanism Overview”. *Chemical Reviews* 116.24 (2016), pp. 14982–15034.
- [20] A. J. Kronemeijer et al. “Reversible Conductance Switching in Molecular Devices”. *Advanced Materials* 20.8 (2008), pp. 1467–1473.
- [21] D. Kim et al. “Reversible Switching Phenomenon in Diarylethene Molecular Devices with Reduced Graphene Oxide Electrodes on Flexible Substrates”. *Advanced Functional Materials* 25.37 (2015), pp. 5918–5923.
- [22] R. C. Chiechi et al. “Eutectic Gallium–Indium (EGaIn): A Moldable Liquid Metal for Electrical Characterization of Self-Assembled Monolayers”. *Angewandte Chemie International Edition* 47.1 (2008), pp. 142–144.
- [23] A. Vilan and D. Cahen. “Soft Contact Deposition onto Molecularly Modified GaAs. Thin Metal Film Flotation: Principles and Electrical Effects”. *Advanced Functional Materials* 12.1112 (2002), pp. 795–807.
- [24] R. Gordon et al. “Resonant optical transmission through hole-arrays in metal films: physics and applications”. *Laser & Photonics Reviews* 4.2 (2009), pp. 311–335.
- [25] E. Kretschmann and H. Raether. “Notizen: Radiative Decay of Non Radiative Surface Plasmons Excited by Light”. *Zeitschrift für Naturforschung A* 23.12 (1968), pp. 2135–2136.
- [26] P. T. Mathew and F. Fang. “Advances in Molecular Electronics: A Brief Review”. *Engineering* 4.6 (2018), pp. 760–771.
- [27] D. Mayer and E. Scheer. “Stability makes a difference”. *Nature Nanotechnology* 14.10 (2019), pp. 925–926.
- [28] N. Xin et al. “Concepts in the design and engineering of single-molecule electronic devices”. *Nature Reviews Physics* 1.3 (2019), pp. 211–230.
- [29] B. Chen and K. Xu. “Single Molecule-Based Electronic Devices: A Review”. *Nano* 14.11 (2019), p. 1930007.
- [30] L. Sun et al. “Single-molecule electronics: from chemical design to functional devices”. *Chem. Soc. Rev.* 43.21 (2014), pp. 7378–7411.
- [31] D. Vuillaume. “Molecular Electronics: From Single-Molecule to Large-Area Devices”. *ChemPlusChem* 84.9 (2019), pp. 1215–1221.
- [32] A. Vilan, D. Aswal, and D. Cahen. “Large-Area, Ensemble Molecular Electronics: Motivation and Challenges”. *Chemical Reviews* 117.5 (2017), pp. 4248–4286.
- [33] L. Herrer, S. Martín, and P. Cea. “Nanofabrication Techniques in Large-Area Molecular Electronic Devices”. *Applied Sciences* 10.17 (2020), p. 6064.
- [34] I. Baldea. *Molecular Electronics: An Experimental and Theoretical Approach*. Ed. by I. Baldea. Pan Stanford, 2016, p. 462.
- [35] J. C. Cuevas and E. Scheer. *Molecular Electronics*. Vol. 1. World Scientific Series in Nanoscience and Nanotechnology. World Scientific, 2010.

-
- [36] R. L. McCreery, H. Yan, and A. J. Bergren. “A critical perspective on molecular electronic junctions: there is plenty of room in the middle”. *Phys. Chem. Chem. Phys.* 15.4 (2013), pp. 1065–1081.
- [37] P. Gehring, J. M. Thijssen, and H. S. J. van der Zant. “Single-molecule quantum-transport phenomena in break junctions”. *Nature Reviews Physics* 1.6 (2019), pp. 381–396.
- [38] C. E. Smith et al. “Length-Dependent Nanotransport and Charge Hopping Bottlenecks in Long Thiophene-Containing π -Conjugated Molecular Wires”. *Journal of the American Chemical Society* 137.50 (2015), pp. 15732–15741.
- [39] H. Yan et al. “Activationless charge transport across 4.5 to 22 nm in molecular electronic junctions”. *Proceedings of the National Academy of Sciences* 110.14 (2013), pp. 5326–5330.
- [40] W. Wang, T. Lee, and M. A. Reed. “Mechanism of electron conduction in self-assembled alkanethiol monolayer devices”. *Physical Review B* 68.3 (2003), p. 035416.
- [41] X. Guo. *Molecular-Scale Electronics*. Ed. by X. Guo. Topics in Current Chemistry Collections. Cham: Springer International Publishing, 2019, p. 262.
- [42] R. Landauer. “Spatial Variation of Currents and Fields Due to Localized Scatterers in Metallic Conduction”. *IBM Journal of Research and Development* 1.3 (1957), pp. 223–231.
- [43] S. Eränen and J. Sinkkonen. “Generalization of the Landauer conductance formula”. *Physical Review B* 35.5 (1987), pp. 2222–2227.
- [44] Y. A. Berlin et al. “Charge Hopping in Molecular Wires as a Sequence of Electron-Transfer Reactions”. *The Journal of Physical Chemistry A* 107.19 (2003), pp. 3970–3980.
- [45] A. V. Walker. “Toward a new world of molecular devices: Making metallic contacts to molecules”. *Journal of Vacuum Science & Technology A: Vacuum, Surfaces, and Films* 31.5 (2013), p. 050816.
- [46] H. Moehwald and G. Brezesinski. “From Langmuir Monolayers to Multilayer Films”. *Langmuir* 32.41 (2016), pp. 10445–10458.
- [47] D. Bélanger and J. Pinson. “Electrografting: a powerful method for surface modification”. *Chemical Society Reviews* 40.7 (2011), p. 3995.
- [48] G. M. Whitesides. “Self-Assembly at All Scales”. *Science* 295.5564 (2002), pp. 2418–2421.
- [49] H. B. Akkerman et al. “Towards molecular electronics with large-area molecular junctions”. *Nature* 441.7089 (2006), pp. 69–72.
- [50] H. Haick, J. Ghabboun, and D. Cahen. “Pd versus Au as evaporated metal contacts to molecules”. *Applied Physics Letters* 86.4 (2005), p. 042113.
- [51] A. V. Walker. “Building Robust and Reliable Molecular Constructs: Patterning, Metallic Contacts, and Layer-by-Layer Assembly”. *Langmuir* 26.17 (2010), pp. 13778–13785.
- [52] J. Chen. “Large On-Off Ratios and Negative Differential Resistance in a Molecular Electronic Device”. *Science* 286.5444 (1999), pp. 1550–1552.
- [53] K. T. Shimizu et al. “Soft Deposition of Large-Area Metal Contacts for Molecular Electronics”. *Advanced Materials* 18.12 (2006), pp. 1499–1504.
- [54] A. J. Kronemeijer et al. “Universal Scaling of the Charge Transport in Large-Area Molecular Junctions”. *Small* 7.11 (2011), pp. 1593–1598.
-

- [55] S. Seo et al. “Photo-switchable molecular monolayer anchored between highly transparent and flexible graphene electrodes”. *Nature Communications* 4.1 (2013), p. 1920.
- [56] G. Wang et al. “A New Approach for Molecular Electronic Junctions with a Multilayer Graphene Electrode”. *Advanced Materials* 23.6 (2011), pp. 755–760.
- [57] T. Li et al. “Solution-Processed Ultrathin Chemically Derived Graphene Films as Soft Top Contacts for Solid-State Molecular Electronic Junctions”. *Advanced Materials* 24.10 (2012), pp. 1333–1339.
- [58] R. Klajn. “Spiropyran-based dynamic materials”. *Chem. Soc. Rev.* 43.1 (2014), pp. 148–184.
- [59] H. M. D. Bandara and S. C. Burdette. “Photoisomerization in different classes of azobenzene”. *Chem. Soc. Rev.* 41.5 (2012), pp. 1809–1825.
- [60] M. Seibold et al. “Photochromic fulgides: towards their application in molecular electronics”. *Journal of Luminescence* 72-74 (1997), pp. 454–456.
- [61] Y. Yokoyama and Y. Kurita. “Photochromism of Fulgides and Related Compounds”. *Molecular Crystals and Liquid Crystals Science and Technology. Section A. Molecular Crystals and Liquid Crystals* 246.1 (1994), pp. 87–94.
- [62] M. IRIE. “Photochromism of diarylethene molecules and crystals”. *Proceedings of the Japan Academy, Series B* 86.5 (2010), pp. 472–483.
- [63] L. Wang and Q. Li. “Photochromism into nanosystems: towards lighting up the future nanoworld”. *Chemical Society Reviews* 47.3 (2018), pp. 1044–1097.
- [64] S. Helmy et al. “Photoswitching Using Visible Light: A New Class of Organic Photochromic Molecules”. *Journal of the American Chemical Society* 136.23 (2014), pp. 8169–8172.
- [65] B. L. Feringa and W. R. Browne, eds. *Molecular Switches*. Weinheim, Germany: Wiley-VCH Verlag GmbH & Co. KGaA, 2011.
- [66] N. Katsonis et al. “Reversible Conductance Switching of Single Diarylethenes on a Gold Surface”. *Advanced Materials* 18.11 (2006), pp. 1397–1400.
- [67] T. Kudernac et al. “Nano-electronic switches: Light-induced switching of the conductance of molecular systems”. *Journal of Materials Chemistry* 19.39 (2009), p. 7168.
- [68] A. C. Whalley et al. “Reversible Switching in Molecular Electronic Devices”. *Journal of the American Chemical Society* 129.42 (2007), pp. 12590–12591.
- [69] T. Sendler et al. “Light-Induced Switching of Tunable Single-Molecule Junctions”. *Advanced Science* 2.5 (2015), p. 1500017.
- [70] C. Jia et al. “Conductance Switching and Mechanisms in Single-Molecule Junctions”. *Angewandte Chemie International Edition* 52.33 (2013), pp. 8666–8670.
- [71] C. Jia et al. “Covalently bonded single-molecule junctions with stable and reversible photoswitched conductivity”. *Science* 352.6292 (2016), pp. 1443–1445.
- [72] I. Hnid et al. “Highly Efficient Photoswitch in Diarylethene-Based Molecular Junctions”. *Journal of the American Chemical Society* 142.17 (2020), pp. 7732–7736.
- [73] D. Kim et al. “Flexible Molecular-Scale Electronic Devices Composed of Diarylethene Photoswitching Molecules”. *Advanced Materials* 26.23 (2014), pp. 3968–3973.

-
- [74] M. E. Gemayel et al. “Optically switchable transistors by simple incorporation of photochromic systems into small-molecule semiconducting matrices”. *Nature Communications* 6.1 (2015), p. 6330.
- [75] L. Hou et al. “Engineering Optically Switchable Transistors with Improved Performance by Controlling Interactions of Diarylethenes in Polymer Matrices”. *Journal of the American Chemical Society* 142.25 (2020), pp. 11050–11059.
- [76] J. M. Pitarke et al. “Theory of surface plasmons and surface-plasmon polaritons”. *Reports on Progress in Physics* 70.1 (2007), pp. 1–87.
- [77] S. Kawata. *Near-Field Optics and Surface Plasmon Polaritons*. Ed. by S. Kawata. Vol. 81. Topics in Applied Physics. Berlin, Heidelberg: Springer Berlin Heidelberg, 2001, p. 214.
- [78] L. D. Landau and E. M. Lifshitz. *The Classical Theory of Fields*. 4th Editio. Elsevier Ltd, 1987, p. 402.
- [79] S. A. Maier. *Plasmonics: Fundamentals and Applications*. New York, NY: Springer US, 2007.
- [80] W. L. Barnes, A. Dereux, and T. W. Ebbesen. “Surface plasmon subwavelength optics”. *Nature* 424.6950 (2003), pp. 824–830.
- [81] V. Amendola et al. “Surface plasmon resonance in gold nanoparticles: a review”. *Journal of Physics: Condensed Matter* 29.20 (2017), p. 203002.
- [82] I. I. Smolyaninov, Y.-J. Hung, and C. C. Davis. “Surface plasmon dielectric waveguides”. *Applied Physics Letters* 87.24 (2005), p. 241106.
- [83] S. Sital. “Surface Plasmon Modes of Dielectric-Metal-Dielectric Waveguides and Applications”. *IOSR Journal of Electronics and Communication Engineering* 12.2 (2017), pp. 08–19.
- [84] A. Abbas, M. J. Linman, and Q. Cheng. “New trends in instrumental design for surface plasmon resonance-based biosensors”. *Biosensors and Bioelectronics* 26.5 (2011), pp. 1815–1824.
- [85] T. W. Ebbesen et al. “Extraordinary optical transmission through sub-wavelength hole arrays”. *Nature* 391.6668 (1998), pp. 667–669.
- [86] H. A. Bethe. “Theory of Diffraction by Small Holes”. *Physical Review* 66.7-8 (1944), pp. 163–182.
- [87] H. Liu and P. Lalanne. “Microscopic theory of the extraordinary optical transmission”. *Nature* 452.7188 (2008), pp. 728–731.
- [88] T. P. L. Ung et al. “Scanning the plasmonic properties of a nanohole array with a single nanocrystal near-field probe”. *Nanophotonics* 9.4 (2020), pp. 793–801.
- [89] S.-H. Chang, S. K. Gray, and G. C. Schatz. “Surface plasmon generation and light transmission by isolated nanoholes and arrays of nanoholes in thin metal films”. *Optics Express* 13.8 (2005), p. 3150.
- [90] W. L. Barnes et al. “Surface Plasmon Polaritons and Their Role in the Enhanced Transmission of Light through Periodic Arrays of Subwavelength Holes in a Metal Film”. *Physical Review Letters* 92.10 (2004), p. 107401.
- [91] E. Kamenetskii, A. Sadreev, and A. Miroshnichenko. *Fano Resonances in Optics and Microwaves*. Ed. by E. Kamenetskii, A. Sadreev, and A. Miroshnichenko. Vol. 219. Springer Series in Optical Sciences. Cham: Springer International Publishing, 2018, p. 582.

- [92] P. Lalanne, J. C. Rodier, and J. P. Hugonin. “Surface plasmons of metallic surfaces perforated by nanohole arrays”. *Journal of Optics A: Pure and Applied Optics* 7.8 (2005), pp. 422–426.
- [93] T. Sannomiya et al. “Investigation of Plasmon Resonances in Metal Films with Nanohole Arrays for Biosensing Applications”. *Small* 7.12 (2011), pp. 1653–1663.
- [94] E.-H. Lin et al. “Enhancing angular sensitivity of plasmonic nanostructures using mode transition in hexagonal gold nanohole arrays”. *Sensors and Actuators B: Chemical* 241 (2017), pp. 800–805.
- [95] M. Couture et al. “Tuning the 3D plasmon field of nanohole arrays”. *Nanoscale* 5.24 (2013), p. 12399.
- [96] N. Subramaniam et al. “Nonlinear plasmonic behavior of nanohole arrays in thin gold films for imaging lipids”. *Applied Physics Letters* 112.23 (2018), p. 233109.
- [97] D. Y. Lei et al. “Geometry Dependence of Surface Plasmon Polariton Lifetimes in Nanohole Arrays”. *ACS Nano* 4.1 (2010), pp. 432–438.
- [98] S. Crespi, N. A. Simeth, and B. König. “Heteroaryl azo dyes as molecular photoswitches”. *Nature Reviews Chemistry* 3.3 (2019), pp. 133–146.
- [99] H. Li and D.-H. Qu. “Recent advances in new-type molecular switches”. *Science China Chemistry* 58.6 (2015), pp. 916–921.
- [100] L. A. Frolova et al. “Design of rewritable and read-only non-volatile optical memory elements using photochromic spiropyran-based salts as light-sensitive materials”. *Journal of Materials Chemistry C* 3.44 (2015), pp. 11675–11680.
- [101] J. Lee et al. “Molecular Monolayer Nonvolatile Memory with Tunable Molecules”. *Angewandte Chemie International Edition* 48.45 (2009), pp. 8501–8504.
- [102] S. Kumar et al. “Chemical Locking in Molecular Tunneling Junctions Enables Nonvolatile Memory with Large On–Off Ratios”. *Advanced Materials* 31.15 (2019), pp. 1–6.
- [103] J. F. Li, C. Y. Li, and R. F. Aroca. “Plasmon-enhanced fluorescence spectroscopy”. *Chemical Society Reviews* 46.13 (2017), pp. 3962–3979.
- [104] M. Galperin and A. Nitzan. “Molecular optoelectronics: the interaction of molecular conduction junctions with light”. *Physical Chemistry Chemical Physics* 14.26 (2012), p. 9421.
- [105] P. Törmä and W. L. Barnes. “Strong coupling between surface plasmon polaritons and emitters: a review”. *Reports on Progress in Physics* 78.1 (2015), p. 013901.
- [106] B. Lenyk et al. “Surface Plasmon-Enhanced Switching Kinetics of Molecular Photochromic Films on Gold Nanohole Arrays”. *Nano Letters* 20.7 (2020), pp. 5243–5250.
- [107] M. Min et al. “Voltage-Controlled Nonvolatile Molecular Memory of an Azobenzene Monolayer through Solution-Processed Reduced Graphene Oxide Contacts”. *Advanced Materials* 25.48 (2013), pp. 7045–7050.
- [108] D. Akinwande, N. Petrone, and J. Hone. “Two-dimensional flexible nanoelectronics”. *Nature Communications* 5.1 (2014), p. 5678.
- [109] Z. He et al. “Principle and Applications of the Coupling of Surface Plasmons and Excitons”. *Applied Sciences* 10.5 (2020), p. 1774.
- [110] F. Valmorra et al. “Strong coupling between surface plasmon polariton and laser dye rhodamine 800”. *Applied Physics Letters* 99.5 (2011), p. 051110.

-
- [111] N. I. Cade, T. Ritman-Meer, and D. Richards. “Strong coupling of localized plasmons and molecular excitons in nanostructured silver films”. *Physical Review B* 79.24 (2009), p. 241404.
- [112] A. J. Moilanen, T. K. Hakala, and P. Törmä. “Active Control of Surface Plasmon–Emitter Strong Coupling”. *ACS Photonics* 5.1 (2018), pp. 54–64.
- [113] A. Spangenberg et al. “Photoswitchable interactions between photochromic organic diarylethene and surface plasmon resonance of gold nanoparticles in hybrid thin films”. *Physical Chemistry Chemical Physics* 15.24 (2013), p. 9670.
- [114] A.-L. Baudrion et al. “Reversible Strong Coupling in Silver Nanoparticle Arrays Using Photochromic Molecules”. *Nano Letters* 13.1 (2013), pp. 282–286.
- [115] E. S. H. Kang et al. “Strong Plasmon–Exciton Coupling with Directional Absorption Features in Optically Thin Hybrid Nanohole Metasurfaces”. *ACS Photonics* 5.10 (2018), pp. 4046–4055.
- [116] W. M. Wilson, J. W. Stewart, and M. H. Mikkelsen. “Surpassing Single Line Width Active Tuning with Photochromic Molecules Coupled to Plasmonic Nanoantennas”. *Nano Letters* 18.2 (2018), pp. 853–858.
- [117] M. Großmann et al. “Light-Triggered Control of Plasmonic Refraction and Group Delay by Photochromic Molecular Switches”. *ACS Photonics* 2.9 (2015), pp. 1327–1332.
- [118] A. Pimpin and W. Srituravanich. “Review on Micro- and Nanolithography Techniques and their Applications”. *Engineering Journal* 16.1 (2012), pp. 37–56.
- [119] Y. Chen. “Nanofabrication by electron beam lithography and its applications: A review”. *Microelectronic Engineering* 135 (2015), pp. 57–72.
- [120] C. L. Haynes and R. P. Van Duyne. “Nanosphere Lithography: A Versatile Nanofabrication Tool for Studies of Size-Dependent Nanoparticle Optics”. *The Journal of Physical Chemistry B* 105.24 (2001), pp. 5599–5611.
- [121] P. Colson, C. Henrist, and R. Cloots. “Nanosphere Lithography: A Powerful Method for the Controlled Manufacturing of Nanomaterials”. *Journal of Nanomaterials* 2013 (2013), pp. 1–19.
- [122] C. Zhang, S. Cvetanovic, and J. M. Pearce. “Fabricating ordered 2-D nanostructured arrays using nanosphere lithography”. *MethodsX* 4 (2017), pp. 229–242.
- [123] Y. Wang et al. “Advanced colloidal lithography: From patterning to applications”. *Nano Today* 22 (2018), pp. 36–61.
- [124] B. Ai et al. “Advanced Colloidal Lithography Beyond Surface Patterning”. *Advanced Materials Interfaces* 4.1 (2017), p. 1600271.
- [125] Y. Xia et al. “Template-Assisted Self-Assembly of Spherical Colloids into Complex and Controllable Structures”. *Advanced Functional Materials* 13.12 (2003), pp. 907–918.
- [126] X. Xu et al. “Multiple-Patterning Nanosphere Lithography for Fabricating Periodic Three-Dimensional Hierarchical Nanostructures”. *ACS Nano* 11.10 (2017), pp. 10384–10391.
- [127] B. Ai and Y. Zhao. “Glancing angle deposition meets colloidal lithography: a new evolution in the design of nanostructures”. *Nanophotonics* 8.1 (2018), pp. 1–26.
- [128] M. J. Madou. *Fundamentals of Microfabrication*. CRC Press, 2002.
- [129] R. Luttge. *Microfabrication for Industrial Applications*. Ed. by R. Luttge. William Andrew Publishing, 2011, p. 312.
-

References

- [130] R. W. Johnson, A. Hultqvist, and S. F. Bent. “A brief review of atomic layer deposition: from fundamentals to applications”. *Materials Today* 17.5 (2014), pp. 236–246.
- [131] F. J. Giessibl. “Advances in atomic force microscopy”. *Reviews of Modern Physics* 75.3 (2003), pp. 949–983.
- [132] Y. F. Dufrière et al. “Imaging modes of atomic force microscopy for application in molecular and cell biology”. *Nature Nanotechnology* 12.4 (2017), pp. 295–307.
- [133] L. Van der Pauw. “A method of measuring specific resistivity and Hall effect of discs of arbitrary shape”. *Philips Research Reports* 13 (1958), pp. 1–9.
- [134] K. S. Kunz and R. J. Luebbers. *The Finite Difference Time Domain Method for Electromagnetics*. Boca Raton: CRC Press, 1993, p. 464.
- [135] S. D. Gedney. “Introduction to the Finite-Difference Time-Domain (FDTD) Method for Electromagnetics”. *Synthesis Lectures on Computational Electromagnetics* 6.1 (2011), pp. 1–250.
- [136] Kane Yee. “Numerical solution of initial boundary value problems involving maxwell’s equations in isotropic media”. *IEEE Transactions on Antennas and Propagation* 14.3 (1966), pp. 302–307.
- [137] A. E. Tekkaya and C. Soyarslan. “Finite Element Method”. In: *CIRP Encyclopedia of Production Engineering*. Berlin, Heidelberg: Springer Berlin Heidelberg, 2014, pp. 508–514.
- [138] A.-P. Blanchard-Dionne and M. Meunier. “Multiperiodic nanohole array for high precision sensing”. *Nanophotonics* 8.2 (2019), pp. 325–329.
- [139] C. Hahn, A. Hajebifard, and P. Berini. “Helium focused ion beam direct milling of plasmonic heptamer-arranged nanohole arrays”. *Nanophotonics* 9.2 (2020), pp. 393–399.
- [140] M. C. Traub, W. Longsine, and V. N. Truskett. “Advances in Nanoimprint Lithography”. *Annual Review of Chemical and Biomolecular Engineering* 7.1 (2016), pp. 583–604.
- [141] B. Ai et al. “Plasmonic films based on colloidal lithography”. *Advances in Colloid and Interface Science* 206 (2014), pp. 5–16.
- [142] A. Chandramohan et al. “Model for large-area monolayer coverage of polystyrene nanospheres by spin coating”. *Scientific Reports* 7.1 (2017), p. 40888.
- [143] J. Yu et al. “Preparation of High-Quality Colloidal Mask for Nanosphere Lithography by a Combination of Air/Water Interface Self-Assembly and Solvent Vapor Annealing”. *Langmuir* 28.34 (2012), pp. 12681–12689.
- [144] M. Szekeres et al. “Ordering and optical properties of monolayers and multilayers of silica spheres deposited by the Langmuir–Blodgett method”. *J. Mater. Chem.* 12.11 (2002), pp. 3268–3274.
- [145] V. Schöps et al. “Facile, non-destructive characterization of 2d photonic crystals using UV-vis-spectroscopy”. *Physical Chemistry Chemical Physics* 20.6 (2018), pp. 4340–4346.
- [146] V. Lotito and T. Zambelli. “Self-assembly and nanosphere lithography for large-area plasmonic patterns on graphene”. *Journal of Colloid and Interface Science* 447 (2015), pp. 202–210.
- [147] M. López-García et al. “Light confinement by two-dimensional arrays of dielectric spheres”. *Physical Review B* 85.23 (2012), p. 235145.

-
- [148] V. Schöps. “Development of Molecular Area Contacts for Optoelectronic Applications”. Doctoral dissertation. University of Konstanz, 2017, p. 188.
- [149] T. J. J. Hondrich et al. “MEA Recordings and Cell-Substrate Investigations with Plasmonic and Transparent, Tunable Holey Gold”. *ACS Applied Materials & Interfaces* 11.50 (2019), pp. 46451–46461.
- [150] Z. Li. *Development of Stretchable and Transparent Holey Electrodes on Polymer Substrates (MSc thesis)*. 2020, p. 83.
- [151] S. Tang. *A Molecular Crossbar Junction and its Optoelectronic Application (MSc thesis)*. 2019, p. 98.
- [152] J. Wolf et al. “Synthesis and Photoswitching Studies of OPE-Embedded Difurylperfluorocyclopentenes”. *The Journal of Organic Chemistry* 78.17 (2013), pp. 8366–8375.
- [153] E. Orgiu et al. “Optically switchable transistor via energy-level phototuning in a bicomponent organic semiconductor”. *Nature Chemistry* 4.8 (2012), pp. 675–679.
- [154] M. Losurdo et al. “Spectroscopic ellipsometry and polarimetry for materials and systems analysis at the nanometer scale: state-of-the-art, potential, and perspectives”. *Journal of Nanoparticle Research* 11.7 (2009), pp. 1521–1554.
- [155] T. Kamiya et al. “Kramers-Kronig Relations and Sum Rules in Nonlinear Optics”. In: *Kramers-Kronig Relations in Optical Materials Research*. Berlin/Heidelberg: Springer-Verlag, 2005, pp. 71–81.
- [156] Z. Szabo. “Closed Form Kramers–Kronig Relations to Extract the Refractive Index of Metamaterials”. *IEEE Transactions on Microwave Theory and Techniques* 65.4 (2017), pp. 1150–1159.
- [157] R. A. Rupp et al. “Absorbance kinetics of dye-doped systems with photochemical first order kinetics”. *physica status solidi (b)* 244.6 (2007), pp. 2138–2150.
- [158] W. J. Tomlinson. “Dynamics of photochromic conversion in optically thick samples: theory”. *Applied Optics* 15.3 (1976), p. 821.
- [159] R. L. Olmon et al. “Optical dielectric function of gold”. *Physical Review B - Condensed Matter and Materials Physics* 86.23 (2012), pp. 1–9.
- [160] H. Gao, J. Henzie, and T. W. Odom. “Direct Evidence for Surface Plasmon-Mediated Enhanced Light Transmission through Metallic Nanohole Arrays”. *Nano Letters* 6.9 (2006), pp. 2104–2108.
- [161] A. Mooradian. “Photoluminescence of Metals”. *Physical Review Letters* 22.5 (1969), pp. 185–187.
- [162] J. Braun et al. “How Holes Can Obscure the View: Suppressed Transmission through an Ultrathin Metal Film by a Subwavelength Hole Array”. *Physical Review Letters* 103.20 (2009), p. 203901.
- [163] E. Kamenetskii, A. Sadreev, and A. Miroshnichenko, eds. *Fano Resonances in Optics and Microwaves*. Vol. 219. Springer Series in Optical Sciences. Cham: Springer International Publishing, 2018.

Band / Volume 64

Quantitative investigation of group III-nitride interfaces by a combination of scanning tunneling microscopy and off-axis electron holography

Y. Wang (2021), 102 pp

ISBN: 978-3-95806-534-5

Band / Volume 65

Scalable Control Electronics for a Spin Based Quantum Computer

L. Geck (2021), xiv, 114, xv-xxxiii

ISBN: 978-3-95806-540-6

Band / Volume 66

DNA-capped silver nanoparticles for stochastic nanoparticle impact electrochemistry

L. Nörbel (2021), VI, 142 pp

ISBN: 978-3-95806-541-3

Band / Volume 67

Development, characterization, and application of intraretinal implants

V. Rincón Montes (2021), XII, 173 pp

ISBN: 978-3-95806-553-6

Band / Volume 68

Optogenetic and electrical investigation of network dynamics in patterned neuronal cultures

T. J. J. Hondrich (2021), x, 177 pp

ISBN: 978-3-95806-555-0

Band / Volume 69

Disentangling parallel conduction channels by charge transport measurements on surfaces with a multi-tip scanning tunneling microscope

S. Just (2021), xii, 225 pp

ISBN: 978-3-95806-574-1

Band / Volume 70

Nanoscale four-point charge transport measurements in topological insulator thin films

A. Leis (2021), ix, 153 pp

ISBN: 978-3-95806-580-2

Band / Volume 71

Investigating the Interaction between π -Conjugated Organic Molecules and Metal Surfaces with Photoemission Tomography

X. Yang (2021), xviii, 173 pp

ISBN: 978-3-95806-584-0

Band / Volume 72

Three-Dimensional Polymeric Topographies for Neural Interfaces

F. Milos (2021), 133 pp

ISBN: 978-3-95806-586-4

Band / Volume 73

Development, characterization, and application of compliant intracortical implants

K. Srikantharajah (2021), xiv, 155, xv-xvii pp

ISBN: 978-3-95806-587-1

Band / Volume 74

Modelling, implementation and characterization of a Bias-DAC in CMOS as a building block for scalable cryogenic control electronics for future quantum computers

P. N. Vliex (2021), xiv, 107, xv-xxviii pp

ISBN: 978-3-95806-588-8

Band / Volume 75

Development of Electrochemical Aptasensors for the Highly Sensitive, Selective, and Discriminatory Detection of Malaria Biomarkers

G. Figueroa Miranda (2021), XI, 135 pp

ISBN: 978-3-95806-589-5

Band / Volume 76

Nanostraw- Nanocavity MEAs as a new tool for long-term and high sensitive recording of neuronal signals

P. Shokoohimehr (2021), xi, 136 pp

ISBN: 978-3-95806-593-2

Band / Volume 77

Surface plasmon-enhanced molecular switching for optoelectronic applications

B. Lenyk (2021), x, 129 pp

ISBN: 978-3-95806-595-6

Weitere **Schriften des Verlags im Forschungszentrum Jülich** unter
<http://wwwzb1.fz-juelich.de/verlagextern1/index.asp>

Information
Band / Volume 77
ISBN 978-3-95806-595-6